OPTICAL AND ELECTROCHEMICAL STUDIES OF SELENIUM BASED NANOCOMPOSITES

Thesis Submitted to the University of Calicut for the Award of
DOCTOR OF PHILOSOPHY IN PHYSICS
By

ANUPAMA K

Under the Supervision of

DR. ANN MARY K A

Research And Post-Graduate Department of Physics
St. Thomas' College (Autonomous), Thrissur
Kerala-680 001

NOVEMEBR 2024

OPTICAL AND ELECTROCHEMICAL STUDIES OF SELENIUM BASED NANOCOMPOSITES

Thesis Submitted to the University of Calicut for the Award of

DOCTOR OF PHILOSOPHY IN PHYSICS

By

ANUPAMA K

Under the Supervision of

DR. ANN MARY K A

Research And Post-Graduate Department of Physics

St. Thomas' College (Autonomous), Thrissur

Kerala-680 001

November 2024

Dedicated to

my Achan and Amma……

CERTIFICATE

This is to certify that the thesis entitled "**OPTICAL AND ELECTROCHEMICAL STUDIES OF SELENIUM BASED NANOCOMPOSITES**" is an authentic record of precise research work carried out by Ms. Anupama K under my guidance and supervision for the partial fulfillment of the award of degree of Doctor of Philosophy in Physics, submitted to University of Calicut and the same has not been submitted elsewhere for any degree or diploma.

Dr. Ann Mary K A
Assistant Professor & Research Guide
Research & Post-Graduate Department of Physics
St. Thomas' College (Autonomous), Thrissur
Kerala

DECLARATION

I hereby declare that the work presented in the thesis entitled "**OPTICAL AND ELECTROCHEMICAL STUDIES OF SELENIUM BASED NANOCOMPOSITES**" is based on the original work done by me under the guidance of Dr. Ann Mary K A, Assistant Professor, Research & Post-Graduate Department of Physics, St. Thomas' College (Autonomous), Thrissur, and has not been included in any other thesis submitted previously for the award of any degree. The contents of the thesis have undergone plagiarism check using iThenticate software at C.H.M.K. Library, University of Calicut, and the similarity index was found within the permissible limit. I also declare that the thesis is free from AI generated contents.

Thrissur Anupama K

14-11-2024

Dr. Ann Mary K A

Assistant Professor & Research Guide

Research & Post-Graduate Department of Physics

St. Thomas' College (Autonomous), Thrissur

ACKNOWLEDGEMENT

The journey of my research has been nothing less of a challenge and yet a rewarding experience. It has humbled me, strengthened and taught me of my capabilities. At this juncture, I have many people to thank from the bottom of my heart and words will probably fall short.

Firstly, I would like to acknowledge my heartfelt indebtedness and sincere gratitude to my supervisor, Dr. Ann Mary K A, Assistant Professor, Department of Physics, St. Thomas' College (Autonomous), Thrissur, for her unerring guidance and support throughout my research endeavour. She has been extremely patient with me even during the tough phases, always forgiving my lapses and has been a constant source of encouragement. Her passion towards research is truly inspiring.

I would like to sincerely acknowledge my gratitude to Dr. Joe Kizhakooden, Head of Department of Physics for his unwavering support and valuable suggestions. I would also like to pay my special thanks to the former Head of Department, Prof. P M Joy, who has always been very affectionately concerned about my research and thesis submission, helping me to remain optimistic through rough times. I also wish to extend my profound gratitude towards the Principal and management of St. Thomas' College (Autonomous), Thrissur. The past 9 years in the institution has shaped me from a naive M.Sc student to a confident and sophisticated researcher. Besides, my heartfelt thanks to the former and present faculty members of our department, Prof. Varghese P

Kodenkandath, Dr. Anto Johny T, Dr. Nees Paul, Dr. Vimalkumar T V, Dr. Daison Panengaden, Dr. Johns Naduvath, Mr. Joby Thomas, Dr. Jilmy P Joy and Ms. Sikha Simon K, for their unending support and encouragement. The department has been a pillar of strength from my post-graduation days and each faculty has played an instrumental role in moulding me to who I am today. A special word of appreciation and love to all the present and former laboratory and office staff of the college. Their promptness, support, and love have been gratifying.

I acknowledge the financial assistance received from KSCSTE that had fuelled my research. I extend my profound gratitude to CSIF University of Calicut, SAIF-Mahatma Gandhi University Kottayam, SPAP- Mahatma Gandhi University Kottayam, IUIC-MG University, STIC Kochi, CRF-CeNS Banglore, SAMat Research Facilities- JNCASR Banglore, Amala Cancer Research Centre Society Thrissur, Department of Physics, Department of Botany and Department of Chemistry, St. Thomas' College (Autonomous), Thrissur, for helping me in my research analysis. I deeply thank Dr. Xavier T S, Assistant Professor, Department of Physics, Dr. Athira A R and Merin Tomy, research scholars, Government College for Women, Thiruvananthapuram, for their support in electrochemical studies.

I express my heartfelt affection to Tessy Paul, Jibin P O and Manjusha Rose Jose, my groupmates and research companions for their unconditional love, and care. They have supported me from day one of my research and has always been there for me through thick and thin. I am extremely thankful for the friendly

and warm atmosphere provided by my lab mates Anitha T V, Swathy Mohanan, Shanu A S, Greatel Francis Paramel, Gadha Menon K and Jasmi K K that always welcomed me. I will always be grateful for their love, enthusiasm, selfless and unwavering support. I also take this opportunity to sincerely thank my friends, seniors and colleagues at Forensic Science Department, Kerala Police for their constant motivation towards completion of my thesis.

This thesis would have never been a reality without the sacrifices made by my parents. Despite being unavailable for them amidst my studies, they have never complained, but only motivated me to complete my research. Their prayer for me was what sustained me thus far. I owe them my deepest gratitude and thank them for standing by me and believing in me even when I doubted myself. I would also like to extend my love and affection to my dear brother for his constant support and care.

Though many have not been mentioned, none is forgotten.

I place everything before the feet of the Omnipotent.

Anupama K

CONTENTS

3. Trigonal selenium quantum dots for fluorescence sensing applications

LIST OF FIGURES

LIST OF TABLES

Abstract

Development of novel nanomaterials through facile and hassle-free synthesis routes have been an intriguing genre of material research. This thesis primarily focuses on the synthesis and characterizations of selenium (Se) nanocrystallites in two different hosts-silica and polyaniline. Additionally, the ability of Se to form variety of allotropic phases is investigated and their morphological, crystalline, microstructural and spectroscopic properties are studied in detail. Cubic and amorphous forms of Se are synthesized in silica matrix via sol-gel route followed by thermal annealing. On the other hand, trigonal and monoclinic Se nanocrystallites are synthesized in silica matrix via a combination of sol-gel assisted solvothermal route. Se was incorporated into cellulose-polyaniline nanocomposite via a one-pot room temperature mediated polymerization technique. The trigonal Se-SiO_2 nanocomposite is used for the inner filter effect based optical sensing of curcumin. The Se/cellulose/polyaniline ternary nanocomposite was studied for electrochemical energy storage application.

Key words: Selenium, quantum dots, fluorescence sensing, inner filter effect, polyaniline, nanocomposite, electrochemical energy storage, pseudocapacitor.

സംഗ്രഹം

. സുഗമവും, ലളിതവുമായ പ്രക്രിയകളിലൂടെ നൂതനവും വൈവിധ്യവുമാർന്ന നാനോതല ഘടനകൾ രൂപകൽപന ചെയ്തെടുക്കുകയെന്നത് നാനോതല ഗവേഷണ രീതികൾക്ക് അനിവാര്യമായ ഒന്നാണ്. സെലീനിയം നാനോഘടനകളുടെ ഉല്പാദനവും അതിന്റെ സവിഷേശതകളും ആണ് ഈ പ്രബന്ധം പ്രഥമമായി ഊന്നൽ നൽകിയിരിക്കുന്നത്. അതോടൊപ്പം തന്നെ സെലീനിയത്തിന്റെ വ്യത്യസ്ഥമായ രൂപാന്തരങ്ങളെക്കുറിച്ചുള്ള വിശദമായ പഠനങ്ങൾ കൂടെ ഈ പ്രബന്ധത്തിൽ ഉൾപെടുത്തിയിട്ടുണ്ട്. സെലീനിയത്തിന്റെ ക്യൂബിക്കും അമോർഫസും ആയ രൂപങ്ങൾ സോൾ ജെൽ പ്രക്രിയയിലൂടെയും മോണോക്ലിനിക്കും, ട്രൈഗണൽ രൂപാന്തരങ്ങൾ സോൾ ജെലിനൊപ്പം സോൾവോ തെർമൽ ട്രീട്മെന്റിലൂടെയാണു സിലിക്ക മാട്രിക്സിലേയ്ക്ക് സംയോജിപ്പിച്ചിട്ടുള്ളത്. ഇതുകൂടാതെ സെല്ലുലോസ് പോളി എനിലീൻ ഹൈബ്രിഡ് മാട്രിക്സിലേയ്ക്കും സെലിനിയം സംയോജപ്പെടുത്തിയിട്ടുണ്ട്. ട്രൈഗണൽ സെലിനിയും സിലിക്ക കോമ്പോസിറ്റ ഒരു ഒപ്റ്റിക്കൽ സെൻസറായും ട്രൈഗണൽ സെലിനിയം സെല്ലുലോസ് പോളി എനിലീൻ കോമ്പോസിറ്റ ഒരു പ്രബലമായ സൂപ്പർ കപ്പാസിറ്റർ ഇലെക്ട്രോഡ് ആയും ഈ പ്രബന്ധത്തിൽ അവതരിപ്പിച്ചിട്ടുണ്ട്.

Preface

Quantum dots or “artificial atoms” with reduced dimensionality opened vast avenues to most of the mature technologies in our life today. Their size dependent properties especially tunable photoluminescence, high quantum yields, photostability etc have been instrumental in many device applications. However, in-depth knowledge of their morphology, functionalization capabilities and detailed understanding on correlation of their structure to its properties is vital for any device application. Selenium, one of the earliest known photovoltaic and photoconducting material is noteworthy due to its ability to form different allotropes. Our objective is to explore less studied phases of nanostructured selenium. The thesis aims to understand the optical and electrochemical features of selenium in two different host matrices-silica and polyaniline (PANI). The thesis is divided into seven chapters and a brief summary of each chapter is given below.

Chapter 1 - ***General introduction*** deals with nanomaterials, synthetic techniques and their optical and electrochemical properties. A comprehensive introduction to Se nanostructures and conducting polymer -polyaniline based nanocomposites is also presented. The optical properties of nanomaterials and various fluorescence sensing mechanisms are discussed in detail. The electrochemical analysis of various energy storage systems, especially supercapacitors are also presented. The organization of the thesis and the objectives of the research are also given towards the end of the chapter.

Chapter 2- ***Synthesis and characterization of selenium allotropes in silica matrix*** discusses the synthesis and structural characterization of various Se allotropes in silica matrix. The chapter deals with detailed understanding of the synthetic route and structural properties of the four different allotropes of Se-cubic, amorphous, trigonal and monoclinic. The nanocomposites are also studied using preliminary in-vitro cytotoxicity assays by trypan blue exclusion method to assess the biocompatibility of the as synthesized QDs.

Chapter 3- ***Trigonal selenium quantum dots for fluorescence sensing applications*** discuss the characteristic optical absorption and photoluminescence observed for trigonal Se (t-Se) QDs**.** Detailed understanding of the structure of t-Se QDs is done through microscopical studies. The crystal growth mechanism is explained in detail and the various defects observed in the microstructural studies are identified. The material is used as a solid-state fluorescent sensor for the inner filter effect (IFE) based detection of curcumin.

Chapter 4- ***Synthesis of selenium/cellulose/polyaniline composites,*** discusses the synthesis route and structural properties of Se doped polyaniline and cellulose polyaniline polymer hybrid matrix. The composite is fabricated via a facile, room temperature cured one pot polymerization followed by freeze drying route. The effect of drying technique and the addition of Se into the polymer is considered as an astute move for surface-oriented performance of the material.

Chapter 5- S*elenium/ cellulose/ polyaniline nanocomposites for energy storage applications,* discusses the electrochemical characterization of Se/Cellulose/PANI composites for energy storage application. Detailed analysis

of the structure and synergistic behavior of the components is made in the chapter. The function of each component of the ternary nanocomposite is understood in detail with respect to the improved capacitance and cyclic stability of the electrode.

Chapter 6 – *Conclusion* gives a comprehensive summary of the key highlights of the work and **Chapter 7 - *Recommendations*** discusses the recommendations and the future outlook of the present thesis particularly in the field of fluorescent sensors and energy storage devices.

Research Papers Published

1. **Anupama, K**.; Paul, T.; Ann Mary, K. A. Solid-State Fluorescent Selenium Quantum Dots by a Solvothermal-Assisted Sol–Gel Route for Curcumin Sensing. *ACS Omega* **2021**, *6* (33), 21525–21533. https://doi.org/10.1021/acsomega.1c02441.
2. Aravind, A. M.; Tomy, M.; **Kuttapan, A**.; Kakkassery Aippunny, A. M.; Suryabai, X. T. Progress of 2D MXene as an Electrode Architecture for Advanced Supercapacitors: A Comprehensive Review. *ACS Omega* **2023**, *8* (47), 44375–44394. https://doi.org/10.1021/acsomega.3c02002.
3. Ann Mary K A, Tessy Paul, **Anupama Kuttappan**, Jibin P O, Anoop K K, Dual emitting carbon nanoparticles for tunable white light emission, Carbon Trends, 2023, 13, 100296, ISSN 2667-0569. https://doi.org/10.1016/j.cartre.2023.100296.
4. Athira, A. R.; Merin, T.; **Anupama, K**.; Ann Mary, K. A.; Xavier, T. S. Surfactant Incorporated Polyaniline/Co3O4/rGO Ternary Hybrid Composite Symmetric Supercapacitors for Efficient Energy Storage Applications. *Diam. Relat. Mater.* **2022**, *130*, 109475. https://doi.org/10.1016/j.diamond.2022.109475.
5. Paul, T.; **Anupama, K**.; Jibin, P. O.; Ann Mary, K. A. Spectroscopic Investigations on Se/RE Doped Sol Gel Derived Silica Matrices. *Mater. Today Proc.* **2020**, *33*, 1323–1326. https://doi.org/10.1016/j.matpr.2020.04.180.

Research Papers Communicated

6. **K Anupama,** Merin Tomy, T S Xavier, KA Ann Mary, Trigonal Selenium Nanocrystallites Decorated Cellulose-Polyaniline Composite as a Potential Supercapacitor Electrode Material.
7. **K Anupama,** Merin Tomy, T S Xavier, KA Ann Mary, Electrochemical studies of Selenium-Polyaniline nanocomposites synthesized by room temperature cured in-situ polymerization.

Presentation in National/International Conferences

1. *A Fluorescent Sensor for the Detection of Additive Food Colorants Based on Trigonal Selenium Quantum Dots* in International Conference on Recent Advances in Functional Materials (RAFM-2022) at Ram Santan Dharma College, University of Delhi during March 14-16, 2022. (*Best Oral Presentation*)
2. *Trigonal Selenium Quantum Dots for Solid-State Fluorescence Sensing Applications* in Bengaluru India NANO 2024 held during Aug 1-3, 2024 conducted by Govt of Karnataka and DST.

Chapter-1

General Introduction

Nanomaterials have always attracted scientific minds as new and efficient candidates for various applications in day-to–day life. Studies focused on various facile, robust and cost-effective fabrication techniques to explore new candidates with improved application potential. Here, optical and electrochemical potential of nanostructured selenium-based composites are investigated in detail. The brief introduction on nanomaterials and their classification are listed here. A detailed description on their synthesis techniques is also given. The optical properties of nanomaterials, including a brief understanding on application of fluorescence is presented. Additionally, the chapter discuss about selenium nanostructures, conducting polymer and their nanocomposites. Furthermore, the chapter discusses in detail the electrochemical studies of nanomaterials and their application in energy storage devices. The organisation of the thesis including the objectives of the research is given in detail towards the end of the chapter.

1.1. INTRODUCTION

Richard Feynman in 1959, at the American Physical Society's annual meeting, presented a revolutionary lecture titled '*There is plenty of room at the bottom*'. This is termed as the first academic talk on nanotechnology which opened avenues and vast horizon of research in this field. "Nano" "technology" soon began to be understood as the science and engineering of particles with dimensions of tolerances <100 nm at least in one of the three dimensions. These materials were experimentally found to possess improved physical, chemical, biological, optical and electrical properties compared to its bulk counterparts. As a result, these nano structures have now replaced most of the existing bulk materials in all realms of science and technology. Agriculture, medicine, electronics, energy, pollution abatement, cosmetics, telecommunication, mechanical engineering, information technology etc have immensely benefitted with the advent of this field. Research efforts are nowadays driven towards scientific/technological advancement in the field, their synthesis and feasible applications of these nanostructures.

1.1.1. Classification of nanomaterials

Nanomaterials can be classified based on their origin, dimensionality and even pore size. Classification of these materials on the basis of their dimensionality is discussed below.

(a) *Zero-dimensional nanomaterials (0D):* Materials wherein all the three dimensions of the particles are confined in the nano (10^{-9}) range are called zero

dimensional materials. Uniform materials with nano-dimensions like nanoclusters, grains, spheres, fullerenes and Quantum Dots (QDs) fall into this category.

Semiconductor nanocrystals with size ranging about 1-10 nm are termed as *Quantum Dots* (QDs). As a result, the exciton (electron-hole pair) is confined to a domain within the Bohr radius of the material. Or in other words, the electron is restricted from moving above and beyond the de-Broglie wavelength. QDs typically consist of a semiconductor shell and a semiconducting core. The quantum confinement experienced by the dots has several effects on the final material properties which differ from those of larger particles. Squashing of the exciton into this confined space increases its energy and hence quantum dots are always associated with size dependent energy gaps- smaller the dots, greater is the energy of exciton produced. Also, the band gap in QDs changes from continuous as in bulk, to discrete levels similar to that in molecular energy states. These class of materials has a decidedly bright future in various fields like medical bio-imaging[1], solar cells[2], LEDs[3], lasers[4], quantum information technology[5], sensors[6] etc. Moungi G. Bawendi, Louis E. Brus and Alexei I. Ekimov received the 2023 Nobel Prize in Chemistry for the development of these highly functional class of materials[7].

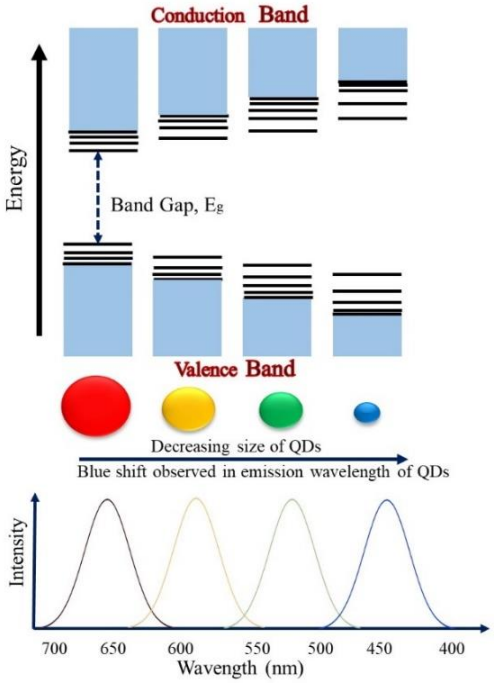

Figure 1.1. Scheme showing the influence of particle size on the band gap and photoluminescence wavelength due to quantum confinement in QDs

(b) *One dimensional nanomaterials (1D):* In these materials, the size is confined in the nanometer range for two of the three dimensions, while the third dimension is usually > 100 nm. Such materials tend to take needle or rod-like shapes. Nanowires, nanorods, nanotubes, nanobelts and nanoribbons fall into this category. Eg. carbon nanotubes (CNTs). Synthetic nanowires/nanorods are fabricated via various techniques like template approaches, spontaneous oriented attachments, electrospinning etc. The size, size dispersion, quality and composition of these 1D structures largely depend on the synthetic strategies

and conditions adopted during fabrication. These materials have a high length-to-diameter ratio that could effectively modulate their innate properties. They possess large specific surface area, high electron-hole separation efficiency, strong photoabsorption capabilities and efficient electron transport pathway that aid in photovoltaic, photoconducting and electrochemical applications.

(c) *Two dimensional nanomaterials (2D):* Materials who have confined size in one out of the three dimensions are termed as two-dimensional materials. These materials exhibit plate-like morphology where the thickness of the material is usually < 100 nm and other two dimensions are > 100 nm. 2D nanomaterials came to the forefront of research after the isolation of atomically thin layer of graphene from graphite in 2004[8]. The single atom thickness and confinement of electron in the 2D sheet structure without interlayer interaction offers exceptional electronic properties to the material. The enhanced specific surface areas and number of surface atoms associated with these materials also make them ideal for many surface-active applications like energy storage and catalysis[9].

(d) *Three dimensional nanomaterials (3D):* In these materials, the dimensions are not confined in the nanometer range. However, these bulk structures are comprised of various individual units, each within the nanometer dimensions. In this sense, 3D nanomaterials can be a bundle of nanowires, multiple nanolayers and even nanoparticle dispersions.

1.1.2. Effect of dimensions on the properties of nanomaterials

Nanomaterials have properties different from that of the bulk and these are tunable and size–dependent features of the materials. The elemental gold is a common example. Bulk solution of Au appears yellow in color while it is red or sometime purple in nanoscale[10]. The following set of properties have shown size dependent quantum confinement effects.

- Physical properties-Most of the nanomaterials have exceptionally good crystallinity. Due to restricted size, inter atomic spacing decreases. There exist a short-range repulsive force and a long-range electrostatic force. Hence, physical properties like melting point decreases with size.
- Mechanical properties- Nature of interfaces primarily dictate the mechanical attributes of the particles. Literature suggests that with reduction in size, mechanical properties such as hardness and toughness in metals/alloys, ductility and super plasticity in ceramics were increased[11,12].
- Chemical properties- Nanomaterials have larger surface to volume ratios in comparison with the bulk and therefore, most of the atoms are located on its surface. This result in improved reactivity and catalytic activity[13].
- Optical properties- The absorption and emission of semiconductor nanoparticles can be modulated by altering the size of the nanomaterial. For example, when the size of colloidal CdSe-CdS core-shell nanoparticles changes from 1.7 to 6 nm in diameter, the emission

wavelength of these particles shifts from blue to red end of the spectrum[10].

- Magnetic properties- Reports of non-magnetic elements like Au and Pt attaining magnetic properties in the nano regime are present in literature[14,15]. Also, the multi-domains in magnetic particles are reduced to single domains upon size restriction into the nano scale[16].
- Electrical properties- The band structure and charge carrier density of nanoparticles are completely different from the bulk. This further alters the electronic properties of the material[17].

1.2. SELENIUM NANOSTRUCTURES

1.2.1 Selenium

Jöns Jacob Berzelius, the 'father of Swedish chemistry' discovered element number 34 in 1818 while preparing sulfuric acid. The residue formed in the process was first mistook for the element Tellurium and it was later realized to have similar yet, different properties from Te. This new element was then named selenium, after the Greek word for moon '*selènè*'.

Selenium (Se) is a semi-metallic element belonging to period 4 and group 16 i.e., the chalcogen family. Placed between sulfur and tellurium, Se has properties intermediate to that of its family members. Se does not occur in its elemental form readily in nature. These are often found in ores like pyrite (i.e., metal sulfide ores) where Se partially replaces S. Naturally occurring selenium exist in inorganic (selenate and selenite) and organic composite forms like

selenomethionine and selenocysteine. Willoughby Smith discovered the photoconductivity of selenium (Se) in 1873 and Se solar cells devised in 1883 by Charles Fritts was the first solid-state photovoltaic construct. The semiconducting nature of grey selenium soon found various applications especially in rectifiers due to the enhanced efficiencies in comparison with copper oxide rectifiers. However, they were later replaced by much efficient and cheap silicon rectifiers by the 1970s. Nevertheless, contrary to semiconducting materials like Si and Ge that employs advanced micro and nanofabrication techniques, Se can be easily processed to perform multifaceted applications. Selenium is also an essential trace element for cellular functions in most mammals. Though selenium element itself is non-toxic, many of its compounds (like hydrogen selenide) can have adverse effects on living systems; with excessive exposure to Se causing selenosis i.e., selenium poisoning[18].

1.2.2. Selenium nanoparticles

Se nanoparticles (Se NPs) are spherical entities with diameter ranging in the order of nanometers. The application potential of Se NPs greatly depends on its crystal structure, dimensions and surface chemistry. Se NPs of amorphous, trigonal and monoclinic structures are studied experimentally. Out of these, amorphous Se NPs are highly stable structures and are widely reported due to its ease of formation. Se NPs absorb light mostly in the UV-visible range. The absorption spectrum as well as the emission wavelength can be tuned by controlling the size of these NPs due to quantum confinement effects. For

instance, Se NP with smaller diameters have an optical bandgap of approximately 2.5 eV or greater in comparison with ~2 eV observed for bulk Se.

1.2.3. Selenium quantum dots

Selenium quantum dots (Se QDs) are zero-dimensional spherical nanostructures with dimensions less than 10 nm. These materials exhibit remarkable optical, electrical, and structural properties due to quantum confinement and surface effects. Se QDs can exist in various crystal structure-cubic, amorphous, trigonal etc. depending on the synthesis route. Due to its smaller dimension, these materials have higher surface-to-volume ratio and the surface defects and/or chemistry in these materials dictates its properties. The optical bandgap of some of the smallest Se QDs may be greater than 3 eV, in comparison with 1.7- 2 eV reported for bulk, due to quantum confinement effects. As a result, Se QDs absorb light from the UV-visible region of the spectrum with band edge shifting with change in particle size. Size-tunable photoluminescence is also observed in some crystalline class of these materials.

1.2.4. Selenium nanowires/nanorods

Selenium nanowires and selenium nanorods are 1D and quasi-1D nanostructures, widely exploited for their optoelectronic properties. While Se nanowires are long, flexible thread-like structures with high aspect ratios with diameters in the order of nanometers, nanorods have smaller length-to-diameter ratio, making them rigid with a cylindrical appearance. These 1D nanostructures are typically comprised of trigonal phase of Se. The anisotropic nature of the

trigonal phase of Se favours growth in the [001] direction resulting in 1D structures. The optical bandgap of Se nanowires/nanorods, can be slightly higher due to quantum confinement, particularly for smaller diameters. These nanostructures absorb light in the visible and near-IR, with a significant absorption edge near 600–700 nm for bulk selenium and also exhibit photoluminescence. This absorption edge and PL emission wavelength can be fine-tuned with change in the diameter of the Se structures due to quantum confinement effects. These 1D Se structures with easy and efficient charge transport are ideal materials for photoconducting and photosensitive applications. A detailed review on various Se nanostructures including their synthesis and application is given in chapter-2.

1.3. CONDUCTING POLYMERS

Polymers were generally deemed as electrical insulators until the advent of conducting polymers or conjugate polymers. The Nobel Prize in Chemistry in 2000 awarded to Shirakawa, MacDiarmid and Heeger for their revolutionizing work in doped polyacetylene, triggered the interests of researchers in the area with numerous studies being published every year[19]. Intrinsically Conducting Polymer (CP) materials were identified to possess electrical conductivities optical properties similar to that of inorganic semiconductor materials or metals. CPs are widely exploited for their high processability, low cost, low density, better chemical functionalization capabilities and flexibility[20]. Typical examples of CPs include polyacetylene (PA), polyaniline (PANI), polypyrrole (PPy), poly (p-phenylenevinylene) (PPv), poly (p-phenylene) (PPp),

polythiophenes (PTh) and their derivatives. These polymers have a sequence of alternating single and double bonds (sp^2 hybridized structure) in their backbone, which results in delocalization of π-electrons along the entire polymer chain which imparts electrical conductivity to these materials.

1.3.1. Polyaniline

Originally known as 'aniline black', polyaniline refers to the oxidation product of aniline monomer. They are among the oldest yet most profound and most explored class of intrinsically conducting polymers. The exceptional environment and thermal stability, processibility, inexpensive precursors, unique doping/de-doping chemistry and good conductivity make them attractive candidates for multifunctional applications[21]. In contrast to other polymers like polythiophene or polypyrrole which have just two major oxidation states, polyaniline is known to have three states. The different states arise from the fact that polymer backbone is made of benzoid and quinoid ring structure that can exist in different proportions. The various states can be the fully reduced leucoemeraldine form (quinoid state), the fully oxidized pernigraniline (benzoid state) and the moderately oxidised emeraldine form (has an equal ratio of both benzoid and quinoid rings)[22]. The emeraldine form becomes conductive emeraldine salt when doped with an acid. The conductivity also depends on the concentration of the dopant and pH of the system (pH must be less than 3)[23]. The dopant however, does not form any bonds with the main chain of the polymer. In reality, under controlled reactions, polyaniline can attain oxidation to any degree. It can also be in intermediate half oxidation states,

protoemeraldine, which lies between leucoemeraldine and emeraldine, and nigraniline which lies between emeraldine and pernigraniline[20]. The various oxidation states can also be identified visually with their characteristic color. Leucoemeraldine is transparent/white; emeraldine state is green for the doped emeraldine salt, blue for the undoped emeraldine base; and pernigraniline appears deep violet.

Polyaniline is generally synthesized by chemical oxidation or electrochemical polymerization of aniline[24]. In chemical oxidation technique the monomer is oxidized in the presence of a suitable oxidizing agent like ammonium persulfate, ammonium peroxy disulfate, ceric sulfate etc. in the presence of dopant acids like HCl or H_2SO_4 under ambient conditions. The pitch-dark green precipitate obtained as the end product indicate the formation of polyaniline. In electrochemical polymerization, the monomers and electrolytes dissolved in a suitable solvent is electrodeposited upon oxidation (not using any chemical agents) on the surface of the electrode. Other popular synthesis procedures adopted include interfacial polymerization[25] or microemulsion methods[26] in which polymerization occurs at the interface of two immiscible liquids.

PANI is a versatile conducting polymer with multifaceted functions; the polymer and its hybrid composite find immense application in especially in chemical sensors[27], photovoltaic cells[28], energy storage devices[29], electromagnetic shielding systems[30], electrochromic[31] and even in anti-corrosion devices[32].

1.3.2. Conducting mechanism in polyaniline

The multiple redox states in PANI are instrumental in the conducting mechanism of the polymer and is responsible for the high conductivity and energy capacity in these materials. The states can be leucoemeraldine (LB) (completely reduced form), emeraldine (EB) (half-oxidised form), and pernigraniline (PB) (completely oxidized form) (**Figure.1.2**). The LB and PB forms are insulators while EB form of PANI becomes conducting once it is protonated to emeraldine salt (ES) form. Protonation simply means 'protonic acid doping' i.e., doping the species with any Lewis acid like HCl, HNO_3, H_2SO_4, H_3PO_4 etc. While protonation induce conductivity in EB by protonating the imine nitrogen, PB and LB forms of PANI remain insulating even after acid doping. The lone pair in the nitrogen atom in the quinonoid structure of PANI or the polaron (quasiparticle formed by the coupling of electron with phonon) plays a crucial role in the conductivity of the polymer. Upon complete protonation, bipolarons are generated which ultimately forms delocalized polaron lattice, termed as polysemiquinone radical cation site or two polarons. The conductivity of the material consequently increases even up to the order of 10^{10} S/cm[33]. Being conventionally semiconducting in nature, PANI often requires doping with some protic molecules to achieve high conductivity. However, it is to be noted that the nature and scale of dopant, presence of substitution groups in the chains and dryness of the sample has a direct consequence on the conductivity of the material[22]. In energy storage applications, during charging process, the polycation attract the negative ions

from the electrolyte and gets oxidized and p-doped while during discharge, polymers are reduced, n-doped with cations. Since these redox reactions occurs in the entirety of the polymer, energy is stored in the bulk of the PANI polymer[33].

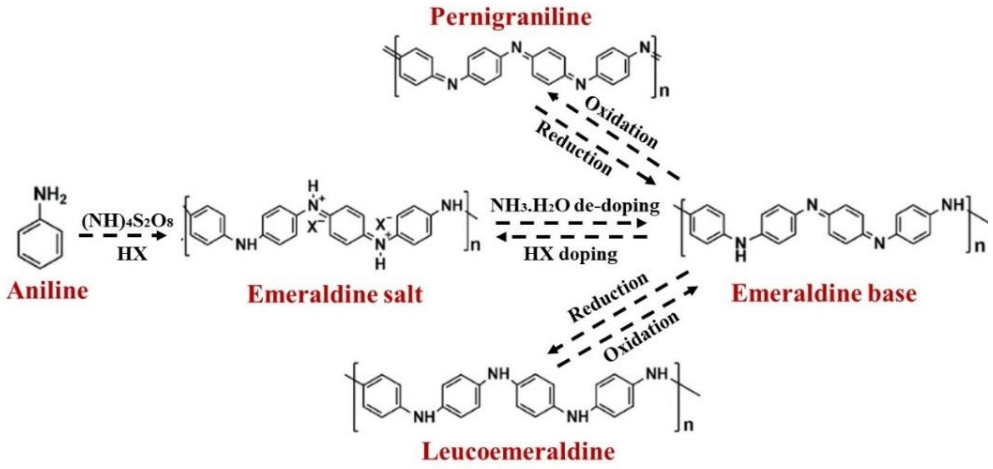

Figure 1.2. Different oxidation states of polyaniline and their interconversion.

1.4. NANOCOMPOSITES

1.4.1. Glass nanocomposites

Nanocomposite glasses can be termed as a hybrid material with two or more phases such that glass is the continuous host matrix and the dispersed phase/phases has dimensions less than 100 nm[34]. The embedded nanoparticles could be crystalline or amorphous. Solid glass matrix prevents the surface oxidation of the material providing chemical, thermal and mechanical stability to the nanostructures[35]. Also, doping the silica glasses with nanomaterials

retain the transparency of the matrix as nanometer sized particles scatter minimal light[36,37]. Conventionally, glass matrices are synthesized via melt quench technique which involves mixing of the precursor solution, melting them at very high temperatures and then rapidly cooling the melt to form glass. However, studies have evidenced that nanoparticles embedded silica are best fabricated via sol-gel route. The size of the pores of the silica xerogels play a vital role in the properties of the dispersed phase as the dimension of the pore dictates the size, growth and composition of the nanomaterial[38]. This fine tuning of pore dimensions is attained by altering the drying techniques and drying parameters during the synthesis of glass monoliths. Semiconductor nanomaterial in transparent silica host is popular among the research community as these materials exhibit multitude of applications in optical fibers, light emitting devices, passive laser elements, and even in non-linear optics[35].

1.4.2. Polymer nanocomposites

The polymeric backbone of conducting polymers is often criticized for their poor stability with various cycles of doping/de-doping. This short life would hinder the device application of these materials. One way to get around this problem is with composite formation. Conducting polymer nanocomposite consists of conjugated polymer as the primary component while an organic, inorganic or even biological entity acts as the secondary component. The secondary component or filler is generally in the nano dimension and hence the name nanocomposite. Fabrication of such materials combines the properties of both the constituents thereby resulting in enhance features of the end material.

Conducting polymer composites could be synthesized by any one of the three routes- ex-situ (the individual components are synthesized separately and then blended together to form composite), in-situ (at least one component of the composite is formed in presence of the other) or one-pot (the composite is formed in a single enclosure with monomers able to interact with the fillers). Ternary composites are also widely reported in literature that displays improved features than binary polymer composites.

1.4.2.1. Polyaniline nanocomposites

Polyaniline nanocomposites are an interesting class of intrinsically conducting polymers that exhibit improved properties in comparison with its individual components. The secondary component in the composite added to PANI could be metallic NPs, carbon entities like graphene, carbon nanotubes, metal oxide NPs, or even other polymers itself. The symbiotic relationship between such fillers and the polymer chain causes electronic interactions, charge transfers and even morphological modifications to the composite material[39]. The addition of the secondary component into the matrix can therefore not only enhance the existing properties but also render novel features to the material. For example, Qiu et.al, developed PANI/Fe_3O_4 composite via ultrasonic irradiation assisted chemical oxidative polymerization where the end composite showed magnetic properties in addition to the conductivity expected from PANI[40]. PANI nanocomposites are widely reported for electrochemical energy storage, biomedical applications, electromagnetic interference shielding,

catalytic applications etc. A detailed review of composites of PANI with selenium & cellulose, which is of interest in this work is given in the chapter 4.

1.5. SYNTHESIS OF NANOCOMPOSITES

There are various procedures that are widely opted for the synthesis of nanomaterials. High-throughput with sustained good quality is essential criteria for any synthesis technique. Generally, they are categorized into two-

- Top-Down method
- Bottom-up method

1.5.1. Top-down methods

In these methods the bulk material is leached out systematically and eventually results in the formation of smaller nanoparticles. The method includes mechanical milling/ grinding, physical vapor deposition, laser ablation, sputtering, anodization etc. These are generally termed ‘destructive’ in nature.

1.5.2. Bottom-up methods

Bottom-up approaches involve coalescence or assembling of the nanoparticles, atom by atom or molecule by molecule to generate the desired nanomaterial. In that sense, the method is ‘constructive’ in nature. Examples of bottom-up methods are chemical vapor deposition, sol–gel processing, solvothermal synthesis, pyrolysis and biogenic synthesis.

As the present thesis work involves materials synthesized via bottom-up methods like sol gel and solvothermal routes, these are discussed in detail.

1.5.2.1. Sol-gel method

Sol-gel is a wet chemical, bottom-up route that is widely used for the fabrication of nanomaterials. They are mostly adopted for the synthesis of metal oxide nanomaterials. The liquid precursor solution is transformed into a 'sol' which is a colloidal suspension of solid particles in the liquid. The suspension proceeds to forms an inorganic network in the continuous liquid phase which is termed as 'gel'. The sol-gel synthesis procedure is generally a two-step reaction – hydrolysis followed by condensation. Firstly, water or alcohol disintegrates the bonds in the metal oxide precursor solution (such as Tetraethyl Orthosilicate or TEOS) and forms sol. After this, condensation and polycondensation of the sol particles takes place due to which a network structure is formed increasing the solvent viscosity. The gel so formed is allowed to age during which polycondensation continues altering the structure, porosity and viscosity of the gel. Excess water and other volatile liquids are removed via drying. The product is also calcined to achieve nanoparticles. The sol can also be coated to form films, spun to obtain fibers or precipitated to get uniform powders so as to get the desired end structure of the material. The chemical reactions that progress during sol gel synthesis from metal alkoxides (≡M-OR) can be formally described by the following reactions

$\equiv M - OR + H_2O \rightarrow \equiv M - OH + ROH$ Hydrolysis

$\equiv M - OH + \equiv M - OR \rightarrow \equiv M - O - M \equiv + ROH$ Condensation

$\equiv M - OH + \equiv M - OH \rightarrow \equiv M - O - M \equiv + H_2O$ Condensation

Various parameters like water percentage, precursor to solvent ratio, reflux time, drying/calcinations temperature etc. also affects the final structure of the material. The drying process in sol-gel synthesis also play a vital role in the structure, porosity and properties of the end material. The removal of solvent from the mixture can be achieved by various drying techniques like evaporation drying, supercritical drying, freeze drying or aging assisted drying etc. In evaporation drying/ambient drying, the solvent is removed under ambient temperature and pressure, which results in a dense, non-porous *xerogel*. The capillary forces exerted by the liquid as it gets removed from the xerogel often causes shrinking and cracking of the matrix. The extend of this shrinkage can be reduced by adopting a slow rate of drying or by using drying control agents. Supercritical drying involves removal of the solvent from the medium by replacing it with a gas isolate at supercritical conditions resulting in the formation of an *aerogel*. The method prevents the shrinkage/cracking of the medium and retains the porosity, low density of the material. Freeze drying/lyophilization involves freezing of the sol-gel mixture followed by subliming the solvent under vacuum. This *cryogel* hence attains a highly porous structure with minimal shrinkage.

The sol gel method offers a facile route to synthesize homogeneous nanoparticles and even complex nanostructures even at low temperatures. A schematic diagram explaining the formation of various materials and its stages through sol-gel has been described in **Figure.1.3**.

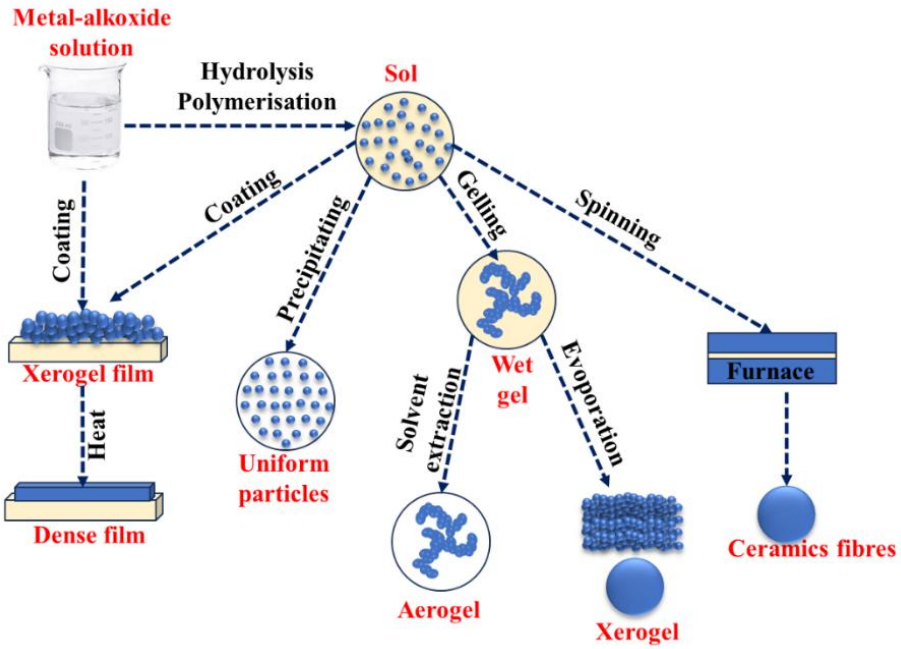

Figure 1.3. Schematic diagram showing the various stages of sol-gel synthesis.

1.5.2.2. Solvothermal method

It is a wet chemical method in which nanomaterials are synthesized via a heterogenous chemical reaction carried out in a sealed container under elevated levels of pressure and temperature ranging from 100°C to 250°C. The crystal growth typically takes place inside a steel pressure vessel termed as autoclave. The aqueous mixture of the precursors is heated above the boiling point of water increasing the pressure in the container. The synergistic effect of temperature and the autogenous pressure generated in the vessel results in the formation of nanomaterials with exceptional crystallinity even without any calcination[41]. It

also depends on the other factors like the presence of dissolved salts in the medium and the percentage of fill of the solvent in the vessel. Solvothermal synthesis is similar to the hydrothermal route with difference lying only in the wetting liquid used. While hydrothermal method proceeds through an aqueous medium, the wetting liquid is usually an organic solvent in solvothermal synthesis. Both these methods offer a one-step, scalable and inexpensive synthetic route that allows accurate control over crystallite size, dopants and nano-geometries of the material.

1.6. OPTICAL PROPERTIES OF NANOCOMPOSITES

Nanomaterials have a fascinating set of optical properties. Typically, these properties vary with size, shape, surface features, doping and even the interaction of the material with its surrounding environment.

1.6.1. UV-visible absorption studies

In semiconductor nanomaterials, when a light of photon energy greater or equal to the bandgap of the material ($h\nu \geq E_g$) is incident upon it, the photon gets absorbed. The electron in the valence band gets excited to the conduction band leaving behind a hole in the valence band. In case of incident photons with energies much greater than the band gap, the electron gets excited to higher levels of the conduction band away from the band edge. These electrons undergo non-radiative transitions to reach the tip of the conduction band and further annihilates the hole through radiative transition. The absorption in the material is governed by the Beer's law,

$$A = \log\left(\frac{I_0}{I}\right) = \varepsilon lc = \alpha \quad (1.1)$$

where A is the absorbance, I_o and I are the intensity of incident and transmitted light, c is the concentration of a solution and l is the path length of the sample, α is the absorption coefficient and ε is the molar absorptivity.

For solid samples, the above equation is derived for thickness of the sample.

For semiconductors, the optical bandgap of the material is evaluated from the Tauc plot after assessing the absorption edge from the UV-visible absorption spectrum. The Tauc relation is given as

$$(\alpha h\vartheta)^n = A\left(h\vartheta - E_g\right) \quad (1.2)$$

where hϑ is the photon energy, E_g is the bandgap energy, n depends on the nature of the electronic transition (e.g., for direct allowed transition n=2, for indirect allowed transition n=0.5). Here, α is the absorption co-efficient given by the relation

$$\alpha = \frac{2.303 * A}{d} \quad (1.3)$$

where A is the absorbance observed and d is the sample thickness.

Due to the discrete nature of the energy band QDs have very broad absorption in comparison with other organic fluorophores meaning that the material gets excited upon illumination with any source with energy greater than the emission band. This property becomes highly convenient for device applications as a single source can excite various QDs. The quantum confinement effects of QDs are also better understood from UV-Visible spectroscopy. Blue shift in the

energy band gap with increasing particle size is evidently observed in QDs. In case of non-semiconducting entities like carbon dots, the optical properties of the dots are dictated by the surface states and defects in contrast to band gap effect in QDs.

1.6.2. Photoluminescence

Photoluminescence concerns with emission of light by any substance due to electronic energy state transitions. Typically, the material absorbs light of a lower wavelength, moves to the excited state and emit light of a higher wavelength when it returns to the ground state. Photoluminescence can be classified as fluorescence or phosphorescence depending upon the mechanism involved. *Fluorescence* refers to the de-excitation of electron from an excited singlet state. The singlet-singlet transition is allowed by quantum mechanical considerations and the electron rapidly falls to the ground state with an excited state lifetime in the order of nanoseconds. On the contrary, *phosphorescence* is the emission of photons from triplet excited states. Electrons excited to the singlet excited state may transit to a triplet state via inter-system crossing. Here the excited electron has the same spin as the ground-state electron due to which transitions to the ground states are forbidden. Hence, de-excitation to the ground state is typically slower with excited state lifetimes in the order of milliseconds or seconds. Due to this, the fluorescence from a material stops immediately upon the removal of excitation source while light emission from phosphorescent materials continue to persist for some more time even after the excited light is switched off. Jablonski diagrams are typically used to understand the absorption,

excitation and emission in luminescent systems. **Figure 1.4** describes one such typical Jablonski diagram.

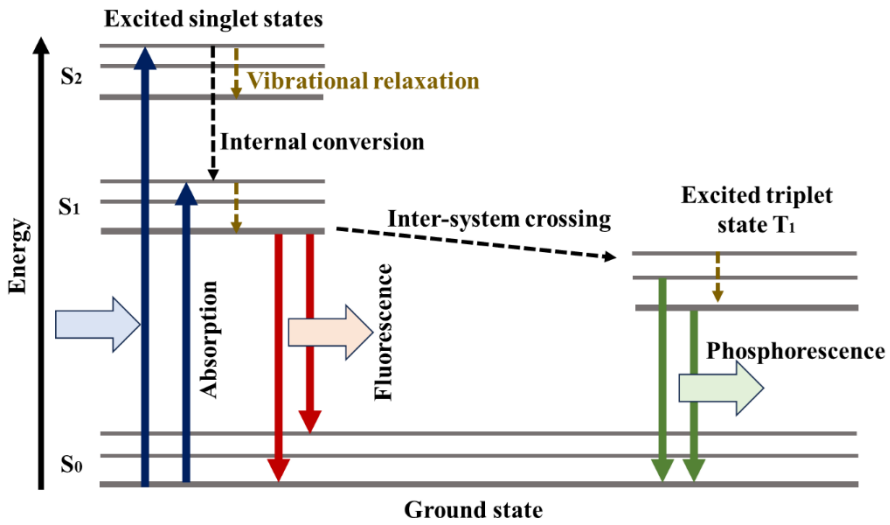

Figure 1.4. Jablonski diagram

1.6.3. Fluorescence

It is often noted that bulk materials are not luminescent while their nano versions show exceptional fluorescence properties. Fluorescence of nanomaterials have proven its utility in an array of applications like bio-imaging, in fluorescent sensors and light emitting devices. Depending on the nature of the nanomaterial, the origin of fluorescence can be different. In semiconductor nanomaterials like quantum dots, after absorption of incident light, the excited electron-hole pair recombines, crossing the band gap via a radiative or non-radiative transition. During radiative relaxation, a photon is

released whose energy matches with the band gap of the material. Upon non-radiative recombination, the fluorescence gets quenched in these materials.

Direct band gap semiconductors are considered the perfect candidates for photoluminescent applications. In such materials, the valence band maximum and conduction band minimum have the same *k* value or momentum. As a result, the radiative relaxation itself conserves momentum and do not require any phonons. However, in case of indirect band gap semiconductors, the valence band maxima and conduction band minima are not aligned in same momentum value and hence electron-hole recombination takes place in the mediation of a phonon to conserve momentum. Due to this, the band gap energy is taken away by the phonon as a result of which such transitions become non-radiative. Contrary to direct band gap semiconductors, indirect band gap materials have slow radiative and/or mostly non radiative recombination routes. They also have lower internal quantum yield. The fluorescence observed in semiconductor nanoparticles is size dependent. As a result, the optical properties of these materials can be tuned to desire by altering the shape or size of the fluorophore. With increasing size of the nanomaterial, the band gap decreases resulting in emission of photons towards longer wavelengths. A schematic representation of the band gap in semiconductors is given in **Figure.1.5**. In case of non-semiconducting nanomaterials like carbon dots, fluorescence has been thought to arise as a result of surface states, defects and passivation effects.

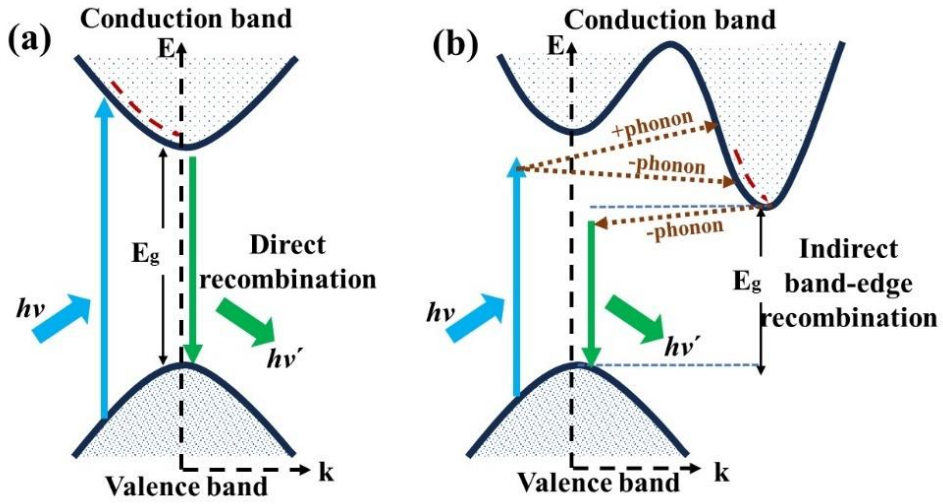

Figure 1.5. (a) Direct and (b) indirect band-gap in semiconductor materials

Fluorescence Quantum Yield (QY) is the ratio of number of photons absorbed to that emitted through fluorescence. It is a measure of how efficiently the material creates fluorescence from an excited photon. Both absolute and relative measurements of QY are possible. Generally, QY of a fluorophore is measured by comparing its photoluminescence with that of a reference sample of known QY. It is estimated by the following equation

$$Q = Q_R \frac{I}{I_R} \frac{A_R}{A} \tag{1.4}$$

where I and I_R are the integrated fluorescent intensities of the unknown and reference sample respectively, A and A_R are the corresponding absorbance value and Q_R is the quantum yield of the reference sample.

Prior studies indicate that QDs shows remarkable fluorescent quantum yields and stable luminescence in comparison with other organic fluorophores. Surface

defects like unsaturated dangling bonds and other disorders on the QDs have considerable effect on the fluorescent QY of the material. Increasing defects and disorders in the material reduces the efficiency of fluorescence and hampers with the stability by reducing the lifetime[42]. Research efforts have been focused on engineering these surface defects so as to improve the QY and fluorescence lifetime in these materials[43,44].

1.6.3.1. Fluorophores

Fluorophores are photoreactive molecules or molecular fragments that absorb light at a particular wavelength and re-emit at a higher wavelength. These could be intrinsic (naturally occurring eg.flavins, aromatic amino acids etc.) or extrinsic (added externally to generate fluorescence in the material eg.fluorescein, rhodamine etc.). Fluorophores can also be classified based on the type of source and structure of the material. These can be classified as organic fluorophores that contain some carbon-based compounds (eg.coumarins, cyanins), fluorescent proteins (eg.DsRed), quantum dots (eg.CdSe QDs), nanoparticle-based fluorophores (eg.gold, silica NPs) and synthetic/modified fluorophores (eg.Boron-dipyrromethene (BODIPY)). Absorption, excitation, emission of the fluorophore, luminescence quantum yield, excited state lifetime and photostability are key factors that govern the properties and application of a fluorophore. These fluorophores with unique fluorescent properties find immense application as labels and trackers in imaging, diagnostics and sensing applications.

1.6.3.2. Application of fluorescence

The fluorescence observed in fluorophores are widely exploited in the following areas.

- They are widely used as a diagnostic biomedical tool to detect damaged or affected tissue/cell through a non-invasive real-time imaging and can also track foreign entities like bacteria in the body helping to understand disease progression. Fluorescent guided surgeries are gaining pace in the medical front with surgeons using such markers to identify vital structures or cancerous tissues during surgery.
- The sensitivity, selectivity and rapid response of a fluorescer is often put into practical use in a fluorescent sensor which responds to minute changes in its environment in the presence of an analyte. Fluorophores are widely used in biosensors (eg. for detection of glucose, certain pathogens, DNA/RNA), chemical sensors which are sensitive to pH, presence of gas vapors like that of oxygen, ammonia, carbon dioxide even the presence of metal ions. The fluorescence-based sensing is also widely employed to asses for water quality monitoring (eg. oxygen levels, heavy metals, toxins), food quality control (for detecting adulterants) and detection of pollutants (eg. heavy metals, pesticides, organic contaminants) in soil and air.
- Fluorescence based techniques are also widely used to understand material structure, optimize synthesis and in the fabrication of advanced materials for optoelectronic applications. For instance, fluorescent

semiconductor QDs are widely employed to enhance the solar cell efficiency and enhancing display technologies.

- In the industrial sectors, fluorescence from materials is employed to ensure industrial efficiency, quality control and monitoring during manufacturing and other processes. They are used in surface defect detection and to check weld/solder joint in automotive or aerospace parts, leak detection in fluid systems or refrigeration/air conditioning units. In textile and paper industry, fluorophores called optical brightening agents and dyes are added to fabrics and paper to enhance the appearance and vibrancy of the material.
- Fluorescent inks are also used as security tags for counterfeit detection or invisible markers for identification of important documents/products. These inks are incorporated into currencies, documents and products and fluoresce only under UV illumination thereby ensuring authenticity.

1.7. ELECTROCHEMICAL PROPERTIES OF NANOMATERIALS

The growing energy demands and the simultaneous depletion of fossil fuel resources is undoubtedly one of the pressing concerns of the current century. Electrochemical energy storage system has been viewed as one of the promising solutions to the energy needs due to its high theoretical conversion efficiency of chemical energy to electrical energy. These devices also exhibited exceptional values of energy and power densities i.e, they can hold on to large amount of energy and even charge and discharge rapidly. Typically, all electrochemical devices consist of a pair of electrodes that shuttles and stores

ions between them and coupled with an external circuit. The electrode material used in the system tries to proves its mettle by providing sufficient amounts of electrons to the external circuit and ions to the electrode.

Batteries and capacitors are the conventionally used electrochemical energy storage devices. However, these have their own limitations. The redox reaction that occurs in the batteries takes place within the active material of the electrode and hence energy is itself stored in the bulk volume of the electrode. As a result, batteries can often afford energy densities even up to 100 $Whkg^{-1}$. Nevertheless, the poor solid-state ion-kinetics and low conductivity of the materials hinders easy charge-discharge in the material, lowering the power densities in batteries. Capacitors on the other hand have low energy densities and are generally suited for applications requiring high power delivery. Supercapacitors, which are also a type of electrochemical energy storage device attempts to achieve the best of both these categories and addresses energy storage as well as harvesting issues. Ideal supercapacitors are characterized by the long lifecycles, excellent power densities, high specific capacitance values thereby bridging the energy-power gap between conventional dielectric capacitors and fuel cells/batteries. This fact is illustrated in the Ragone plot (specific energy vs specific power graph) given in **Figure 1.6**.

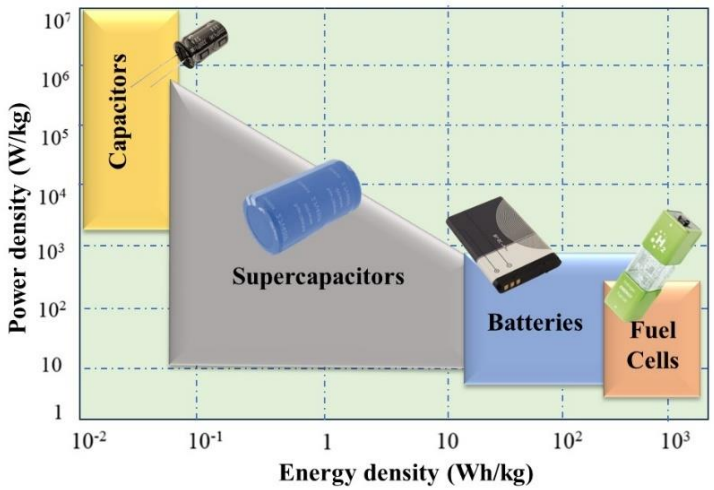

Figure 1.6. Ragone plot showing different energy storage devices

1.7.1 Classification of supercapacitors

The morphology of the active component of the electrode, the synthesis procedure opted, the nature of the electrolyte, separator and the design of the energy storage and harvest system plays a fundamental role in tuning the performance metrics of the supercapacitor. Regardless of the electrode material, the supercapacitance performance in a device can be understood to follow any one of the following three types.

1.7.1.1 Electrochemical double-layer capacitors (EDLCs)

Electrochemical double-layer capacitors or EDLCs store energy electrostatically or via a non-faradaic process. During the charging process, electrons move from negative to positive electrode through the circuit and the

excess or deficit of charges are accumulated at the electrode surface. Simultaneously, in the electrolyte, the cations travel towards the negative electrode and anions travel towards the positive electrode. The ions with enough magnitude to counterbalance the electron accumulation at the electrode gets collected in the electrolyte side thereby ensuring charge neutrality. These ions can layer into the pores of the electrode which possess opposite charge. Eventually, a double layer of capacitance is formed at the electrode-electrolyte interfaces where the charge is stored (**Figure 1.7 (a)**). The ions/electrons do not cross or exchange the interface at any point of charge/discharge thereby ensuring constant electrolyte concentration. During the discharge process, the ions are repelled and the reverse mechanism takes place. The fundamental equation governing the capacitance of a capacitor is

$$C = \frac{A\varepsilon_0\varepsilon_r}{d} \tag{1.5}$$

where the capacitance C is inversely proportional to the effective thickness of the electrical double layer d and directly proportional to the surface area A of the electrode, ε_0, ε_r being the permittivity of free space and relative permittivity of the dielectric material respectively. The specific capacitance in EDLCs similarly depend on the electrochemically active surface area of the material which is different from the specific area of the electrode. Hence materials with sufficient porosity with pore comparable to ion size that can provide accessible electrochemical active sites to the ions are generally preferred as electrodes. Literature has seen a spurge of efforts in this regard with most studies concentrated on carbonaceous electrode materials like graphene, carbon

aerogels, carbon nanotubes, carbon foams, activated carbon etc. Typically, aqueous and organic solvents are used as electrolytes in EDLCs.

EDLCs allows fast charge-discharge process that is stable and reversible even after 10^6 cycles as it do not involve any faradaic process. Consequently, the swelling of electrodes that is usually seen in batteries upon cycles of charge-discharge is eliminated. However, the major disadvantage of EDLCs is that they exhibit limited energy density with limited options for the choice of functional electrodes.

1.7.1.2. Pseudocapacitors

Pseudocapacitors store charge through faradaic process-i.e., the material undergoes rapid and reversible redox reaction at the interface. On application of a potential redox reaction occurs at the electrode and as a result charge transfers across the double layer. The faradaic current hence flows through the cell. The phenomenon is named 'pseudocapacitance' because the electrodes exhibit capacitive behaviour but the charge storage in these materials are a result of various reaction mechanisms (**Figure 1.7 (b)**). The charge (Q) stored in the system as a function of potential (V) is given by the equation

$$Q = CV \tag{1.6}$$

where C is called the specific capacitance measured in Fg^{-1} or Fcm^{-2}. Differentiating the equation with respect to time on both sides, we get,

$$I = C\frac{dV}{dt} \tag{1.7}$$

where *I* is the current. In addition to redox charge transfer, pseudocapacitance can also arise from underpotential deposition and intercalation pseudocapacitance. While the former is caused by the monolayer deposition of a foreign metal on the electrode, the latter involves rapid insertion of ions into the electrode. Conducting polymers like polyaniline (PANI), polypyrrol (PPy), polythiophene (PTh), their composites or derivatives and electroactive metal oxides like RuO_2 and MnO_2 are extensively used as electrodes in pseudocapacitors. These materials are endowed high value of specific capacitance and consequently high energy densities than EDLCs. However, due to repeated redox reaction at the interface, swelling and shrinkage of electrode takes place similar to batteries and hence these materials often suffer from poor mechanical stability shorter lifetime and lower power densities in comparison with EDLCs.

1.7.1.3. Hybrid capacitors

Hybrid supercapacitors exploit the advantages of EDLCs as wells as pseudocapacitor. With carefully chosen electrode combinations, these supercapacitors can exhibit exceptionally good energy and power densities. (**Figure 1.7(c)**). Depending upon the nature of the electrodes, these capacitors can be – asymmetric, battery type hybrid or composite hybrid supercapacitors.

- *Asymmetric hybrid supercapacitors* – It combines a EDLC electrode and a pseudocapacitor type electrode thereby coupling both faradaic and non-faradaic process in the system. i.e., one stores the charge by faradaic redox intercalation, while the other facilitates charge storage

by charge accumulation at the electrode-electrolyte interface. Such a configuration meets both power and energy density requirements of a supercapacitor. Generally, carbon-based materials like activated carbon (AC) are used as negative electrodes while metal-oxides or conducting polymer can be used as positive electrodes. Some examples of hybrid supercapacitors include AC//PbO_2, AC//$Ni(OH)_2$, AC//polyaniline etc.

- *Battery-type hybrid super capacitors* – It involves a battery-type electrode and a supercapacitor type electrode combined to give the benefits of both battery and supercapacitors. An example in this class is the lithium-ion capacitors, where one electrode is carbon-based and the other is lithium intercalated material.
- *Composite hybrid supercapacitors* – In these type of hybrid supercapacitors, both pseudocapacitor and EDLC materials are incorporated into a single electrode because of which the single electrode has physical and chemical mechanisms of energy storage within it. In such a configuration, generally, the carbon which is generally an EDLC material, contributes in charge transport, provides enhanced surface area to the composite while the pesudocapacitor component like metal-oxide contributes in charge storage. Depending on the number of constituents in the composite, they can also be classified as binary, ternary or even quaternary composites. Eg. Graphene/MnO_2, graphene/CNT/PANI.

Improved electrochemical performance metrics, cost effectiveness, better mechanical and cyclic stability and good working temperature window have stirred attention towards this class of materials in the recent years.

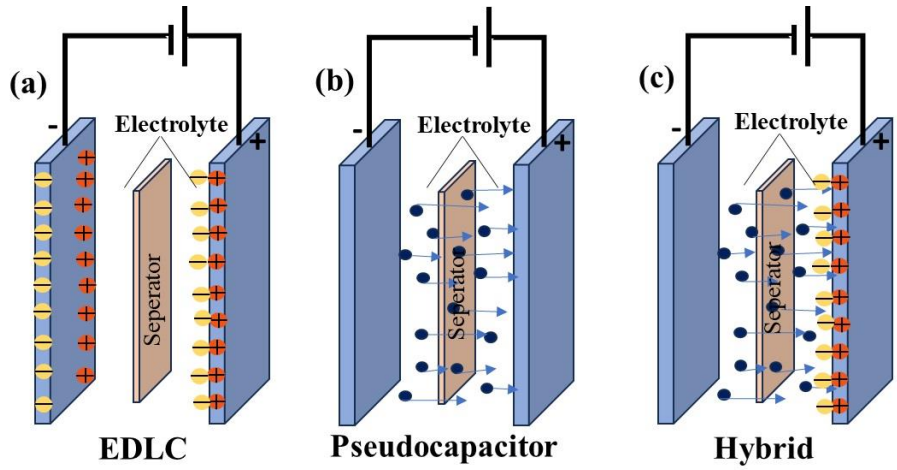

Figure 1.7. Types of supercapacitors (a) EDLC (b) pseudocapacitors (c) hybrid supercapacitors.

1.7.2. Applications of supercapacitors

Supercapacitors were primarily considered as energy storage devices. They have made attempts to bridge the gap between batteries that have high energy densities and ordinary capacitors renowned with exceptional power densities. Supercapacitors are widely exploited in various fields like energy storage, transportation, medicine, electronics, space expeditions etc. In electric and hybrid vehicles, SCs are currently being used as a backup for supply of power. Portable electronic devices like MP3 or smartphones, smartwatches and even many wearable sensors like health-bands in the market today exploit high

power densities of SCs. Miniaturized, flexible and wearable electronic devices that are often integrated into fabrics or our skin have stirred interests among the research fraternity for applications in wearable sensors, flexible solar cells, flexible detectors and even as a biocompatible energy replacement for batteries in pacemakers. The rapid power discharge in SCs have also found application in energy power backups in industries, in vehicle charging stations, laser equipped weapons in the military or defense and even unmanned expeditions in space projects. In addition to these, SCs are nowadays integrated with other devices or improvise in itself to perform multifunctional applications. SCs with self-repairing, self-charging, electrochromic and even mechanically deformable properties are extensively explored.

1.7.3. Nanocomposites for supercapacitor applications

Supercapacitor applications demand high surface area, good electrical conductivity, mechanical strength and electrochemical stability which is difficult to obtain in a single type of material. However, combining two or more nanomaterials can synergistically combine these properties, often outperforming individual materials. Few examples of such nanocomposites are metal oxide-based nanocomposites, conducting polymer-based nanocomposites, carbon-based nanocomposites, metal-organic framework (MOF)-based nanocomposites and hybrid nanocomposites. These composites often exhibit high pseudo capacitance from redox reaction among its components, improved mechanical stability as with carbon-based materials, increased surface area and tunable porosity with synthesis conditions as in the case of MOF components.

Nevertheless, the cost effectiveness, scalability and complexity of the synthesis routes of all these nanocomposite materials must be evaluated before practical device applications.

1.7.3.1. Graphene nanocomposites

Graphene is a monolayered, sp^2 hybridized, two-dimensional carbon sheet which have unique electrical, mechanical and thermal properties. It is known to possess a specific surface area of 2630 $m^2 g^{-1}$ and is one of the most conducting materials at room temperature with an electrical conductivity of the orders 10^6 S cm^{-1}[45]. However, graphene falls short of the high capacitance and energy density requirements for supercapacitor applications despite its long cyclic stability. Therefore, graphene is often combined with other pseudocapacitive materials to enhance its energy storage capabilities. Composites of graphene with metal oxides, carbon nanotubes, conducting polymers and Metal Organic Frameworks (MOFs) are widely explored by the research community for supercapacitor applications. Metal oxides like MnO_2[46], RuO_2[47], Fe_3O_4[48], NiO[49] with graphene exhibits improved capacitance due to pseudocapacitive and faradaic reactions. Sadak et al., reported MnO_2 nanoflowers electrochemically deposited on graphene paper exhibited high specific capacitance of 385.2 Fg^{-1} at 1 mVs^{-1}[50]. Bendable RuO_2/Gr/Cu electrode showed excellent specific capacitance of 1561 F g^{-1} (0.015 F cm^{-1}) at 5 mV s^{-1}, a high energy density of ∼13 Wh kg^{-1} at a power density of ∼21 kW kg^{-1} with excellent capacitance retention[51]. Conducting polymers like polyaniline (PANI), polypyrrole (PPy), and

polythiophene are also integrated with graphene to improve its properties. Xiao et al., had fabricated a unique sandwich-structured where PANI was electropolymerized on graphene paper and then wrapped with another layer of graphene to create graphene/polyaniline/graphene paper with excellent capacitance[52]. The symbiotic growth of p-type polypyrrole over functionalized graphene sheets has also shown to exhibit higher storage capacity than graphene-only films[53]. Carbon nanotubes (CNTs) acts as spacers between graphene layers preventing from restacking and also offer conductive pathways which also makes them ideal candidates as composite counterparts. MOFs on the other hands offers high surface area and tunable porosity to the composite improving ion diffusion and capacitance. A comprehensive review on MOF-graphene composite for supercapacitor applications was recently done by DK Singha et.al. which discusses the various synthetic routes and benefits of the nanocomposite for real-world energy storage application[54].

1.7.3.2. Polymer nanocomposites

Integration of a nanomaterial with a polymer not only reinforces the material but also impart novel properties to the polymer. These enhanced properties of the polymer largely depend on the synergy and interaction between these individual materials, their nature and synthesis routes. Often, conducting polymers possess good electrochemical capacitance but lack cyclic retention as the mechanical stability of the polymer chain tends to degrade over multiple cycles of charge-discharge. Hence, these materials are combined with other suitable components that offer mechanical stability to the end composite while

enhancing the specific capacitance. Widely used conducting polymer-based nanocomposites are polyaniline (PANI) nanocomposites, polypyrrole (PPy) nanocomposites and polythiophene (PTh) nanocomposites. Composites of polyaniline with graphene/reduced graphene oxide[55], CNTs[56], metal-oxides[57,58] and MOF structures[59,60] are widely reported in literature. A hybrid composition of three or more of these materials are also explored for energy storage capabilities. For example, free standing and flexible energy storage systems with ternary nanocomposites of reduced graphene oxide, polyaniline, and iron oxide was found to electrochemically outperform individual components[61]. Though PANI continue to dominate the supercapacitor domain, other polymer composites like that of PPy and PTh are also gaining wide attention. Dang et.al., recently reported rGO electrodeposited polypyrrole electrodes with maximum capacitance of 1091.2 $mFcm^{-2}$ at 1 $mAcm^{-2}$, with 93.3% capacitance retention, even under 180° bending[62]. Similarly, Zhang et.al., had recently fabricated a polythiophene derivative with very high specific capacitance of 1342 F g^{-1} at 4.0 A g^{-1}, with improved energy and power densities of 119.3 W h kg^{-1} and 38.83 kW kg^{-1}[63]. These advances in polymer nanocomposites make them ideal candidates for lightweight, portable, flexible and wearable electronics with enhanced electrochemical performance.

1.7.4. Electrochemical analysis

The electrochemical studies are carried out in electrolytic cell connected to an electrochemical work station. The electrochemical studies of SC devices are conducted in two and three-electrode systems. The three-electrode system evaluate the performance of the active component of the electrode in small quantities and hence the observed capacitance is solely dependent on the electrode material under study without the interference of any other electrode or configuration. The two-electrode set up on the contrary is similar to the device configuration set up and estimates the stability and efficiency of the material. It presents the capacitive performance of the effective cell including both electrodes in the configuration.

Three electrode configuration consists of working electrode (WE), counter electrode (CE) and reference electrode (RE) immersed in electrolyte and connected to a potentiostat (as depicted in **Figure 1.8(a)**). WE consist of the material under study which is usually conductive to ensure passage of charge. It is coated over a substrate electrode like Ni foam or glassy carbon after mixing with suitable binders. Pt electrodes are generally used as CE. RE is usually a stable and non-polarisable component. The potential of other electrode in the cell are measured with respect to the RE. Saturated calomel electrode (SCE), Ag/AgCl etc are the typical choices of RE. When a potential is applied to the WE, ideally, current flows between WE and CE completing the circuit and the voltage of WE is estimated in reference to the RE. In contrast to this, a two-

electrode configuration simply consist of a positive and negative electrode immersed in an electrolyte (**Figure. 1.8(b)**).

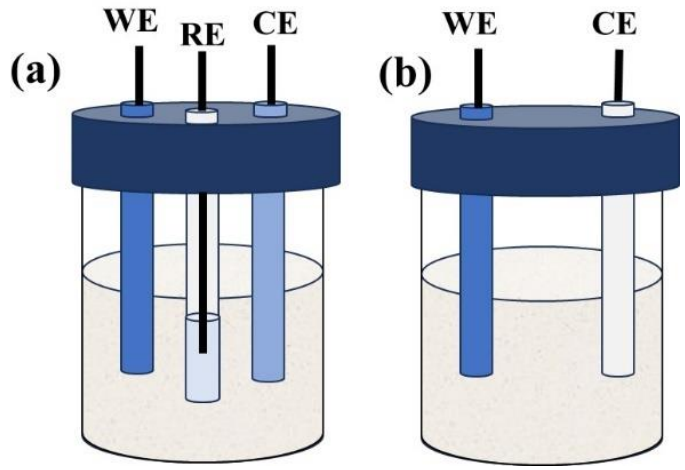

Figure 1.8. (a) Three and (b) Two electrode set up for electrochemical characterization

1.7.4.1. Cyclic Voltammetry

Cyclic voltammetry or CV is elemental in understanding the basic electrochemical nature of the material. It is a potential sweep technique in which the current is recorded by alternating the potential between two chosen limits at a constant scan rate. For forward scan, the system proceeds through a positive ramp signal which gets reversed after a half cycle. The CV plot gets inversed in this negative half, the system strives to attain equilibrium and tries to comes back to where it started. Another switch in the potential causes the cycle to repeat and hence the name ‘cyclic voltammetry’. The shape of typical cyclic voltammogram and position of the peaks can be used to understand the

electrochemical nature and redox potential of the materials. The specific capacitance (Fg^{-1}) of the electrodes can be estimated from these cyclic voltammograms using the equation

$$C = \frac{\int_{v1}^{v2} I(V)\, dV}{(\Delta V) v M} \tag{1.8}$$

where I represents the current (A), $v1$ and $v2$ are starting and ending voltages (V), ΔV represents the potential window (V), v is the scan rate (mV/s), M is the mass of active material of the electrode (g). The areal specific capacitance (Fcm^{-2}) can also be evaluated from a cyclic voltammogram by using the equation

$$C = \frac{\int_{v1}^{v2} I(V)\, dV}{2(\Delta V) v A} \tag{1.9}$$

where A is the area of the active electrode (cm^{-2}). Here $\int I(V)dV$ can be evaluated as the integrated area of the CV curve. In case of EDLC type supercapacitors, the CV curves are rectangular in shape with no positive or negative shifts in anodic and cathodic peaks. For pseudocapacitors, the voltammogram is nearly rectangular, with some inflection points which are ascribed to the oxidation-reduction in the material. Contrary to this, the battery-type materials have CV curves with obvious redox peaks.

1.7.4.2. Galvanostatic Charge-Discharge

It is the most efficient technique for capacitance estimation. In this technique, the potential is measured with respect to time at an applied current density. The specific capacitance (Fg^{-1} or Fcm^{-2}) of the electrode can be estimated from the GCD curve by the equation

$$C = \frac{I\Delta t}{\Delta V} \tag{1.10}$$

where I represents the current density (Ag^{-1} or Acm^{-2}), ΔV represents the potential window (V), Δt is the discharge time (s). The charge-discharge curves take a linear plot for EDLC materials indicating excellent capacitance while non-linearity and non-symmetry in the graph is observed for pseudocapacitor materials due to quasi-reversible faradic reactions. The battery-type energy storage materials have totally different type of GCD curves that are characterized by plateau-like regions. Rapid charge-discharge with negligible voltage drop during discharge is considered good electrochemical behavior. Illustration of typical cyclic voltammogram and galvanostatic discharging curves of EDLC, pseudocapacitor an batter-type energy storage devices is given in **Figure 1.9**.

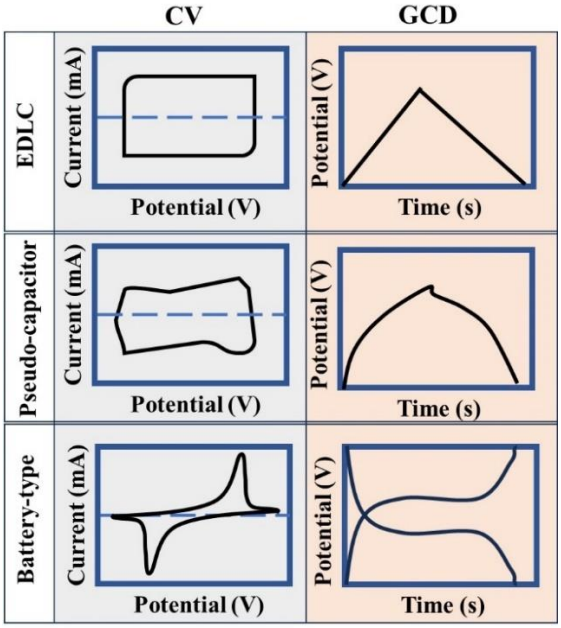

Figure 1.9. Cyclic voltammogram (CV) and galvanostatic discharging (GCD) curves of EDLC, pseudocapacitor and batter-type energy storage device

The specific energy density E (in $Whkg^{-1}$ or $Whcm^{-2}$) is given by the equation

$$E = \frac{1}{2} C (\Delta V)^2 \tag{1.11}$$

where C is the corresponding specific capacitance (Fg^{-1} or Fcm^{-2}) of the electrode. The power density P (Wkg^{-1} or Wcm^{-2}) is calculated from the energy density using

$$P = \frac{E}{\Delta t} \tag{1.12}$$

The Ragone plot (energy density vs. power density) is plotted using these values obtained from the GCD studies for performance evaluation and comparison of

supercapacitors. Cyclic stability or efficiency for multiple rounds of charge discharge is estimated from the degradation in specific capacitance of the fabricated electrode after any number of GCD cycles at a given current density. It is used to study the life time and longevity of the electrode material for practical applications.

1.7.4.3. Electrochemical Impedance Spectroscopy

The method is used to analyze the impedance or charge transfer kinetics associated with an electrochemical cell. A small sinusoidal voltage (with small amplitude) is applied to the electrode material and the current generated is measured over a wide range of frequencies at room temperature. The amplitude and phase of this signal is evaluated in comparison with applied voltage. The impedance values are then compared with an equivalent Randle's circuit as given in **Figure 1.10**. Here, C is the capacitance associated with the electrode, R_s is the resistance of the electrolyte, R_{ct} is the charge transfer resistance, and Z_w is the Warburg impedance (caused by diffusion). The Nyquist plots are the graphical representation of EIS data and typically consists of a high frequency and low frequency region. In the higher frequency region, a semicircle or arc is obtained, characteristics of faradaic reactions, whose intercept in the x-axis gives the charge transfer resistance of the material. In the lower frequency region, a straight-line nature of the EIS spectra was evident indicating capacitive behavior. This corresponds to the Warburg impedance which is associated with the diffusion of ions to the interior of the electrode from the electrolyte. The capacitance (C) can be calculated using equation

$$C = \frac{1}{2\pi f |Z|} \tag{1.13}$$

Where f gives the frequency and |Z| gives the imaginary part of impedance Z. The phase of the generated current was expressed using the Bode plot, which is plotted between Z_W along X-axis and phase shift θ or log |Z| along Y-axis.

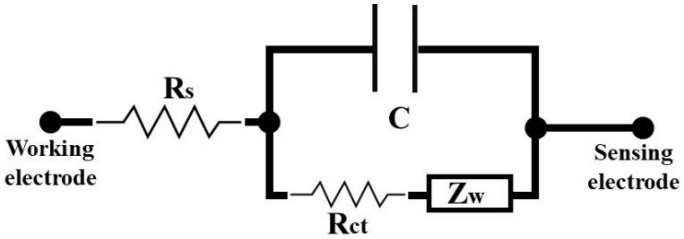

Figure 1.10. Randle's circuit

1.7.5. Challenges of supercapacitor

Though supercapacitors are endowed with a number of advantages and superior properties, certain shortcomings still hinder the road for commercial applications.

1. Low energy density- The energy density values of SCs is still lagging behind that of conventional batteries despite constant efforts. The gap is as large as 20 $Whkg^{-1}$ for supercapacitors and 30-200 $Whkg^{-1}$ for batteries. Improvised manufacturing processes, new electrolytes, novel electrochemically active electrode materials with improved accessible surface area are few expanses that can tackle the issue.

2. Non-ideal conditions- The practical applications of SCs should be able to accommodate the non-ideal parameters or factors that may affect the working of devices. For example, SCs used in military applications or space program equipment may be subjected to unusual environment or fluctuations and even accidental disturbance in the load.
3. Miniaturization and flexibility- The use of SCs in portable or wearable electronic devices requires that the electrodes are flexible at the same time have excellent capacitive performance with less mass loading to ensure check on the size of the device.
4. Device integration- Sustainable development has raised demands for materials with multifunctional applications with long life. Materials that integrate SCs with shape memory, transparency, electrochromic potential and self-repair abilities are highly preferred in comparison with conventional devices.

1.8. ORGANISATION OF THE THESIS

Nanostructure of different allotropes are always a subject of growing research because slight modification in their structural arrangement result in drastic changes in their physical properties. The thesis presented is directed to understand the material structure and formation of different selenium allotropes. The work has been focused on different composites of Se in silica xerogel and polyaniline, for optical sensing and electrochemical storage applications respectively. A brief introduction about the various synthesis techniques and

optical, electrochemical properties of materials and their analysis is discussed in this chapter. Chapter 2 discusses the formation of four different allotropic forms of Se sol-gel based synthesis. A comparative study of the structural and preliminary cytotoxic activity is conducted. In chapter 3, trigonal selenium quantum dots synthesized by a solvothermal assisted sol-gel route is used for the solid-state fluorescent sensing of curcumin. Detail discussion of the structure, defects observed in the material and optical sensing mechanism is also presented. Chapter 4 discusses the synthesis and structural characterization of Se in PANI/Cellulose-PANI composites. Chapter 5 presents the electrochemical energy storage studies of Se/PANI/Cellulose composite. Chapter 6 and 7 gives the conclusion of the studies performed and some future perspectives and opportunities respectively.

1.9. OBJECTIVES OF THE RESEARCH WORK

- ✓ To synthesis nanocrystalline allotropes selenium in silica matrix and study cytotoxicity of selenium allotropes
- ✓ To investigate phase transformation related structural and optical properties of obtained Se-SiO_2 composites.
- ✓ To explore the optical properties of nanocrystalline Se allotropes and design a fluorescence sensor for quantitative determination of curcumin.
- ✓ To synthesis selenium- conducting polymer hybrid nanocomposite for energy storage applications.
- ✓ To modify properties of PANI and Cellulose/PANI in the presence of nanocrystalline selenium.

1.10. REFERENCES

[1] Martynenko IV, Litvin AP, Purcell-Milton F, Baranov AV, Fedorov AV, Gun'ko YK. Application of semiconductor quantum dots in bioimaging and biosensing. J Mater Chem B 2017;5:6701–27. https://doi.org/10.1039/C7TB01425B.

[2] Kumar S, Nehra M, Deep A, Kedia D, Dilbaghi N, Kim K-H. Quantum-sized nanomaterials for solar cell applications. Renew Sustain Energy Rev 2017;73:821–39. https://doi.org/10.1016/j.rser.2017.01.172.

[3] Jang E, Jang H. Review: Quantum Dot Light-Emitting Diodes. Chem Rev 2023;123:4663–92. https://doi.org/10.1021/acs.chemrev.2c00695.

[4] Jung H, Ahn N, Klimov VI. Prospects and challenges of colloidal quantum dot laser diodes. Nat Photonics 2021;15:643–55. https://doi.org/10.1038/s41566-021-00827-6.

[5] Heindel T, Kim J-H, Gregersen N, Rastelli A, Reitzenstein S. Quantum dots for photonic quantum information technology. Adv Opt Photonics 2023;15:613–738. https://doi.org/10.1364/AOP.490091.

[6] Ma Q, Su X. Recent advances and applications in QDs-based sensors. Analyst 2011;136:4883–93. https://doi.org/10.1039/C1AN15741H.

[7] The Nobel Prize in Chemistry 2023. NobelPrizeOrg n.d. https://www.nobelprize.org/prizes/chemistry/2023/press-release/ (accessed May 5, 2024).

[8] Novoselov KS, Geim AK, Morozov SV, Jiang D, Zhang Y, Dubonos SV, et al. Electric Field Effect in Atomically Thin Carbon Films. Science 2004. https://doi.org/10.1126/science.1102896.

[9] Zhang H. Ultrathin Two-Dimensional Nanomaterials. ACS Nano 2015;9:9451–69. https://doi.org/10.1021/acsnano.5b05040.

[10] Roduner E. Size matters: why nanomaterials are different. Chem Soc Rev 2006;35:583. https://doi.org/10.1039/b502142c.

[11] Huang Q, Bando Y, Xu X, Nishimura T, Zhi C, Tang C, et al. Enhancing Superplasticity of Engineering Ceramics by Introducing BN Nanotubes. Nanotechnol Nanotechnol 2007;18:485706–7. https://doi.org/10.1088/0957-4484/18/48/485706.

[12] Ramachandra M, Abhishek A, Siddeshwar P, Bharathi V. Hardness and Wear Resistance of ZrO2 Nano Particle Reinforced Al Nanocomposites Produced by Powder Metallurgy. Procedia Mater Sci 2015;10:212–9. https://doi.org/10.1016/j.mspro.2015.06.043.

[13] González-Rovira L, Sánchez-Amaya JM, López-Haro M, del Rio E, Hungría AB, Midgley P, et al. Single-Step Process To Prepare CeO2 Nanotubes with Improved Catalytic Activity. Nano Lett 2009;9:1395–400.https://doi.org/10.1021/nl803047b.

[14] Nakae Y, Seino Y, Teranishi T, Miyake M, Yamada S, Hori H. Anomalous spin polarization in Pd and Au nano-particles. Phys B Condens Matter 2000;284–288:1758–9. https://doi.org/10.1016/S0921-4526(99)02928-2.

[15] Yamamoto Y, Miura T, Nakae Y, Teranishi T, Miyake M, Hori H. Magnetic properties of the noble metal nanoparticles protected by polymer. Phys B Condens Matter 2003;329–333:1183–4. https://doi.org/10.1016/S0921-4526(02)02102-6.

[16] Caizer AssocPC. Nanoparticle Size Effect on Some Magnetic Properties, 2015, p. 475–519. https://doi.org/10.1007/978-3-319-15338-4_24.
[17] Zhang Y, Wang E, Li H, Cai Y, Zhang J. Enhanced electrical properties in 0–3 pyroelectric composites doped with nano carbon black powder. J Mater Sci Mater Electron 2015;26:37–41. https://doi.org/10.1007/s10854-014-2359-3.
[18] Boyd R. Selenium stories. Nat Chem 2011;3:570–570. https://doi.org/10.1038/nchem.1076.
[19] The Nobel Prize in Chemistry 2000. NobelPrizeOrg n.d. https://www.nobelprize.org/prizes/chemistry/2000/summary/ (accessed May 6, 2024).
[20] Baker CO, Huang X, Nelson W, Kaner RB. Polyaniline nanofibers: broadening applications for conducting polymers. Chem Soc Rev 2017;46:1510–25. https://doi.org/10.1039/C6CS00555A.
[21] Li D, Huang J, Kaner RB. Polyaniline Nanofibers: A Unique Polymer Nanostructure for Versatile Applications. Acc Chem Res 2009;42:135–45. https://doi.org/10.1021/ar800080n.
[22] K N, Sekhar Rout C. Conducting polymers: a comprehensive review on recent advances in synthesis, properties and applications. RSC Adv 2021;11:5659–97. https://doi.org/10.1039/D0RA07800J.
[23] Wang Y, Levon K. Influence of Dopant on Electroactivity of Polyaniline. Macromol Symp 2012;317–318:240–7. https://doi.org/10.1002/masy.201200008.
[24] Tran HD, Li D, Kaner RB. One-Dimensional Conducting Polymer Nanostructures: Bulk Synthesis and Applications. Adv Mater 2009;21:1487–99. https://doi.org/10.1002/adma.200802289.
[25] Zhang X, Chan-Yu-King R, Jose A, Manohar SK. Nanofibers of polyaniline synthesized by interfacial polymerization. Synth Met 2004;145:23–9. https://doi.org/10.1016/j.synthmet.2004.03.012.
[26] Yan F, Xue G. Synthesis and characterization of electrically conducting polyaniline in water–oil microemulsion. J Mater Chem 1999;9:3035–9. https://doi.org/10.1039/A905146E.
[27] Huang J, Virji S, Weiller BH, Kaner RB. Polyaniline Nanofibers: Facile Synthesis and Chemical Sensors. J Am Chem Soc 2003;125:314–5. https://doi.org/10.1021/ja028371y.
[28] Sönmezoğlu S, Taş R, Akın S, Can M. Polyaniline micro-rods based heterojunction solar cell: Structural and photovoltaic properties. Appl Phys Lett 2012;101:253301. https://doi.org/10.1063/1.4772019.
[29] Wang H, Lin J, Shen ZX. Polyaniline (PANi) based electrode materials for energy storage and conversion. J Sci Adv Mater Devices 2016;1:225–55. https://doi.org/10.1016/j.jsamd.2016.08.001.
[30] He Z, Xie H, Wu H, Chen J, Ma S, Duan X, et al. Recent Advances in MXene/Polyaniline-Based Composites for Electrochemical Devices and Electromagnetic Interference Shielding Applications. ACS Omega 2021;6:22468–77. https://doi.org/10.1021/acsomega.1c02996.

[31] Ghosh T, Bansal L, Kandpal S, Rani C, Tanwar M, Kumar R. Ambipolar All-Organic Solid-State Electrochromic Device Using Electrodeposited Polyaniline: Improving Performance by Design. ACS Appl Opt Mater 2023;1:473–80. https://doi.org/10.1021/acsaom.2c00115.

[32] Cai K, Zuo S, Luo S, Yao C, Liu W, Ma J, et al. Preparation of polyaniline/graphene composites with excellent anti-corrosion properties and their application in waterborne polyurethane anticorrosive coatings. RSC Adv 2016;6:95965–72. https://doi.org/10.1039/C6RA19618G.

[33] Heme HN, Alif MSN, Rahat SMSM, Shuchi SB. Recent progress in polyaniline composites for high capacity energy storage: A review. J Energy Storage 2021;42:103018. https://doi.org/10.1016/j.est.2021.103018.

[34] Karmakar B. Chapter 1 - Fundamentals of Glass and Glass Nanocomposites. In: Karmakar B, Rademann K, Stepanov AL, editors. Glass Nanocomposites, Boston: William Andrew Publishing; 2016, p. 3–53. https://doi.org/10.1016/B978-0-323-39309-6.00001-8.

[35] Xia M, Luo J, Chen C, Liu H, Tang J. Semiconductor Quantum Dots-Embedded Inorganic Glasses: Fabrication, Luminescent Properties, and Potential Applications. Adv Opt Mater 2019;7:1900851. https://doi.org/10.1002/adom.201900851.

[36] Kajihara K. Recent advances in sol–gel synthesis of monolithic silica and silica-based glasses. J Asian Ceram Soc 2013;1:121–33. https://doi.org/10.1016/j.jascer.2013.04.002.

[37] Blanc W, Martin I, Francois-Saint-Cyr H, Bidault X, Chaussedent S, Hombourger C, et al. Compositional Changes at the Early Stages of Nanoparticles Growth in Glasses. J Phys Chem C 2019;123:29008–14. https://doi.org/10.1021/acs.jpcc.9b08577.

[38] Gurin VS, Alexeenko AA, Yumashev KV, Prokoshin PV, Zolotovskaya SA, Zhavnerko GA. Structure and optical properties of CuxO- and CuxSe-doped sol–gel silica glasses. Mater Sci Eng C 2003;23:1063–7. https://doi.org/10.1016/j.msec.2003.09.073.

[39] Sen T, Mishra S, Shimpi NG. Synthesis and sensing applications of polyaniline nanocomposites: a review. RSC Adv 2016;6:42196–222. https://doi.org/10.1039/C6RA03049A.

[40] Qiu G, Wang Q, Nie M. Polyaniline/FE3O4 magnetic nanocomposite prepared by ultrasonic irradiation. J Appl Polym Sci 2006;102:2107–11. https://doi.org/10.1002/app.24100.

[41] Walton RI. Subcritical solvothermal synthesis of condensed inorganic materials. Chem Soc Rev 2002;31:230–8. https://doi.org/10.1039/B105762F.

[42] Jiang R, Wu H, Manzani D, Zhang W, Liu C. Effect of surface defects on photoluminescence properties of CdSe quantum dots in glasses. Appl Surf Sci 2023;622:156931. https://doi.org/10.1016/j.apsusc.2023.156931.

[43] Duncan TV, Méndez Polanco MA, Kim Y, Park S-J. Improving the Quantum Yields of Semiconductor Quantum Dots through Photoenhancement Assisted by Reducing Agents. J Phys Chem C 2009;113:7561–6.

https://doi.org/10.1021/jp811245r.
[44] Grabolle M, Ziegler J, Merkulov A, Nann T, Resch-Genger U. Stability and Fluorescence Quantum Yield of CdSe–ZnS Quantum Dots—Influence of the Thickness of the ZnS Shell. Ann N Y Acad Sci 2008;1130:235–41. https://doi.org/10.1196/annals.1430.021.
[45] Chang H, Wu H. Graphene-based nanocomposites: preparation, functionalization, and energy and environmental applications. Energy Environ Sci 2013;6:3483–507. https://doi.org/10.1039/C3EE42518E.
[46] Chen S, Zhu J, Wu X, Han Q, Wang X. Graphene Oxide−MnO2 Nanocomposites for Supercapacitors. ACS Nano 2010;4:2822–30. https://doi.org/10.1021/nn901311t.
[47] Han ZJ, Pineda S, Murdock AT, Seo DH, Ostrikov K (Ken), Bendavid A. RuO2-coated vertical graphene hybrid electrodes for high-performance solid-state supercapacitors. J Mater Chem A 2017;5:17293–301. https://doi.org/10.1039/C7TA03355A.
[48] Liao J, Li Y, Wang Z, Lv L, Chang L. In-situ preparation of Fe3O4/graphene nanocomposites and their electrochemical performances for supercapacitor. Mater Chem Phys 2021;258:123995. https://doi.org/10.1016/j.matchemphys.2020.123995.
[49] Zhu Y-G, Cao G-S, Sun C-Y, Xie J, Liu S-Y, Zhu T-J, et al. Design and synthesis of NiO nanoflakes/graphene nanocomposite as high performance electrodes of pseudocapacitor. RSC Adv 2013;3:19409–15. https://doi.org/10.1039/C3RA42091D.
[50] Sadak O, Wang W, Guan J, Sundramoorthy AK, Gunasekaran S. MnO2 Nanoflowers Deposited on Graphene Paper as Electrode Materials for Supercapacitors. ACS Appl Nano Mater 2019;2:4386–94. https://doi.org/10.1021/acsanm.9b00797.
[51] Cho S, Kim J, Jo Y, Ahmed ATA, Chavan HS, Woo H, et al. Bendable RuO2/graphene thin film for fully flexible supercapacitor electrodes with superior stability. J Alloys Compd 2017;725:108–14. https://doi.org/10.1016/j.jallcom.2017.07.135.
[52] Xiao F, Yang S, Zhang Z, Liu H, Xiao J, Wan L, et al. Scalable Synthesis of Freestanding Sandwich-structured Graphene/Polyaniline/Graphene Nanocomposite Paper for Flexible All-Solid-State Supercapacitor. Sci Rep 2015;5:9359. https://doi.org/10.1038/srep09359.
[53] de Oliveira HP, Sydlik SA, Swager TM. Supercapacitors from Free-Standing Polypyrrole/Graphene Nanocomposites. J Phys Chem C 2013;117:10270–6. https://doi.org/10.1021/jp400344u.
[54] Kanti Singha D, Ipsita Mohanty R, Bhanja P, Kumar Jena B. Metal–organic framework and graphene composites: advanced materials for electrochemical supercapacitor applications. Mater Adv 2023;4:4679–706. https://doi.org/10.1039/D3MA00523B.

[55] Wang L, Lu X, Lei S, Song Y. Graphene-based polyaniline nanocomposites: preparation, properties and applications. J Mater Chem A 2014;2:4491–509. https://doi.org/10.1039/C3TA13462H.
[56] Kumar A, Kumar V, Awasthi K. Polyaniline–Carbon Nanotube Composites: Preparation Methods, Properties, and Applications. Polym-Plast Technol Eng 2018;57:70–97. https://doi.org/10.1080/03602559.2017.1300817.
[57] Singu BS, Palaniappan S, Yoon KR. Polyaniline–nickel oxide nanocomposites for supercapacitor. J Appl Electrochem 2016;46:1039–47. https://doi.org/10.1007/s10800-016-0988-3.
[58] Jaidev, Jafri RI, Mishra AK, Ramaprabhu S. Polyaniline–MnO2 nanotube hybrid nanocomposite as supercapacitor electrode material in acidic electrolyte. J Mater Chem 2011;21:17601. https://doi.org/10.1039/c1jm13191e.
[59] Udayan APM, Sadak O, Gunasekaran S. Metal–Organic Framework/Polyaniline Nanocomposites for Lightweight Energy Storage. ACS Appl Energy Mater 2020;3:12368–77. https://doi.org/10.1021/acsaem.0c02376.
[60] Vinodh R, Babu RS, Sambasivam S, Gopi CVVM, Alzahmi S, Kim H-J, et al. Recent Advancements of Polyaniline/Metal Organic Framework (PANI/MOF) Composite Electrodes for Supercapacitor Applications: A Critical Review. Nanomaterials 2022;12:1511. https://doi.org/10.3390/nano12091511.
[61] Martins VHN, Siqueira NMS, Fonsaca JES, Domingues SH, Souza VHR. Ternary Nanocomposites of Reduced Graphene Oxide, Polyaniline, and Iron Oxide Applied for Energy Storage. ACS Appl Nano Mater 2021;4:5553–63. https://doi.org/10.1021/acsanm.1c01036.
[62] Dang F, Cai Y, Yang P. Electrodeposition of Graphene/Polypyrrole Electrode for Flexible Supercapacitor with Large Areal Capacitance. ACS Appl Energy Mater 2024;7:5832–8. https://doi.org/10.1021/acsaem.4c00968.
[63] Zhang Y, Zhang H, Ming S, Lin P, Yu R, Xu T. Ultra-Stable High-Capacity Polythiophene Derivative for Wide-Potential-Window Supercapacitors. ACS Appl Mater Interfaces 2024;16:22571–9. https://doi.org/10.1021/acsami.4c02684.

Chapter-2

Synthesis and characterization of selenium allotropes in silica matrix

Synthesis of different allotropes of same element by changing the experimental condition is often interesting and challenging. Herein, nanomaterials of selenium are synthesized in a silica matrix via sol-gel and sol-gel assisted solvothermal route. The four polymorphs of Se (cubic, amorphous, trigonal and monoclinic) are synthesized by the decomposition of selenous acid by altering the synthesis parameters. The characteristic resonance peaks in Raman spectra, lattice fringes observed in High-Resolution Transmission Electron Micrographs and Selected Area Diffraction data are used to differentiate the various crystalline and amorphous forms of Se. The optical bandgaps of cubic, amorphous, trigonal and monoclinic Se QDs are found to be 3.6 eV, 2.18 eV, 1.64 eV and 2.13 eV respectively. The cell viability studies of Se QDs in silica is also conducted using in vitro cytotoxic studies in rat spleen cells. All nanocrystalline forms of Se shows cell viabilities up to >90% for concentrations up to 100 µg/L. Being highly versatile and biocompatible, these elemental allotropes of selenium have potential applications in various bio-photonic and opto-electronic devices.

2.1. INTRODUCTION

Study of elemental allotropes has always been one of the promising areas in the field of material science. This is mainly due to the fact that though allotropes are different forms of the same element, they could have totally unrelated and wide range of properties. Nanostructure of different allotropes is always a subject of growing research because a slight modification in the structural arrangement might cause drastic changes in their physical properties. The study also opens new avenues in understanding of material structure, its properties and potential application. A very suitable example in this context is that of carbon. Diamond, graphite, fullerenes, carbon nanotubes, and relatively recent discovery of graphene triggered minds for all possible carbon modification and their potential use in nanoelectronics, sensors, nanocomposites, batteries and supercapacitors. In addition to these polymorphs, various combination of sp-, sp^2- and sp^3-hybridized carbon atoms results in the formation of new synthetic allotropes like graphyne, carbyne etc[1]. Despite being similar in composition, each of these aforementioned allotropes have different atomic arrangement within it and hence exhibit diverse applications. For instance, while diamond is an insulator with exceptional hardness, CNT and graphene is known for their conductivity and flexibility.

Another example that can be considered is that of Phosphorus. Each allotrope of P varies in its reactivity and stability. White P is highly reactive

species, a phosphorescent material with increased level of toxicity. Thermal treatment of white P yields red P which is relatively more stable and less toxic than white P. Black phosphorus is the most stable form of P and has a layered, sheet-like structure with atoms in a puckered honeycomb arrangement similar to graphite. Exfoliation of bulk black phosphorus remains the most common route for Phosphorene which is basically a single layer of black P. Other complex structural variants of P, especially blue P is currently explored. Hence, various polymorphs of an element are materials that possess immense scope for multifunctional applications due to its versatility. Presence of discrete energy state, tunable band-gap and enhanced opto-electronic properties have always hyped up the potential of their zero-dimensional elemental quantum dots (QDs) compared to its other dimensional peers.

2.1.1. Selenium allotropes

Elemental selenium (Se^0) has always been a vital component in the electronic industry and often finds application in various realms of science. Being one among the first photoelectric substances discovered, these were widely used in solar cells[2], xerography[3] and even imaging[4]. Se exists in various allotropic forms including five crystalline and two non-crystalline forms. The crystalline forms are namely cubic (α, β and fcc), hexagonal, monoclinic (α, β and γ), orthorhombic and rhombohedral[5]. The non crystalline forms can be amorphous (red or black) and vitreous. The molecular structure of

different allotropes is different. For example, monoclinic Se consists nearly identical puckered cyclo-octaselenium (Se_8) rings with discrete packaging. It is usually wine-red in color and the ring arrangement/packaging in the structure can further result in three forms-α, β and γ[6]. The grey-colored hexagonal/trigonal Se has helical polymeric chain structure with atoms connected by covalent bonds aligned in the c-axis where adjacent chains are bonded by a weak van der Waals interaction. This trigonal structure is characterized by three atoms per turn in its helix, which is strongly biased to grow along c-axis into 1D structure. It is the most stable among all other forms at room temperature[7]. The red and black amorphous forms of Se are characterized by the abundance of Se_8 rings and Se_8 chains respectively in them. These different chain/ rings characteristics of all the aforementioned polymorphs have a direct consequence on the electronic structure and properties of the allotropes. For instance, cubic Se has a band gap energy of approximately 3.5 eV due to which it acts as an insulator while trigonal and monoclinic Se has an optical bandgap around 2 eV making it a semiconductor.

The crystalline forms of Se, especially trigonal Se, with its ordered arrangement and smaller bandgap, higher mobility and easy charge transport can absorb more light. Hence these polymorphs are widely studied for applications in solar cells. On the contrary, the amorphous Se structures are renowned with higher resistivities and hence find immense applications in detectors and imaging devices.

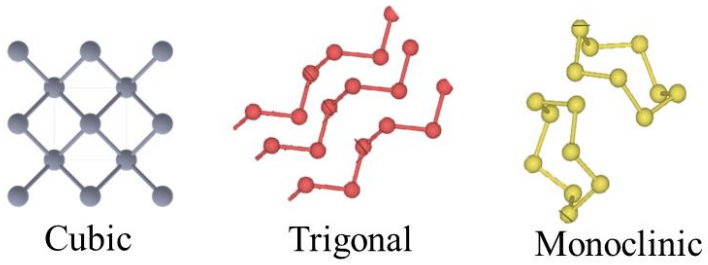

Figure-2.1.- Structure of some crystalline Se allotropes.

2.1.2. Selenium nanostructures- a comprehensive review

Tailoring the size and shape of nanostructures are detrimental in deciding the final properties of the nanomaterials. The shape of the material has a direct consequence on the facet orientation, surface structure and number of atoms on the edges. The size of the nano species on the other hand, determines the ratio of surface to bulk atoms[8]. Controlling the morphology of the nanomaterials can successively tune the device performance. Various strategies have been developed to fabricate different Se nanostructures including 0D (nanoparticles), 1D (nanowires, nanorods, nanotubes, nanobelts), 2D (nanosheets) and even other complex hierarchical structures. The review aims to understand the various nanostructures of Se that have been reported in literature with specific interest in the morphology and synthesis of these structures.

Out of the various crystalline forms of Se, cubic and monoclinic Se is relatively less explored. Shape controlled synthesis of cubic-like Se structures using folic acid-gallic acid-*N*,*N*,*N*-trimethyl chitosan (FA-GA-TMC) stabilizer have been found to have good anticancer properties[9]. Though there are reports

of synthesis of β-cubic Se from bacterial strain like *Pseudomonas aeruginosa* through biological reduction of certain Se precursors[10], inorganic synthesis of cubic Se and their structural understanding in literature is sparse. α-cubic to amorphous transition of Se quantum dots (QDs) in silica matrix were studied for application in optical limiters[11]. Pure m-Se on the other hand, is often not attainable commercially due to their poor thermostability[12]. The synthetic process for trigonal and monoclinic structures often results in symbiotic mixtures of trigonal and monoclinic allotropes. One of the earliest reports of synthesis of α-monoclinic nanowires is by the reduction of selenate ions using protein *cytochrome* c_3[13]. Free standing nanowires with monoclinic crystal structure were synthesized by Gao et.al via a room temperature mediated solution-solid growth method[14].

Amorphous Se nanostructures are widely synthesized via various chemical, physical and biological routes. In chemical synthesis, various reducing agents like hydrazine hydrate[15], ascorbic acid[16], L-cysteine[17], L-asparagine[18] etc are effectively used to reduce Se precursors to Se NPs. These NPs are also often stabilized using surfactants like PVP[15], PVA[19], sodium dodecyl sulphate[20], polysaccharides[21] etc in order to prevent their interconversion to more stable trigonal form. Physical methods employ laser ablation[22], gamma[23], microwave[24], ultraviolet irradiation[25] and sonochemical[26] methods to reduce Se(IV) compounds to Se NPs. Quintana et.al., reported one of the earliest synthetic routes to fabricate a-Se NPs using pulsed laser deposition using a YAG laser at 532 nm on different substrates[27].

Biogenic routes on the contrary, offer a non-toxic, eco-friendly and cheaper method to obtain a-Se NPs which are then studied for antibacterial, antifungal and anticancer properties. The biogenic reduction of Se precursor can be carried out using plant extracts[28], bacteria[29,30], fungi[31] etc. Recently, these biological and physical routes have been employed for effective segregation of Se by reduction of selenide/selenates or other Se containing compounds from natural resources with minimal intervention of harsh chemical reagents. A recent work done by MA Ruiz-Fresneda et.al., describes the biogenic reduction of selenium isotopes from radionuclide waste to synthesis of Se NPs using a bacterial isolate *Stenotrophomonas bentonitica* BII-R7[32].

The trigonal nanowires, similar to amorphous nanoparticles of Se are widely studied due to their ease of formation compared to other counterparts[33]. The ease of synthesis of t-Se structures can be understood from Li et.al's report on synthesis of high yield t-Se nanowires through simple reduction of SeO_2 at room temperature using ascorbic acid under the assistance of β-cyclodextrin, without the use of any complex equipment or adverse reaction conditions[34]. Trigonal Se with diverse and controlled morphologies also were successfully fabricated via hydrothermal approach from single precursors[35,36]. Sonochemical processes have also been extensively adopted to fabricate 1D trigonal Se as reported by Li et.al[37]. Single crystalline t-Se nano needles were also developed by Xiong et.al via a one-step in situ reduction of Na_2SeO_3 by poly(vinyl alcohol) (PVA) under hydrothermal conditions[38]. Lu et.al, demonstrated a mild hydrothermal route to synthesize 1D t-Se nanobelts using cellulose as a reducing as well as morphology directing

agent[39]. Reports of 1D t-Se nanostructures synthesized from amorphous Se nanoparticles that act as 'seeds' are also abundant in literature[40,41]. One of the early studies in this regard is that of Gates et al. which reports t-Se nanowires with diameters of 10-30 nm and lengths up to hundreds of microns through a solution phase approach from colloidal amorphous Se[42]. Mary et.al, had studied ultrafast optical non-linearity in stable amorphous nanoparticles and trigonal selenium nanowires in nanosecond excitation regimes[43]. Pulsed laser ablation (PLA) is another top-down approach widely used for the synthesis of Se NPs, as reported by S.C Singh[44] et.al and O.V. Overschelde et.al[45]. Chen et.al., used L-cysteine as both reducing agent and soft template in solution at room temperature to fabricate Se NPs under high intensity ultrasonication[17]. The size and morphology of the nanoparticles was found to be tunable by altering the reaction conditions and a transition from amorphous NPs to trigonal Se nanorods observed on prolonged high-intense ultrasonication.

Physical vapor deposition (PVD) and chemical vapor transport (CVT) are the reported techniques for high quality Se nanosheet fabrication[46,47]. An electrolyte-gated synaptic transistor (EGT) capable of mimicking the axon−multisynapse system of human brain, based on a trigonal Se nanosheet was recently demonstrated by Qin et.al.[48] Apart from chemical/inorganic synthesis, Se NPs are widely studied through various green, biogenic synthesis routes to achieve biocompatibility for many bio-medical applications. The biological agents that mediate the growth of these nanostructures vary from bacteria[32,49], fungi[50,51], algae[52] and even plan extracts[53–55].

Hexagonal 0D Se quantum dots of diameter ~3 nm and with QY=22.7%, that even outperforms graphene QDs were synthesized via ultrasound liquid-phase exfoliation using $NbSe_2$ powders as the source material and N-Methyl-2-pyrrolidone (NMP) as the dispersant[56]. Jiang et.al reported a similar liquid-phase exfoliation method to fabricate trigonal Se QDs and their photocarrier dynamics were systematically investigated[57]. Four different decay pathways with different decay lifetimes corresponding to the splitting of energy bands were identified in the material. Fujishima et.al developed a current doubling-induced two step photodeposition (CD-2PD) technique in which Se QDs (< 5nm) were photodeposited on TiO_2 surface from ethanol (or methanol) solution of H_2SeO_3 (Se/TiO_2)[58]. CdSe QDs (~2 nm) were also synthesized by irradiating this system containing metal ion solution (Cd^{2+} ions) with UV radiation.

The various nanostructures of Se find diverse applications. Trigonal selenium-based bifacial solar cells with a PCE of 5.2% and 2.7% from front-side and back-side illumination respectively was synthesized for tandem photovoltaics[59]. In a recent article by Yan and co-workers, Se was also suggested as a suitable candidate in indoor photovoltaics as the absorption spectrum of Se matches with the emission spectra of indoor light sources that spans from 400 to 700 nm[60]. Monoclinic Se NPs grown via biogenic reduction by bacteria *Bacillus subtilis* was found to transform into 1D trigonal structures after 24 hours at room temperature. Both these nano structures were studied for H_2O_2 biosensing applications and had good sensitivity towards the analyte with a limit of detection of 80 nM[61]. Kuo et.al., proposed a flexible x-

ray imager using 100-μm-thick amorphous selenium (a-Se) on a flexible thin film transistor (TFT) backplane[62]. Flat panel detectors for medical imaging makes use of avalanche multiplication which is observed in a-Se NPs[63]. An interconversion among these various phases of Se have also proved to be instrumental for various applications. Different (de)lithiation mechanisms was recently explored to improve the performance of Li-Se batteries by using amorphous and/or crystalline selenium[64].

The Se^0 species and the biogenic/physico-chemical methods involved plays a crucial role in the end structure of the allotrope. The biogenic synthesis of Se nanostructures involves the reduction of Se precursor using living organism and their derivatives (mostly plant and bacterial extracts) and often results in the formation of nano globules of Se[65,66]. However, scaling of the production and quality of these nanoparticles in terms of their homogeneity in shape, size and structure hinders their industrial or commercial potential. The chemical synthesis on the contrary involves the reduction of Se salt precursors (selenous acid, sodium selenite, sodium selenate, sodium selenosulphate etc) using suitable reducing agents like glucose, cysteine, ascorbic acid, glutathione etc[67,68]. Other methods of physical synthesis of Se^0 nanoparticles include laser irradiation[44], microwave irradiation[18], hydrothermal[69], sonochemical[70] methods etc. Though various synthesis methods can often result in the formation of different structures, formation of different allotropes of an element from single precursor and same base technique remains challenging and untested.

2.1.3. Cytotoxicity of selenium nanostructures

Selenium is a chalcogen element and an indispensable micronutrient in human body with various selenoprotein forms like selenocysteine and selenomethionine[71]. It plays a vital role in reproduction, thyroid hormone, DNA synthesis and even metabolism. As per the UK group of vitamins and minerals, recommended daily dosage for men and women are 60 µg and 70 µg respectively with anything above a daily intake of 400 µg termed toxic. Its deficiency can cause certain neurological disorder and even liver malfunctioning. On the contrary, inorganic selenium counterparts like selenates and selenides are often disparaged due to their toxic demeanour[72]. However, elemental Se nanoparticles (NPs) has shown excellent anticancer efficacies and decreased systemic toxicity[73,74]. They have also shown anti-oxidant, anti-biofilm, antibacterial properties and even proved to be effective as Hungtington's disease medication. Geoffrion et.al., recently put forth the effectiveness of pure naked amorphous Se (a-Se) NPs against standard and antibiotic-resistant bacterial strains. These NPs were seen to be compatible with human dermal fibroblasts (HDF) cells while inhibiting cell proliferation in cancerous cells[75]. Reports of Se NPs with excellent immunomodulatory[71,74] and immunoadjuvent[76] properties against breast cancers are also found in literature. Antioxidant and antibacterial activity of Se NPs incorporated into chitosan were also investigated[77]. Selenium tethered mesoporous silica nanocomposites were also successfully used as a dual drug delivery unit with significant apoptosis against breast cancer cells[78]. Clinical

trials using elemental nano Se have already proven to be a potential alternative than other selenium sources. It is noteworthy that QD toxicity is correlated to its physicochemical attributes like size, shape, core/shell composition, surface modification, nature of surface charge and solubilizing ligands[79]. Hence, different allotropic structure of the same material could pose varying degrees of toxicity towards a cell[80]. A notable work in this regard is that of carbon allotropes. Pulmonary exposure of single walled carbon nanotubes were reportedly more toxic than graphite and carbon black[81,82]. Nevertheless, similar reports of toxic and pharmacological effects of Se QDs are scarce in literature. The present work aims to identify and compare the cytotoxic activity of Se QDs (cubic, amorphous, monoclinic and trigonal) and provide a better understanding of correlation between structural modification and biotoxicity.

2.2. EXPERIMENTAL SECTION

2.2.1. Materials

Tetraethyl orthosilicate (TEOS) ($Si(OC_2H_5)_4$, 98%) and selenous acid (H_2SeO_3, 98%) were procured from Sigma-Aldrich. Distilled water was used throughout the experiment.

2.2.2. Apparatus and characterization

Morphological parameters were evaluated from High Resolution Transmission Electron Microscopy (HRTEM) data from a TALOS F200S G2 Transmission Electron Microscope (200KV, FEG, CMOS Camera 4k x 4k) and JEOL JEM 2100 High Resolution Transmission Electron Microscope. Raman

spectra obtained from Horiba Jobin Yvon T64000 Raman spectrometer was used for phase identification. The structural analysis was carried out using Fourier Transform Infa-Red (FTIR) spectrum in the region 400-4000 cm^{-1} obtained from FTIR spectrometer (Thermo Nicolet- USA) at room temperature. The absorption spectra in the entire visible range were recorded on a UV Vis spectrophotometer (Jasco, Japan).

2.2.3. Synthesis of Se- silica composites

10 wt% Se in 2g silica was prepared by simple sol-gel and sol gel assisted solvothermal routes using selenous acid as precursor. Cubic and amorphous forms of Se were synthesized through sol-gel synthesis involving hydrolysis, condensation and polymerization of tetraethyl orthosilicate (TEOS) in the presence of ethanol and distilled water[11]. On the other hand, the autogenous pressure generated within a solvothermal system was used to rapidly hydrolyse and condense the silica matrix to attain m-Se and t-Se QDs. In a typical synthesis, aqueous solution of selenous acid was added to TEOS and ethanol at room temperature. 2 drops of 1M HNO_3 was added as a catalyst. The resulting mixture was stirred continuously for 1 hour to obtain a clear solution. The molar ratio of TEOS: Water: Ethanol was taken as 1:2:2.

- *Synthesis of cubic (c-Se) and amorphous (a-Se) QDs - silica*

The homogeneous aqueous mixture of selenous acid, TEOS and ethanol was poured and allowed to set in polypropylene dishes for about a month. The silica xerogel obtained was then heated at 60 °C in hot air oven to remove the organics in the sample to obtain c-Se- silica which is colourless. The c-Se-silica

when annealed at 200 °C for 2 hours gives a brick-red coloured glass indicating the formation of a-Se in silica matrix.

- *Synthesis of monoclinic (m-Se) and trigonal (t-Se) QDs - silica*

The homogeneous aqueous mixture of selenous acid, TEOS and ethanol was poured into 50 mL teflon-lined autoclave and heated at 100 °C and 150 °C. After 24 hours at 100 °C, a wine-coloured composite of m-Se-silica was obtained. A grey coloured composite obtained after 24 hrs at 150 °C indicates the formation of t-Se. The obtained composites were powdered and used for further characterizations.

2.2.4. In-vitro cytotoxicity studies

The samples were studied for short-term cytotoxicity in rat spleen cells. This study was done at Amala Cancer Research Centre Society (A Society registered T.C.Act, XII of 1955sl.No. 56 of 1984), that abides by all rules of its licensing committee for performing the said analysis using experimental protocols that are approved by the licensing committee. Viable cell suspension (10^6 cells in 0.1 mL) obtained after preliminary treatment of rat spleen cells was added to tubes containing various concentrations of the composite dissolved in dimethyl sulfoxide and made upto 1 mL using DMEM media. Cell suspensions without any test composite were kept as control. The tubes were incubated for 3 hours at 37 °C after which they were mixed with 0.1 mL 1% trypan blue solution. These were kept for few minutes and then loaded into a hemocytometer. The trypan blue solution stains the dead cells while living cells

in the suspension do not absorb the color. The numbers of stained and unstained cells were noted and cell viability was evaluated as

$$\%Viability = \frac{No.of\ viable\ cells}{Total\ no.of\ cells} * 100 \quad (2.1)$$

In order to understand the effect of toxicity of Se QDs on the rat spleen cells, bare SiO_2 sample was also synthesized and studied for cytotoxicity in addition to the four different QDs of Se.

2.3. RESULTS AND DISCUSSION

2.3.1. Transmission Electron Microscopy (TEM) & High-Resolution Transmission Electron Microscopy (HR-TEM)

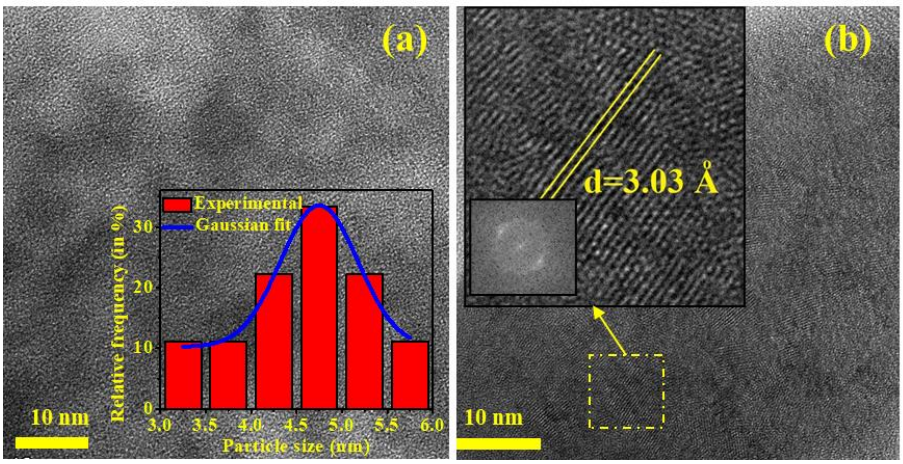

Figure 2.2-(a) TEM image of c-Se QDs with size distribution histogram in the inset; (b) HRTEM image showing (hkl) planes marked with interatomic distances of 3.03 Å (001) in the inset with the FFT of the scanned area in the inset of inset

Structural analysis of the allotropes of Se QDs was done from Transmission Electron Microscopy (TEM) and High-Resolution Transmission Electron Microscopy (HRTEM). TEM images show randomly oriented crystallites. The crystallite size distribution histogram given in the **inset of Figure 2.2(a)** depicts that c-Se QDs has an average size in the range 3-6 nm. Inter planar spacing of the lattice fringes observed in the HRTEM image was evaluated as 3.03 Å. This can be ascribed to the (001) plane of c-Se [11] (given in the **inset of Figure 2.2(b)**). The Fast Fourier Transform (FFT) analysis of the selected area is given in the **inset of inset of Figure 2.2(b)**. The bright spots obtained in the FFT pattern correspond to the diffraction pattern in cubic crystal lattice.

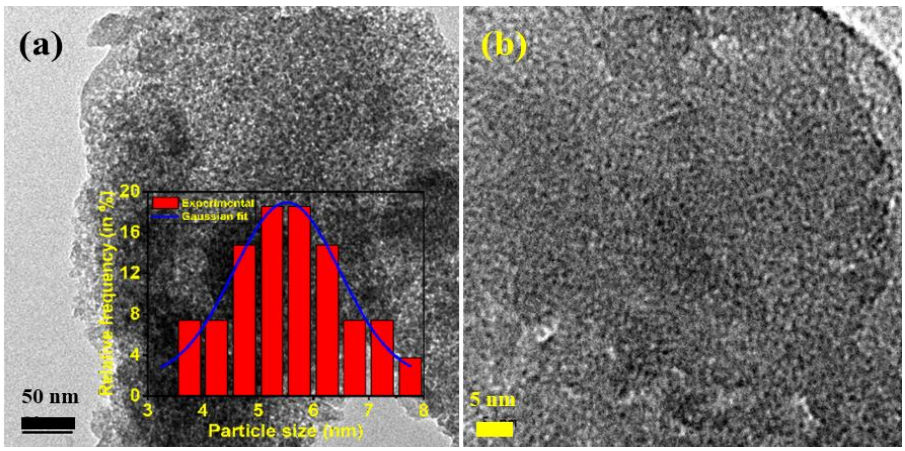

Figure 2.3-(a) TEM image; inset showing particle size distribution (b) HRTEM image of a-Se- silica composite

Figure 2.3(a) shows the TEM image of a-Se-silica composite. Large field TEM imaging shows the presence of some agglomerated quasi-spherical

entities. The particle size distribution given in the **inset of Figure 2.3(a)** suggests that the particle size varies from 3 to 7 nm. Regular orderly arrangement or lattice fringes were not observed in the HRTEM images (**Figure 2.3(b)**). This confirms the amorphous nature of the sample.

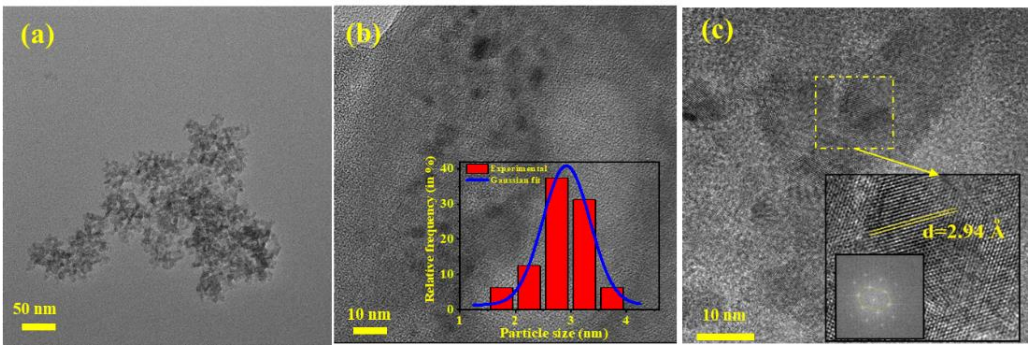

Figure 2.4-(a) TEM and (b) HRTEM image of t-Se QDs in silica matrix with size distribution histogram in the inset of (b); (c) HRTEM images showing t-Se QDs, with the (hkl) plane marked with interatomic distances of 2.94 Å (101) in the inset; the FFT of the scanned area is also given in the inset of the inset.

The TEM image given in **Figure 2.4(a)** illustrates the morphology of the material. The composite exhibited an approximate width of about 120 nm. **Figure 2.4(b)** shows the corresponding HRTEM images of t-Se-silica composite. The **inset of Figure 2.4(b)** shows the size distribution of the dots in silica. Crystallites were found to be in the size range of 2-4 nm. HRTEM images also reveal randomly aligned regions of crystallinity. From the **inset of Figure 2.4(c)**, lattice fringes with inter planar spacing of 2.94 Å were observed. It can be attributed to the (101) plane of the trigonal structure of Se (ICDD-006-0362). FFT image generated from the selected area in the HRTEM image (**inset of**

inset of Figure 2.4(c)) verifies that Se QDs crystallised in a hexagonal structure and it showed excellent agreement with the calculated diffracted pattern of t-Se. On close examination, the randomly oriented crystals were also noted to have abrupt edges and even faults in the packing. The detailed study of the crystal structure, lattice defects and imperfections found in the trigonal Se QDs and its effect on the morphology and other properties is discussed in detailed in the upcoming chapter.

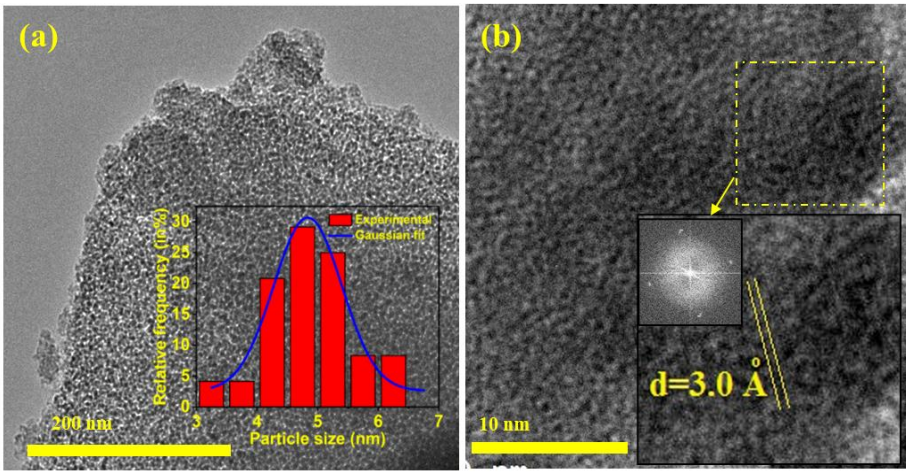

Figure 2.5-(a) TEM image; (b) HRTEM images showing m-Se QDs, lattice fringes that corresponds to the inter planar spacing of 3.0 Å corresponding to (2$\bar{2}$3) plane is shown in inset; FFT of the scanned area is also given in the inset of inset

Figure 2.5(a) and **2.5(b)** depicts the far field TEM and HRTEM images of m-Se-silica composite. The spherical morphology of the particle is evident from the TEM image. Lattice fringes were observed in the HRTEM image of the composite and on close evaluation of the selected area, the inter planar spacing

of these fringes were found to be approximately 3.0 Å (**inset of Figure 2.5(b)**). This corresponds to the intense $(22\bar{3})$ plane of m-Se. The Fast Fourier Transform of the aforesaid selected area is given in the **inset of inset of Figure 2.5(b)** and can be ascribed to the presence of m-Se.

2.3.2. Selected Area Electron Diffraction (SAED)

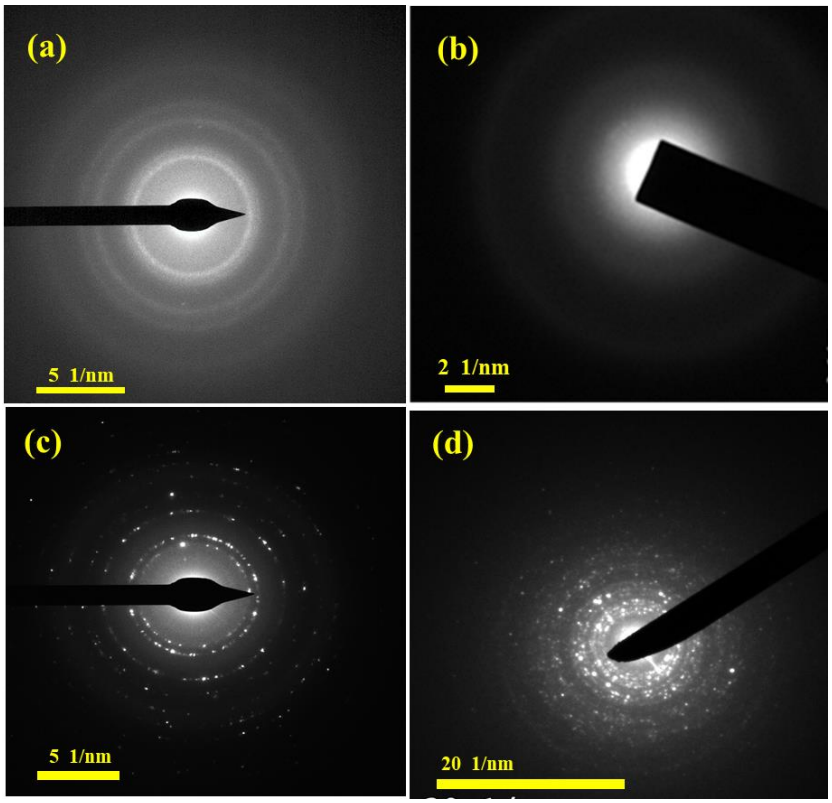

Figure 2.6- SAED pattern showing (a) (hkl) planes that is indexed to c-Se (b) amorphous nature of the a-Se (c) diffraction pattern indicating trigonal structure (d) diffraction rings indexing to m-Se QDs in silica matrix.

The polycrystalline nature of the composite is evident from SAED pattern given in **Figure 2.6(a)**. It shows concentric diffraction rings corresponding to (001), (011), (111) and (012) planes of cubic Se (ICDD-038-0768). Presence of a halo like appearance in the electron diffraction pattern observed in **Figure 2.6(b)** is characteristic of amorphous structure of a-Se QDs. Concentric rings corresponding to trigonal phase of Se was clearly observed in the SAED pattern in **Figure 2.6(c)**. The electron diffraction pattern given in **Figure 2.6(d)** shows many concentric rings indicating the polycrystalline nature of the composite and these closely spaced rings can be indexed to the monoclinic planes of Se (JCPDS 71-0528)..

2.3.3. Raman spectroscopy

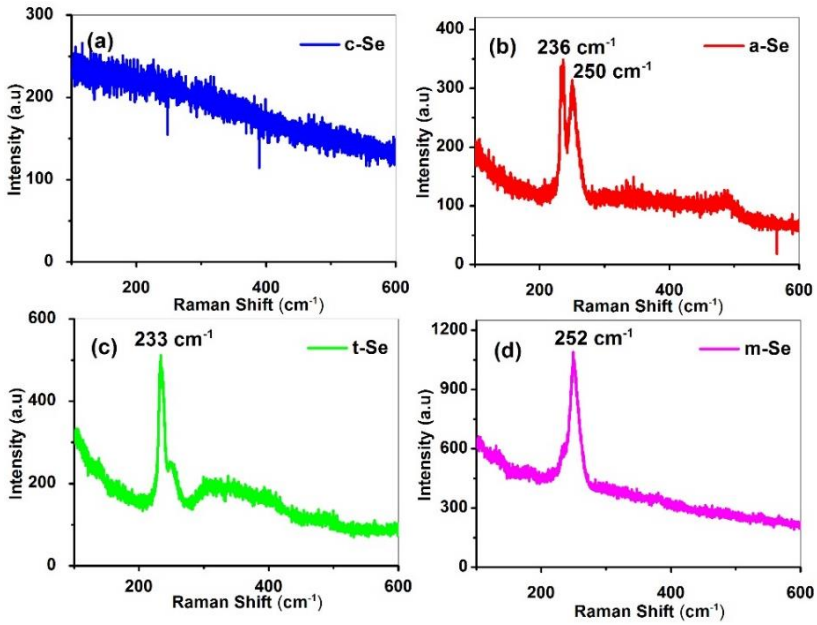

Figure 2.7-RAMAN spectra of (a) c-Se (b) a-Se (c) t-Se and (d) m-Se-silica composites

The structural identification of Se-silica was done using Raman spectroscopy. Raman spectroscopy was found to be sensitive to various allotropic modifications and crystallinity of elemental Se[83]. The spectra of interest for various forms of selenium are in the low-frequency region, particularly under 500 cm^{-1}. The Raman spectra given in **Figure 2.7** shows the absorption bands observed for various composites under study. Though the characteristic peak of Se is reported to be at approximately 250 cm^{-1} (which corresponds to the A_1 symmetric vibrations of rings or chains in the crystal), shifts are observed in the resonance peak position based on the polymorph of Se formed[84]. The absence of any spectral peak in **Figure 2.7(a)** is due to the formation of cubic Se structure in the matrix. For simple cubic structure, there are no Raman active modes and hence first order Raman spectrum is not allowed due to symmetry considerations[85]. The amorphous phase of Se can be easily identified from the spectra given in **Figure 2.7(b)**. The spectrum is a broadened bi headed peak with one head peaked at 250 cm^{-1} due to the disordered Se chains with minor contribution from Se rings, Another peak head at 236 cm^{-1} corresponding to symmetric bond stretching mode A_1 in t-Se is due to the photocrystallisation from a-Se to t-Se upon laser irradiation[86]. Presence of both these peaks in the spectrum could be indicative of the fact that the short monomer orders of a-Se contains fragments is characterised by both ring-like and chain-like confirmation[87]. Similarly, the characteristic resonance band observed at 233 cm^{-1} (as depicted in **Figure 2.7(c)**) can be attributed to the presence of helical selenium chains (A_1) as observed for trigonal structure of elemental selenium[88]. The single resonance peak at 252 cm^{-1} observed in

Figure 2.7(d) confirms the monoclinic ring crystallisation of selenium in silica matrix[24].

2.3.4. Fourier Transform Infrared (FTIR) spectra

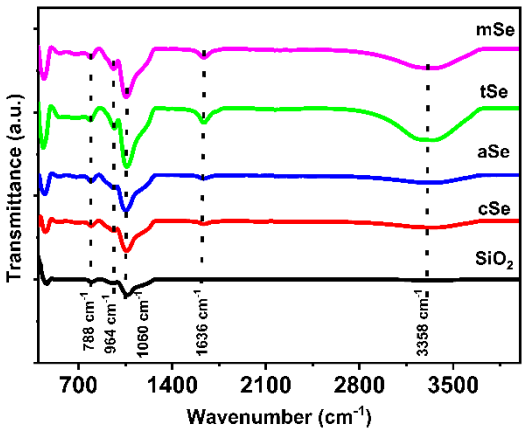

Figure 2.8-FTIR spectra of selenium-silica composites

The chemical structure of the as prepared composites was studied using Fourier-Transform Infrared (FTIR) spectra as shown in **Figure 2.8**. It was evident that all the spectra resemble the peak positions observed for SiO_2 based composites reported in literature[89]. This can be attributed to the fact that Se species would have been encapped in the silica matrix during synthesis. The characteristic symmetric stretching and bending vibrations associated with Si-O bonds were observed around at 788 cm^{-1} and 1060 cm^{-1} respectively. The bands at 1636 cm^{-1} and 964 cm^{-1} is attributed to the oxo-ethyl group in the composites. The broad absorption at 3358 cm^{-1} can be indexed to the presence of hydroxyl (-OH) group in the composite[90,91]. The absorption bands corresponding to

these hydroxyl groups are more prominent for sol gel assisted solvothermal samples of trigonal and monoclinic Se which were also very brittle in nature. This could be due to the fact that the moisture and other organics could have seeped less from the matrix during their rapid synthesis. On the contrary, the cubic and amorphous samples were formed to stiff gels after long-term drying and ageing.

2.3.5. UV-Visible absorption spectra & Tauc plot

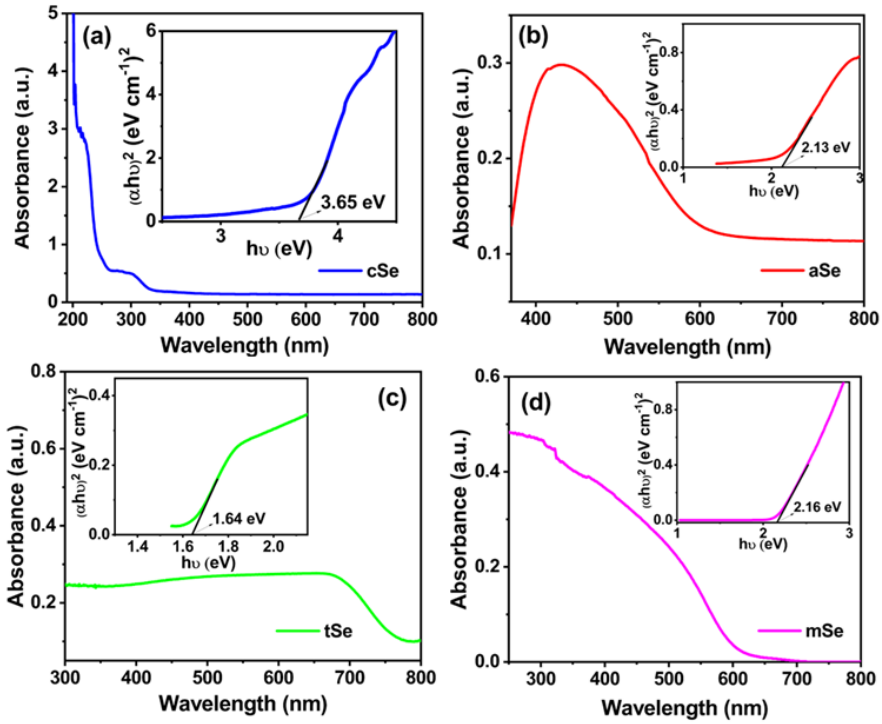

Figure 2.9- Absorption spectra of (a)c-Se, (b)a-Se, (c)t-Se and (d)m-Se doped silica composites. The Tauc plots given in the respective inset gives the optical band gap of the material.

The UV-visible absorption spectra of the all the four QDs and the band gap evaluated from the Tauc plot correspondingly is shown in **Figure 2.9(a-d)**. The direct absorption bandgap of these semiconductor materials was calculated using the equation

$$(\alpha h\nu)^2 = B(h\nu - Eg) \tag{2.2}$$

where α is the absorption coefficient, $h\nu$ is the photon energy, E_g is the absorption band gap, and B is a constant corresponding to the material.

$$\text{Here, } \alpha = \frac{2.303\ A}{d} \tag{2.3}$$

where A is the absorbance and d is the thickness of the sample.

The band gap was estimated by extrapolating the slope of $(\alpha h\nu)^2$ vs $h\nu$ graph to intersect the x-axis so that $\alpha=0$. Cubic Se quantum dots exhibited an absorption band peaked around 310 nm. The observed optical bandgap of the material was evaluated to be 3.65 eV (**inset of Figure 2.9(a)**). This is in accordance with the gap value of cubic-Se from prior studies. The observed band gap for cubic Se can hence be attributed to the exciton absorption in the material[11]. The absorption spectra for a-Se show a broad absorption band peaked at 450 nm. The calculated band gap of a-Se quantum dots was 2.13 eV (**inset of Figure 2.9(b)**) and found to be consistent with reported values in the literature[11,92]. The trigonal quantum dots obtained via solvothermal assisted sol-gel route exhibited an absorption edge at 750 nm and a broad absorption in the lower wavelength region. The first excitonic peak for trigonal Se

nanomaterials is reported at approximately 2 eV[57]. However, the band gap obtained for the as synthesized dots was 1.65eV (**inset of Figure 2.9(c)**). Though a blue shift is often expected owing to the quantum confinement in dots, a decrease in the band gap is noted. This could also be due to the presence of surface states and trap sites in the material[93,94]. The microstructural studies conducted for t-Se and its effect on the optical properties of the dot has been discussed in detail in the following chapter. The monoclinic allotrope of Se evidently exhibits a broad absorption spectrum similar to a-Se. The bandgap of m-Se was evaluated from the Tauc plot (**inset of Figure 2.9(d)**) to be 2.16 eV and is found to be slightly higher than the previous reports of 2.05 eV[95]. This could be attributed to the quantum confinement of Se QDs.

2.3.6. Fluorescence spectra

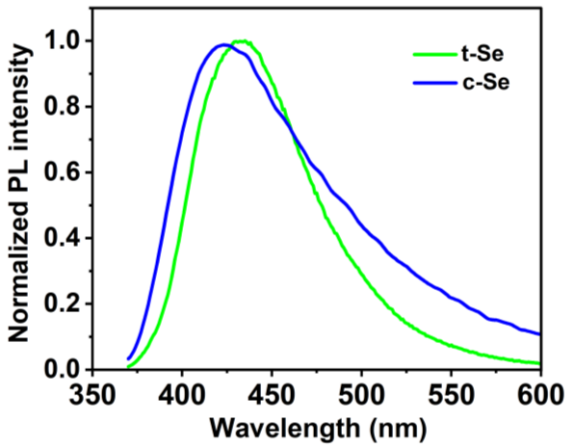

Figure-2.10.- Fluorescence spectra of cubic and trigonal Se-silica composites

The fluorescence spectra of Se-SiO_2 composites were recorded. Upon UV excitation at 350 nm, both cubic and trigonal forms of Se exhibit characteristic blue fluorescence with peaks at 425 nm and 434 nm respectively (**Figure 2.10**). The emission band observed for c-Se corresponds to band-edge emission in the material[11]. The emission peak obtained for t-Se can be attributed to direct inter-band radiative recombination of these QDs[96]. A detailed understanding of the fluorescence emission of t-Se is made in chapter-3. Amorphous and monoclinic Se do not show any fluorescence emission which is consistent with earlier reports[11,92].

2.3.7. Thermogravimetric Analysis (TGA)

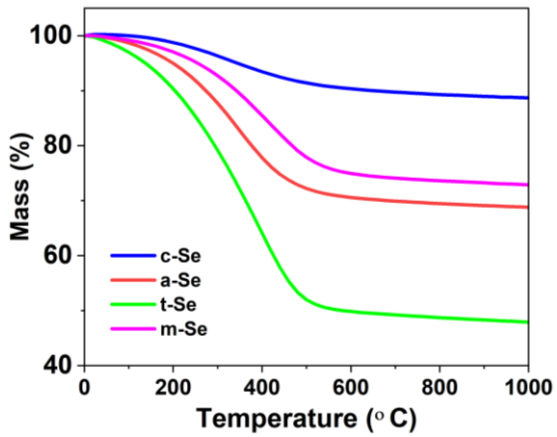

Figure-2.11.- Thermogravimetric analysis spectra of Se-silica composites

The thermal stability of all the different Se-silica composites were evaluated from TGA spectra (**Figure 2.11**). The spectra of all the Se-silica composites can be divided into three regions. The small weight loss below 200

℃ can be attributed to the removal of moisture and other physically adsorbed organics from the matrices. The second stage of weight loss from 200 ℃ to 400 ℃ observed in the samples is due to the dihydroxylation and decomposition of organic groups from the silica network. A part of this weight loss could also be ascribed to the volatization of Se from the matrices as Se has a reported melting point around 220 ℃. The mass loss in this stage varies for each sample as the host silica matrices does not have the same density and porosity owing to the different synthesis temperature and route. A stable plateau region is attained after dehydroxylation where sample suffers negligible weight loss and the material remains as such till 1000 ℃. Among Se-silica composites, c-Se exhibits better stability with minimal weight loss. This is due to the slow ageing and drying of the gel over a period of one month. This strengthens the silica network to form silica glasses with higher degree of stiffening of the gel during condensation which retains almost 88% weight even at 1000 ℃.

2.3.8. Mechanism of formation of Se QDs in silica

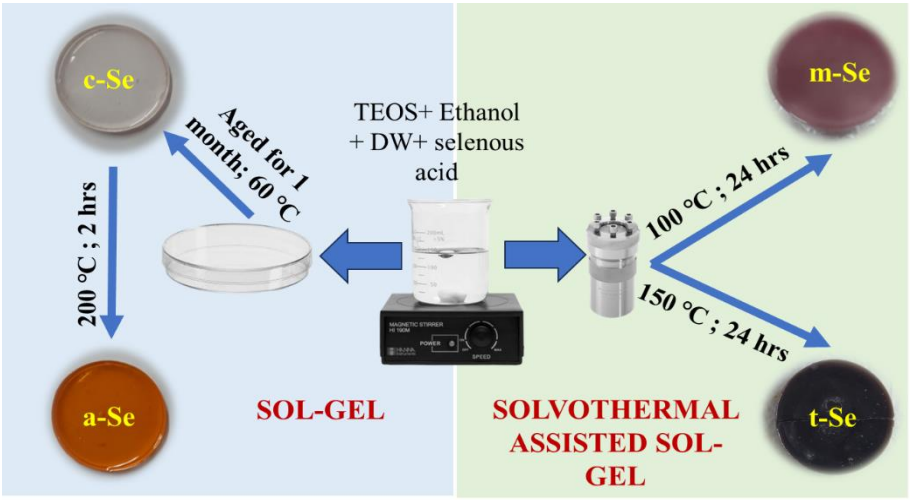

Scheme 2.1. Schematic diagram showing the synthesis of different Se QDs in silica by sol gel and sol-gel assisted solvothermal route.

The four selenium allotropes were synthesized from a single precursor by simply altering the synthesis conditions. A schematic representation of the synthesis procedure adopted is given in **Scheme 2.1**. During the sol-gel synthesis of Se-SiO_2 mixture, selenous acid decomposes and elemental selenium nucleates at favorable sites of tetraethyl orthosilicate (TEOS). Trigonal form of selenium is thermodynamically most stable form and Se always tends to grow in a preferred direction along c-axis in the mixture. In a mesoporous matrix like silica, the capping effect of the xerogel inhibits the growth of nanomaterials. Upon ageing to 1 month, the material crystallizes in a more symmetric cubic structure in the voids of silica. Upon annealing at 200 °C, which is near to the melting temperature of bulk Se, the element melts and agglomerates into

amorphous structure. This unusual cubic to amorphous transformation mechanism had been described previously[11].

Under solvothermal conditions, the decomposition of selenous acid is followed by nucleation of trigonal selenium nanocrystallites at favourable sites of TEOS. The strong surface adsorption of TEOS promotes the initial growth of nanocrystals through pure oriented attachment (OA) mechanism. This slow down the dissolution of particles in solution and nucleation-dissolution recrystallization mechanism is thermodynamically prohibited. The solvothermal treatment of mixture triggers rapid hydrolysis of TEOS in the presence of water and ethanol. This is simultaneously followed by a cascade of quick polycondensation reactions during which growth of trigonal Se QDs is promoted at preferred sites. Though crystallization of anisotropic trigonal Se is promoted by OA assisted mechanism, the SiO_2 network inhibits their further habitual growth to 1D nanostructures. The capping effect of SiO_2 network acts as a growth controlling agent and the product retains a quasi-spherical shape with abrupt edges.

The growth of monoclinic and trigonal Se can be differentiated by the fact that at higher temperatures (at any temperature greater than about 130 °C), monoclinic selenium transforms into trigonal structure due to its poor thermal stability. The formation of different allotropic forms of Se in silica matrix is visually perceptible with color of the final composite. While c-Se is colorless, upon annealing it converts into brick red a-Se. The trigonal form of Se is characterized by a grey color while m-Se attains a wine-red color after solvothermal treatment.

2.3.9. Cytotoxicity analysis of Se QDs

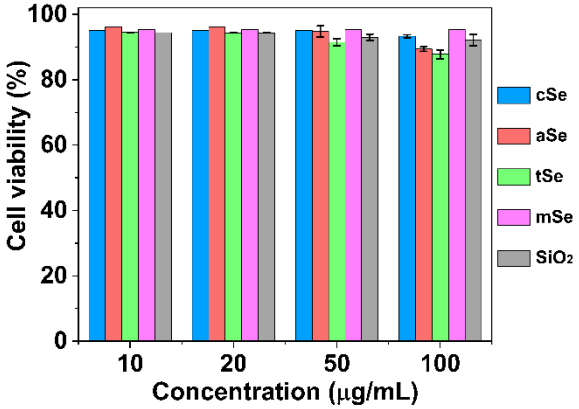

Figure-2.12.- In-vitro cytotoxicity of Se-SiO_2 composites in rat spleen cells

Selenium containing species are often criticised for their toxic demeanour. Most of these accusations disregard the fact that elemental Se or Se NPs have exhibited better biocompatibility than Se containing compounds[68,97]. The cytotoxic activity of the as synthesised selenium polymorphs in silica were hence evaluated by short term in vitro cytotoxicity in rat spleen cells. Cell viability was evaluated for allotrope dispersion and compared with the activity shown by the reference silica sample. All samples showed excellent cell viability against spleen cells. As per the cell cytotoxicity assay shown in **Figure 2.12**, c-Se, a-Se and t-Se showed gradual decrease in cell viability upto approximately 93%, 89% and 87% respectively at a concentration of 100 µg/mL. However, m-Se retained a constant viability of ~95% for the examined concentrations. This value is exceptionally good in comparison with

the toxicity of bulk Se reported in literature. These results reiterate the fact that elemental Se is biologically inert and pose least threat upon use.

2.4. CONCLUSION

Various allotropes of Se were synthesized in silica matrix via sol gel and sol-gel assisted solvothermal decomposition of selenous acid. Cubic selenium was synthesized at room temperature after ageing the sol-gel mixture to a stiff gel. Annealing the cubic Se-SiO_2 at 200 °C transformed the QDs to amorphous brick-red Se. Additionally, solvothermal treatment of the sol-gel mixture at 100 °C resulted in monoclinic crystal structure of Se whereas the solvothermal temperature of 150 °C was found necessary for the synthesis of t-Se QDs. The allotropes were characterized using Raman spectra by identifying the characteristic resonance peak indigenous to the polymorph. The various lattice spacings and diffraction rings obtained in HRTEM and SAED patterns was instrumental in differentiating the crystal structure of the allotropes while FTIR spectra was analysed to study surface groups and chemical bonds. Additionally, all four allotropes exhibited distinct UV-visible absorption characteristics. Cytotoxic activity of these QDs was studied in rat spleen cells. All the allotrope suspensions showed comparable cell viability and was found to be a highly biocompatible alternative to selenite and selenide compounds.

2.5. REFERENCES

[1] Hirsch A. The era of carbon allotropes. Nat Mater 2010;9:868–71. https://doi.org/10.1038/nmat2885.

[2] Todorov TK, Singh S, Bishop DM, Gunawan O, Lee YS, Gershon TS, et al. Ultrathin high band gap solar cells with improved efficiencies from the world's oldest photovoltaic material. Nat Commun 2017;8:682. https://doi.org/10.1038/s41467-017-00582-9.

[3] Huang H, Abbaszadeh S. Recent Developments of Amorphous Selenium-Based X-Ray Detectors: A Review. IEEE Sens J 2020;20:1694–704. https://doi.org/10.1109/JSEN.2019.2950319.

[4] Nayak V, Singh KR, Singh AK, Singh RP. Potentialities of selenium nanoparticles in biomedical science. New J Chem 2021;45:2849–78. https://doi.org/10.1039/D0NJ05884J.

[5] Dang C, Liu M, Lin Z, Yan W. Selenium nanomaterials enabled flexible and wearable electronics. Chem Synth 2023;3:14. https://doi.org/10.20517/cs.2022.33.

[6] Farfán W, Mosquera E, Vadapoo R, Krishnan S, Marín C. Vapor-Liquid-Solid Synthesis and Characterization of α -Monoclinic Selenium Nanowires. J Nanosci Nanotechnol 2009;9:4846–50. https://doi.org/10.1166/jnn.2009.1082.

[7] Ding Y, Li Q, Jia Y, Chen L, Xing J, Qian Y. Growth of single crystal selenium with different morphologies via a solvothermal method. J Cryst Growth 2002;241:489–97. https://doi.org/10.1016/S0022-0248(02)01323-4.

[8] He Z, Yang Y, Liu J-W, Yu S-H. Emerging tellurium nanostructures: Controllable synthesis and their applications. Chem Soc Rev 2017;46. https://doi.org/10.1039/C7CS00013H.

[9] Luesakul U, Komenek S, Puthong S, Muangsin N. Shape-controlled synthesis of cubic-like selenium nanoparticles via the self-assembly method. Carbohydr Polym 2016;153:435–44. https://doi.org/10.1016/j.carbpol.2016.08.004.

[10] Dwivedi S, AlKhedhairy AA, Ahamed M, Musarrat J. Biomimetic Synthesis of Selenium Nanospheres by Bacterial Strain JS-11 and Its Role as a Biosensor for Nanotoxicity Assessment: A Novel Se-Bioassay. PLOS ONE 2013;8:e57404. https://doi.org/10.1371/journal.pone.0057404.

[11] Mary KAA, Unnikrishnan NV, Philip R. Cubic to amorphous transformation of Se in silica with improved ultrafast optical nonlinearity. RSC Adv 2015;5:14034–41. https://doi.org/10.1039/C4RA14025G.

[12] Duan S, Chen S, Wang T, Li S, Liu J, Liang J, et al. Elemental selenium enables enhanced water oxidation electrocatalysis of NiFe layered double hydroxides. Nanoscale 2019;11:17376–83. https://doi.org/10.1039/C9NR06169J.

[13] Abdelouas A, Gong WL, Lutze W, Shelnutt JA, Franco R, Moura I. Using Cytochrome c_3 To Make Selenium Nanowires. Chem Mater 2000;12:1510–2. https://doi.org/10.1021/cm990763p.

[14] Gao X, Gao T, Zhang L. Solution–solid growth of α-monoclinic selenium nanowires at room temperature. J Mater Chem 2003;13:6–8. https://doi.org/10.1039/B209399E.

[15] Song J-M, Zhu J-H, Yu S-H. Crystallization and Shape Evolution of Single Crystalline Selenium Nanorods at Liquid−Liquid Interface: From Monodisperse Amorphous Se Nanospheres toward Se Nanorods. J Phys Chem B 2006;110:23790–5. https://doi.org/10.1021/jp065600k.
[16] Štefanková D, Skrbek K, Pižl M, Bartůněk V. Nano and mesosized selenium and its synthesis using the ascorbic acid route. J Non-Cryst Solids 2023;616:122462. https://doi.org/10.1016/j.jnoncrysol.2023.122462.
[17] Chen Z, Shen Y, Xie A, Zhu J, Wu Z, Huang F. l-Cysteine-Assisted Controlled Synthesis of Selenium Nanospheres and Nanorods. Cryst Growth Des 2009;9:1327–33. https://doi.org/10.1021/cg800398b.
[18] Yu B, You P, song meifang, Zhou Y, Yu F, Zheng W-J. A facile and fast synthetic approach to create selenium nanoparticles with diverse shape and their antioxidation property. New J Chem 2015;40. https://doi.org/10.1039/C5NJ02519B.
[19] Shah CP, Kumar M, Bajaj PN. Acid-induced synthesis of polyvinyl alcohol-stabilized selenium nanoparticles. Nanotechnology 2007;18:385607. https://doi.org/10.1088/0957-4484/18/38/385607.
[20] Bartůněk V, Junková J, Babuněk M, Ulbrich P, Kuchař M, Sofer Z. Synthesis of spherical amorphous selenium nano and microparticles with tunable sizes. Micro Nano Lett 2016;11:91–3. https://doi.org/10.1049/mnl.2015.0353.
[21] Zhang S-Y, Zhang J, Wang H-Y, Chen H-Y. Synthesis of selenium nanoparticles in the presence of polysaccharides. Mater Lett 2004;58:2590–4. https://doi.org/10.1016/j.matlet.2004.03.031.
[22] Haro-Poniatowski E, Escobar-Alarcón L, Hernández-Pozos JL, Mendoza-Luna LG, Guarin CA. Synthesis and characterization of selenium nanoparticles obtained by femtosecond pulsed laser ablation in liquid media. Appl Phys A 2022;128:827. https://doi.org/10.1007/s00339-022-05956-5.
[23] Pereira AG, Gerolis LGL, Gonçalves LS, Moreira LMC, Gastelois PL, Neves MJ. Radiolytic synthesis and characterization of selenium nanoparticles: comparative biosafety evaluation with selenite and ionizing radiation. World J Microbiol Biotechnol 2022;38:33. https://doi.org/10.1007/s11274-021-03218-9.
[24] Jadhav AA, Khanna PK. Impact of microwave irradiation on cyclo-octeno-1,2,3-selenadiazole: formation of selenium nanoparticles and their polymorphs. RSC Adv 2015;5:44756–63. https://doi.org/10.1039/C5RA05701A.
[25] Nu Hoai Nguyen V, Amal R, Beydoun D. Photocatalytic reduction of selenium ions using different TiO2 photocatalysts. Chem Eng Sci 2005;60:5759–69. https://doi.org/10.1016/j.ces.2005.04.085.
[26] Panahi-Kalamuei M, Mousavi-Kamazani M, Salavati-Niasari M, Hosseinpour-Mashkani SM. A simple sonochemical approach for synthesis of selenium nanostructures and investigation of its light harvesting application. Ultrason Sonochem 2015;23:246–56. https://doi.org/10.1016/j.ultsonch.2014.09.006.

[27] Quintana M, Haro-Poniatowski E, Morales J, Batina N. Synthesis of selenium nanoparticles by pulsed laser ablation. Appl Surf Sci 2002;195:175–86. https://doi.org/10.1016/S0169-4332(02)00549-4.
[28] Alagesan V, Venugopal S. Green Synthesis of Selenium Nanoparticle Using Leaves Extract of Withania somnifera and Its Biological Applications and Photocatalytic Activities. BioNanoScience 2019;9:105–16. https://doi.org/10.1007/s12668-018-0566-8.
[29] Tugarova AV, Mamchenkova PV, Khanadeev VA, Kamnev AA. Selenite reduction by the rhizobacterium Azospirillum brasilense, synthesis of extracellular selenium nanoparticles and their characterisation. New Biotechnol 2020;58:17–24. https://doi.org/10.1016/j.nbt.2020.02.003.
[30] Zhu Y, Kong X, Wu E, Zhu N, Liang D, Lou M, et al. [Biosynthesis of spherical selenium nanoparticles with halophilic Bacillus subtilis subspecies stercoris strain XP for inhibition of strawberry pathogens]. Sheng Wu Gong Cheng Xue Bao Chin J Biotechnol 2021;37:2825–35. https://doi.org/10.13345/j.cjb.200581.
[31] Faramarzi S, Anzabi Y, Jafarizadeh-Malmiri H. Nanobiotechnology approach in intracellular selenium nanoparticle synthesis using Saccharomyces cerevisiae—fabrication and characterization. Arch Microbiol 2020;202:1203–9. https://doi.org/10.1007/s00203-020-01831-0.
[32] Fresneda MAR, Martín JD, Bolívar JG, Cantos MVF, Bosch-Estévez G, Moreno MFM, et al. Green synthesis and biotransformation of amorphous Se nanospheres to trigonal 1D Se nanostructures: impact on Se mobility within the concept of radioactive waste disposal. Environ Sci Nano 2018;5:2103–16. https://doi.org/10.1039/C8EN00221E.
[33] Chaudhary S, Umar A, Mehta SK. Selenium nanomaterials: An overview of recent developments in synthesis, properties and potential applications. Prog Mater Sci 2016;83:270–329. https://doi.org/10.1016/j.pmatsci.2016.07.001.
[34] Li Q, Yam VW-W. High-yield synthesis of selenium nanowires in water at room temperature. Chem Commun 2006:1006–8. https://doi.org/10.1039/B515025F.
[35] Fan H, Wang Z, Liu X, Zheng W, Guo F, Qian Y. Controlled synthesis of trigonal selenium crystals with different morphologies. Solid State Commun 2005;135:319–22. https://doi.org/10.1016/j.ssc.2005.05.002.
[36] Mondal K, Srivastava SK. A new hydrothermal route to nano- and microstructures of trigonal selenium exhibiting diverse morphologies. Mater Chem Phys 2010;124:535–40. https://doi.org/10.1016/j.matchemphys.2010.07.006.
[37] Li X, Li Y, Li S, Zhou W, Chu H, Chen W, et al. Single Crystalline Trigonal Selenium Nanotubes and Nanowires Synthesized by Sonochemical Process. Cryst Growth Des 2005;5:911–6. https://doi.org/10.1021/cg049681q.
[38] Xiong S, Xi B, Wang W, Wang C, Fei L, Zhou H, et al. The Fabrication and Characterization of Single-Crystalline Selenium Nanoneedles. Cryst Growth Des 2006;6:1711–6. https://doi.org/10.1021/cg060005t.
[39] Lu Q, Gao F, Komarneni S. Cellulose-Directed Growth of Selenium Nanobelts in Solution. Chem Mater 2006;18:159–63. https://doi.org/10.1021/cm051082z.

[40] Sinha AK, Sasmal AK, Mehetor SK, Pradhan M, Pal T. Evolution of amorphous selenium nanoballs in silicone oil and their solvent induced morphological transformation. Chem Commun 2014;50:15733–6. https://doi.org/10.1039/C4CC08168D.
[41] Zhang J, Fu Q, Xue Y, Cui Z. Controlled synthesis of t-Se nanomaterials with various morphologies via a precursor conversion method. CrystEngComm 2018;20:1220–31. https://doi.org/10.1039/C7CE01998J.
[42] Gates B, Yin Y, Xia Y. A Solution-Phase Approach to the Synthesis of Uniform Nanowires of Crystalline Selenium with Lateral Dimensions in the Range of 10−30 nm. J Am Chem Soc 2000;122:12582–3. https://doi.org/10.1021/ja002608d.
[43] Ann Mary KA, Unnikrishnan NV, Philip R. Ultrafast optical nonlinearity in nanostructured selenium allotropes. Chem Phys Lett 2013;588:136–40. https://doi.org/10.1016/j.cplett.2013.09.069.
[44] Singh SC, Mishra SK, Srivastava RK, Gopal R. Optical Properties of Selenium Quantum Dots Produced with Laser Irradiation of Water Suspended Se Nanoparticles. J Phys Chem C 2010;114:17374–84. https://doi.org/10.1021/jp105037w.
[45] Van Overschelde O, Guisbiers G, Snyders R. Green synthesis of selenium nanoparticles by excimer pulsed laser ablation in water. APL Mater 2013;1:042114. https://doi.org/10.1063/1.4824148.
[46] Qin J-K, Qiu G, Jian J, Zhou H, Yang L-M, Zemlyanov D, et al. Controlled Growth of Large-Size 2D Selenium Nanosheet and Its Electronic and Optoelectronic Applications n.d.
[47] Sarma PV, Nadarajan R, Kumar R, Patinharayil RM, Biju N, Narayanan S, et al. Growth of highly crystalline ultrathin two-dimensional selenene. 2D Mater 2022;9:045004. https://doi.org/10.1088/2053-1583/ac787f.
[48] Qin J-K, Zhou F, Wang J, Chen J, Wang C, Guo X, et al. Anisotropic Signal Processing with Trigonal Selenium Nanosheet Synaptic Transistors. ACS Nano 2020;14:10018–26. https://doi.org/10.1021/acsnano.0c03124.
[49] Dwivedi S, AlKhedhairy AA, Ahamed M, Musarrat J. Biomimetic Synthesis of Selenium Nanospheres by Bacterial Strain JS-11 and Its Role as a Biosensor for Nanotoxicity Assessment: A Novel Se-Bioassay. PLOS ONE 2013;8:e57404. https://doi.org/10.1371/journal.pone.0057404.
[50] Zhang H, Zhou H, Bai J, Li Y, Yang J, Ma Q, et al. Biosynthesis of selenium nanoparticles mediated by fungus *Mariannaea* sp. HJ and their characterization. Colloids Surf Physicochem Eng Asp 2019;571:9–16. https://doi.org/10.1016/j.colsurfa.2019.02.070.
[51] Joshi SM, De Britto S, Jogaiah S, Ito S. Mycogenic Selenium Nanoparticles as Potential New Generation Broad Spectrum Antifungal Molecules. Biomolecules 2019;9:419. https://doi.org/10.3390/biom9090419.
[52] Vikneshan M, Saravanakumar R, Mangaiyarkarasi R, Rajeshkumar S, Samuel SR, Suganya M, et al. Algal biomass as a source for novel oral nano-antimicrobial agent. Saudi J Biol Sci 2020;27:3753–8. https://doi.org/10.1016/j.sjbs.2020.08.022.

[53] Alvi GB, Iqbal MS, Ghaith MMS, Haseeb A, Ahmed B, Qadir MI. Biogenic selenium nanoparticles (SeNPs) from citrus fruit have anti-bacterial activities. Sci Rep 2021;11:4811. https://doi.org/10.1038/s41598-021-84099-8.

[54] Hashem AH, Salem SS. Green and ecofriendly biosynthesis of selenium nanoparticles using Urtica dioica (stinging nettle) leaf extract: Antimicrobial and anticancer activity. Biotechnol J 2022;17:2100432. https://doi.org/10.1002/biot.202100432.

[55] Menon S, K.s. SD, Agarwal H, Shanmugam VK. Efficacy of Biogenic Selenium Nanoparticles from an Extract of Ginger towards Evaluation on Anti-Microbial and Anti-Oxidant Activities. Colloid Interface Sci Commun 2019;29:1–8. https://doi.org/10.1016/j.colcom.2018.12.004.

[56] Qian F, Li X, Tang L, Lai SK, Lu C, Lau SP. Selenium quantum dots: Preparation, structure, and properties. Appl Phys Lett 2017;110:053104. https://doi.org/10.1063/1.4975358.

[57] Jiang X, Huang W, Wang R, Li H, Xia X, Zhao X, et al. Photocarrier relaxation pathways in selenium quantum dots and their application in UV-Vis photodetection. Nanoscale 2020;12:11232–41. https://doi.org/10.1039/C9NR10235C.

[58] Fujishima M, Tanaka K, Sakami N, Wada M, Morii K, Hattori T, et al. Photocatalytic Current Doubling-Induced Generation of Uniform Selenium and Cadmium Selenide Quantum Dots on Titanium(IV) Oxide. J Phys Chem C 2014;118:8917–24. https://doi.org/10.1021/jp410794j.

[59] Youngman TH, Nielsen R, Crovetto A, Seger B, Hansen O, Chorkendorff I, et al. Semitransparent Selenium Solar Cells as a Top Cell for Tandem Photovoltaics. Sol RRL 2021;5:2100111. https://doi.org/10.1002/solr.202100111.

[60] Yan B, Liu X, Lu W, Feng M, Yan H-J, Li Z, et al. Indoor photovoltaics awaken the world's first solar cells. Sci Adv 2022;8:eadc9923. https://doi.org/10.1126/sciadv.adc9923.

[61] Wang T, Yang L, Zhang B, Liu J. Extracellular biosynthesis and transformation of selenium nanoparticles and application in H2O2 biosensor. Colloids Surf B Biointerfaces 2010;80:94–102. https://doi.org/10.1016/j.colsurfb.2010.05.041.

[62] Kuo T-T, Wu C-M, Lu H-H, Chan I, Wang K, Leou K-C. Flexible x-ray imaging detector based on direct conversion in amorphous selenium. J Vac Sci Technol A 2014;32:041507. https://doi.org/10.1116/1.4882835.

[63] Reznik A, Zhao W, Ohkawa Y, Tanioka K, Rowlands JA. Applications of avalanche multiplication in amorphous selenium to flat panel detectors for medical applications. J Mater Sci Mater Electron 2009;20:63–7. https://doi.org/10.1007/s10854-007-9440-0.

[64] Zhou X, Gao P, Sun S, Bao D, Wang Y, Li X, et al. Amorphous, Crystalline and Crystalline/Amorphous Selenium Nanowires and Their Different (De)Lithiation Mechanisms. Chem Mater 2015;27:6730–6. https://doi.org/10.1021/acs.chemmater.5b02753.

[65] Vijayakumar S, Chen J, Divya M, Durán-Lara EF, Prasannakumar M, Vaseeharan B. A Review on Biogenic Synthesis of Selenium Nanoparticles and Its Biological Applications.

J Inorg Organomet Polym Mater 2022;32:2355–70. https://doi.org/10.1007/s10904-022-02366-1.

[66] Shirsat S, Kadam A, Naushad M, Mane RS. Selenium nanostructures: microbial synthesis and applications. RSC Adv 2015;5:92799–811. https://doi.org/10.1039/C5RA17921A.

[67] Chhabria S, Desai K. Selenium Nanoparticles and Their Applications, 2016, p. 1–32.

[68] Bisht N, Phalswal P, K. Khanna P. Selenium nanoparticles: a review on synthesis and biomedical applications. Mater Adv 2022;3:1415–31. https://doi.org/10.1039/D1MA00639H.

[69] Mondal K, Roy P, Srivastava SK. Facile Biomolecule-Assisted Hydrothermal Synthesis of Trigonal Selenium Microrods. Cryst Growth Des 2008;8:1580–4. https://doi.org/10.1021/cg7008557.

[70] Mayers BT, Liu K, Sunderland D, Xia Y. Sonochemical Synthesis of Trigonal Selenium Nanowires. Chem Mater 2003;15:3852–8. https://doi.org/10.1021/cm034193b.

[71] Chen Q, Liu T, Chen S, Luo Y, Ma M, Xue F, et al. Targeted Therapeutic-Immunomodulatory Nanoplatform Based on Noncrystalline Selenium. ACS Appl Mater Interfaces 2019;11:45404–15. https://doi.org/10.1021/acsami.9b15774.

[72] Letavayová L, Vlasáková D, Spallholz JE, Brozmanová J, Chovanec M. Toxicity and mutagenicity of selenium compounds in Saccharomyces cerevisiae. Mutat Res Mol Mech Mutagen 2008;638:1–10. https://doi.org/10.1016/j.mrfmmm.2007.08.009.

[73] Selenium nanomaterials in biomedicine—An overview of new opportunities in nanomedicine of selenium. J Drug Deliv Sci Technol 2018;46:223–33. https://doi.org/10.1016/j.jddst.2018.05.023.

[74] Khurana A, Tekula S, Saifi MA, Venkatesh P, Godugu C. Therapeutic applications of selenium nanoparticles. Biomed Pharmacother 2019;111:802–12. https://doi.org/10.1016/j.biopha.2018.12.146.

[75] Geoffrion LD, Hesabizadeh T, Medina-Cruz D, Kusper M, Taylor P, Vernet-Crua A, et al. Naked Selenium Nanoparticles for Antibacterial and Anticancer Treatments. ACS Omega 2020;5:2660–9. https://doi.org/10.1021/acsomega.9b03172.

[76] Yazdi MH, Varastehmoradi B, Faghfuri E, Mavandadnejad F, Mahdavi M, Shahverdi AR. Adjuvant Effect of Biogenic Selenium Nanoparticles Improves the Immune Responses and Survival of Mice Receiving 4T1 Cell Antigens as Vaccine in Breast Cancer Murine Model. J Nanosci Nanotechnol 2015;15:10165–72. https://doi.org/10.1166/jnn.2015.11692.

[77] Song X, Chen Y, Sun H, Liu X, Leng X. Physicochemical and functional properties of chitosan-stabilized selenium nanoparticles under different processing treatments. Food Chem 2020;331:127378. https://doi.org/10.1016/j.foodchem.2020.127378.

[78] Vimala K, Maruthupandian A, Thangaraj R, Kannan S. Selenium Tethered Mesoporous Silica Nanocomposite Enhances Drug Delivering Efficiency to Target Breast Cancer. J Clust Sci 2020. https://doi.org/10.1007/s10876-020-01906-4.

[79] Oh E, Liu R, Nel A, Gemill KB, Bilal M, Cohen Y, et al. Meta-analysis of cellular toxicity for cadmium-containing quantum dots. Nat Nanotechnol 2016;11:479–86. https://doi.org/10.1038/nnano.2015.338.

[80] Kirchner C, Liedl T, Kudera S, Pellegrino T, Muñoz Javier A, Gaub HE, et al. Cytotoxicity of Colloidal CdSe and CdSe/ZnS Nanoparticles. Nano Lett 2005;5:331–8. https://doi.org/10.1021/nl047996m.

[81] Lam C-W, James JT, McCluskey R, Hunter RL. Pulmonary Toxicity of Single-Wall Carbon Nanotubes in Mice 7 and 90 Days After Intratracheal Instillation. Toxicol Sci 2004;77:126–34. https://doi.org/10.1093/toxsci/kfg243.

[82] Warheit DB, Laurence BR, Reed KL, Roach DH, Reynolds GAM, Webb TR. Comparative Pulmonary Toxicity Assessment of Single-wall Carbon Nanotubes in Rats. Toxicol Sci 2004;77:117–25. https://doi.org/10.1093/toxsci/kfg228.

[83] Tugarova AV, Mamchenkova PV, Dyatlova YA, Kamnev AA. FTIR and Raman spectroscopic studies of selenium nanoparticles synthesised by the bacterium *Azospirillum thiophilum*. Spectrochim Acta A Mol Biomol Spectrosc 2018;192:458–63. https://doi.org/10.1016/j.saa.2017.11.050.

[84] Martin RM, Lucovsky G, Helliwell K. Intermolecular bonding and lattice dynamics of Se and Te. Phys Rev B 1976;13:1383–95. https://doi.org/10.1103/PhysRevB.13.1383.

[85] Toulouse C, Amoroso D, Xin C, Veber P, Hatnean MC, Balakrishnan G, et al. Lattice dynamics and Raman spectrum of ${\mathrm{BaZrO}}_{3}$ single crystals. Phys Rev B 2019;100:134102. https://doi.org/10.1103/PhysRevB.100.134102.

[86] Poborchii VV, Kolobov AV, Tanaka K. An in situ Raman study of polarization-dependent photocrystallization in amorphous selenium films. Appl Phys Lett 1998;72:1167–9. https://doi.org/10.1063/1.121002.

[87] Misawa M, Suzuki K. Ring-Chain Transition in Liquid Selenium by a Disordered Chain Model. J Phys Soc Jpn 1978;44:1612–8. https://doi.org/10.1143/JPSJ.44.1612.

[88] Goldan AH, Li C, Pennycook SJ, Schneider J, Blom A, Zhao W. Molecular structure of vapor-deposited amorphous selenium. J Appl Phys 2016;120:135101. https://doi.org/10.1063/1.4962315.

[89] Rubio F, Rubio J, Oteo JL. A DSC study of the drying process of TEOS derived wet silica gels. Thermochim Acta 1997;307:51–6. https://doi.org/10.1016/S0040-6031(97)00309-2.

[90] Tran TN, Anh Pham TV, Phung Le ML, Thoa Nguyen TP, Tran VM. Synthesis of amorphous silica and sulfonic acid functionalized silica used as reinforced phase for polymer electrolyte membrane. Adv Nat Sci Nanosci Nanotechnol 2013;4:045007. https://doi.org/10.1088/2043-6262/4/4/045007.

[91] Bertoluzza A, Fagnano C, Antonietta Morelli M, Gottardi V, Guglielmi M. Raman and infrared spectra on silica gel evolving toward glass. J Non-Cryst Solids 1982;48:117–28. https://doi.org/10.1016/0022-3093(82)90250-2.

[92] Ann Mary KA, Unnikrishnan NV, Philip R. Ultrafast optical nonlinearity in nanostructured selenium allotropes. Chem Phys Lett 2013;588:136–40. https://doi.org/10.1016/j.cplett.2013.09.069.

[93] Mary KAA, Unnikrishnan NV, Philip R. Role of surface states and defects in the ultrafast nonlinear optical properties of CuS quantum dots. APL Mater 2014;2:076104. https://doi.org/10.1063/1.4886276.

[94] Khan MM, Ansari SA, Pradhan D, Han DH, Lee J, Cho MH. Defect-Induced Band Gap Narrowed CeO_2 Nanostructures for Visible Light Activities. Ind Eng Chem Res 2014;53:9754–63. https://doi.org/10.1021/ie500986n.

[95] Qasrawi AF, Aloushi HD. In situ monitoring of the permanent crystallization, phase transformations and the associated optical and electrical enhancements upon heating of Se thin films. Phys B Condens Matter 2019;569:62–7. https://doi.org/10.1016/j.physb.2019.05.038.

[96] Anupama K, Paul T, Ann Mary KA. Solid-State Fluorescent Selenium Quantum Dots by a Solvothermal-Assisted Sol–Gel Route for Curcumin Sensing. ACS Omega 2021;6:21525–33. https://doi.org/10.1021/acsomega.1c02441.

[97] Puri A, Mohite P, Ansari Y, Mukerjee N, M. Alharbi H, Upaganlawar A, et al. Plant-derived selenium nanoparticles: investigating unique morphologies, enhancing therapeutic uses, and leading the way in tailored medical treatments. Mater Adv 2024. https://doi.org/10.1039/D3MA01126G.

Chapter-3

Trigonal selenium quantum dots for fluorescence sensing applications

Toward the need for solid-state fluorescent quantum dots, resistant to self-quenching, we analysed the optical features of trigonal Se quantum dots synthesized via sol-gel assisted solvothermal route. Morphological and crystalline characterizations reveal that Se quantum dots (average size 3-8 nm) have a trigonal crystal structure. The presence of planar defects (dislocations, stacking faults, twins and grain boundaries) suggests formation of Se nanocrystallites through aggregation-based crystal growth mechanisms. Under ultraviolet excitation, the quantum dots exhibit an excitation wavelength-dependent solid-state blue emission with an average lifetime of 1.96 ns. Depending on fluorescence quenching by curcumin, selenium quantum dots act as ideal candidates for inner filter effect-based curcumin sensing.

3.1. INTRODUCTION

Nanomaterials have been an intriguing subject of research for last several decades as their physical properties can be drastically changed by tailor-made structural and morphological modifications. Presence of discrete energy states, tunable band gap and enhanced fluorescent properties makes elemental quantum dots (QDs) a promising candidate compared to its one-dimensional or two-dimensional counterparts. More recently, fluorescent quantum dots of graphene[1], phosphorous[2], boron[3], selenium[4] etc have attracted increased attention because of their intrinsic fluorescent properties making them promising candidates for development of biosensing and bioimaging platforms. Among them, selenium has an inimitable position at the boundary of group VI in the Periodic Table between van der Waals molecular solids (O_2 and S_8) and covalent solid Te. It can exist in several solid modifications: two monoclinic (α and β), the most stable trigonal form, a cubic and an amorphous modification[5]. Prior studies widely focussed on amorphous Se (a-Se) nanoparticles and trigonal Se (t-Se) nanowires due to their ease of formation and stability[6–9]. Dependence of ultrafast optical nonlinearity on cubic and amorphous forms of Se quantum dots are studied in silica xerogel prepared through a simple sol-gel route[5]. Though some progress has been achieved in the synthesis of t-Se nanoparticles[7,10,11] through green assisted synthesis as well as precursor conversion methods, synthesis of t-Se quantum dots are not equally explored. Recently, t-Se QDs is synthesized by ultrasound liquid-phase exfoliation (LPE) of $NbSe_2$ powders using N-Methyl-2-pyrrolidone (NMP) as the dispersant[12].

Photocarrier dynamics and pathways involved in t-Se QDs synthesised by a similar LPE method are also studied in a very recent work[13]. Research efforts are increasing progressively to explore simple methods to synthesize different Se QDs allotropes. Moreover, considering the influence of crystal defects on physical properties of a material, it is crucial to understand the growth mechanism and microstructure of Se QDs which are not well explored yet.

3.1.1. Fluorescence sensing

Fluorescence sensing of different analytes is a widely explored area of research. The fluorescence intensity of a fluorophore is always measured against a dark background independent of a reference beam unlike in absorbance measurements where light intensity is compared with a reference beam. This endows selectivity and sensitivity to luminescence-based sensing measurements. Rapid, highly sensitive detection with cost effectiveness, high selectivity and real-time sensing capabilities makes the phenomenon one of the widely used sensing routes.

Many spectral observables and their changes are widely employed for fluorescence sensing. The most common and direct method is using fluorescence intensity of a fluorophore. The interaction of fluorophore with the analyte/intermediate entities causes perceptible changes to the fluorescence intensity of the fluorophore that could be recorded by a fluorimeter. Other observables include change in polarisation or anisotropy of the light, time domain fluorescence lifetimes and even phase modulation.

3.1.1.1. Fluorescence quenching & its mechanism

Fluorescence quenching can be termed as the process that diminish the fluorescence intensity of a fluorophore. Molecule interactions like rearrangements, excited-state reactions, collisional quenching, ground state complex formation, energy transfer etc. can deplete the fluorescence intensity of the material. Among these, some quenching mechanisms are initiated with molecular contact between the fluorophore and quencher- dynamic and static quenching. In ***dynamic quenching*** (or collisional quenching), collisional encounters between the entities takes place. The quencher diffuses into the fluorophore and upon contact, it absorbs the energy from the fluorophore during its excited lifetime; the fluorophore returns to the ground state without photon emission. No reaction processes or change in the structure of the system is anticipated during dynamic quenching. Static quenching on the contrary, is characterized by the formation of a non-fluorescent ground state complex formation between the fluorophore and the quencher. These quenching mechanisms can be further differentiated through time resolved fluorescent decay measurements of the material in the presence and absence of the quencher. In case of collisional quenching, the photoexcited molecule interacts briefly with a quencher molecule and consequently loses its energy to the quencher depopulating the excited state. As a result, the excited state life-time of the fluorophore in the absence and presence of the quencher analyte is different. Dynamic quenching is depicted by the Stern-Volmer (SV) equation

$$\frac{F_0}{F} = 1 + k_q \tau_0 \, [Q] = 1 + K_D [Q] \tag{3.1}$$

$$\frac{F_0}{F} = \frac{\tau_0}{\tau} \tag{3.2}$$

where, F_0 and F are the fluorescence intensities, τ_0 and τ are the lifetimes of the fluorophore in the absence and presence of quencher, respectively; k_q and K_D are the bimolecular quenching constant and Stern-Volmer dynamic quenching constant, respectively, and $[Q]$ is the quencher concentration.

Static quenching involves ground state complex formation between the fluorophore and the analyte; any unbound fluorophore would decay in its natural lifetime τ_0, even in the presence of the quencher thereby causing no change in decay lifetimes. The quenching is governed by the equation

$$\frac{F_0}{F} = 1 + K_S[Q] \tag{3.3}$$

$$\frac{\tau_0}{\tau} = 1 \tag{3.4}$$

where K_S is the Stern-Volmer constant for static quenching process. A linear Stern-Volmer plot is generally indicates a single class of fluorophores which are all equally accessible to quencher, or in simple terms, single type of quenching-either static or dynamic.

However, in some cases, the fluorescence quenching results in materials by both collisional quenching and ground state complex formation. The Stern-Volmer equation can be hence modified to

$$\frac{F_0}{F} = (1 + K_S\,[Q])(1 + K_D[Q]) = 1 + (K_S + K_D)[Q] + K_S K_D[Q]^2 \tag{3.5}$$

This second order in $[Q]$ accounts for the upward curvature observed when both static and dynamic quenching occur for the same fluorophore.

Other factors that can distinguish these quenching mechanisms are:

- Dependence on temperature & viscosity- At higher temperatures, diffusion rates increase and dynamic quenching increases, while in static quenching, breakdown of the weakly bound ground -state complex at higher temperatures diminishes the static quenching.
- Steady state absorption spectra- As dynamic quenching is characteristic of the excited state, no perturbation in the ground state absorption spectra is expected while the absorption spectrum of the fluorophore in static quenching exhibit discernible perturbation.
- Bimolecular quenching constant k_q- For dynamic quenching values ~10^{10} M^{-1} sec^{-1}; value is generally several orders larger than 10^{10} M^{-1} sec^{-1} for static quenching.

Fluorescence quenching based systems can typically be turn-off, turn-on or ratiometric sensing systems (**Figure 3.1**).

3.1.1.2. Turn-off/ turn-on fluorescence sensing

In turn-off mode, with increase in analyte concentration, the absorption of the absorber increases, diminishing the luminescence intensity of the fluorophore. An example in this regard could be Zhang et.al's work on IFE based fluorescence detection of curcumin using nitrogen doped carbon QDs[14]. In some cases, the analyte itself acts as the absorber. Nevertheless, turn-off sensing is often reputed with false positive signals due to other interferences and is less sensitive to analyte concentration due to high background noise in comparison with turn-on systems. In turn-on sensing, the absorber turn-off the

fluorescence, and then the analyte restores the signal via chemical/biochemical pathways, e.g., absorber dissolution, oxidation-reduction, and complexation. Shang et.al, reported the turn-on IFE strategy to detect cyanide using Ag NPs as absorber and a water-soluble conjugated polymer PFS as the fluorophore[15]. The fluorophore emits weakly in the presence of Ag NPs due to the intensive absorption of Ag NPs to both the excitation and emission light. In the presence of cyanide, Ag NPs will dissolve upon their interaction with cyanide, which then leads to decreased absorbance of Ag NPs. As a result, the IFE-decreased emission of the fluorophore is restored, based on which cyanide can be detected in a simple and sensitive approach.

3.1.1.3. Ratiometric fluorescence sensing

In ratiometric sensing, analyte concentrations are determined by measuring the ratios of the emission at two different wavelengths. It offers a self-calibrating method that can eliminate the effects of different analyte-related parameters and false signals into the system. In addition to this, it also offers an easy-to-differentiate intensity and color change of the fluorescence system. IFE induced fluorescence quenching of carbon dots was used for the ratiometric sensing of uranyl ions in real water samples[16]. IFE can also exist in combination with other optical sensing mechanism like static quenching, photoinduced electron transfer (PET) or Förster resonant energy transfer (FRET).

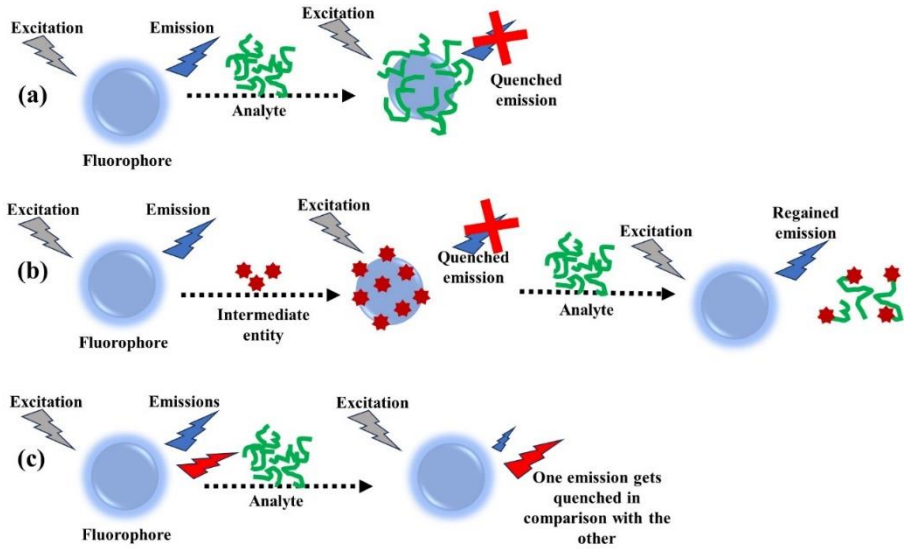

Figure 3.1. Schematic diagram showing the various strategies in IFE based optical sensors (a) turn-off, (b) turn-on and (c) ratiometric detection of analytes.

3.1.1.4. Inner filter effect

It was observed by Stokes, that in an optically dense solution, the fluorescence was observed from the solution surface that is exposed to incident light. The fluorescence intensity of a system with many non-interacting fluorophores is simply the sum of their individual contributions. Inner Filter Effect (IFE) refers to the absorption of the excitation and/or emission light of a fluorescer by an absorber in the system. The IFE was typically considered as an inconvenient source of error in spectrofluorometry. However, researchers tend to restore the fluorescer-absorber interaction by accounting for the error due to IFE. The changes in absorbance of the absorber are reflected in exponential scale in the fluorescence intensity of the fluorophore which allows sensitive and

stable detection strategies in sensors. The efficiency of the IFE based optical sensor relies on the following conditions and consequently on the suitable choice of fluorescer-absorber pair.

- Considerable spectral overlap must exist between the absorption spectrum of absorber and the excitation and/or emission spectrum of fluorescer.
- The fluorescence of the material should be independent of the analyte.
- External factors should not interfere with the absorption/ emission features of the entities.
- Generally, fluorescer -absorber pairs are expected to be charge repulsive so that the fluorescence of the fluorescer is not quenched.

In comparison with other sensing routes, IFE based sensors are advantageous as they are sensitive when compared to various UV-vis absorption measurements at lower concentrations, economical and flexible with the choice of absorber and fluorescer as they do not need to have any chemical link with one another. The response slope, range, limits of detection could be easily tuned by controlling the relative amounts of absorber and fluorescer in the system.

3.1.2. Solvothermal assisted sol-gel route

The conventional sol-gel route is often tailored to the need and requirements of the target material. This is often achieved by modifying the prime factors that affect the sol-gel process like pH, temperature, pressure, time, solvent and its concentration, presence of catalyst etc. The polycondensation reactions that takes place in the sol-gel process reinforce the gel with additional

cross-links which further lead to shrinkage of the medium thereby expelling the solution from the pores. The remaining amount of the solvent is removed via drying or calcination. Solvothermal assisted sol gel route aims to accelerate the gel formation from the sol in a restricted time under elevated temperature and pressure. This causes easier formation of nanoparticles in a quicker pace due to high temperature and pressure but with crystal defects in the lattice. The solvothermal route initiates rapid hydrolysis and polycondensation reaction of the sol with simultaneous expulsion of the solvent from the pores. Elevated temperature and pressure alter the kinetics of the reaction and interaction among the precursors thereby easily precipitating out the solid from the liquid.

3.1.3. Defects in crystals

Despite how carefully they are synthesized or how controlled the synthesis environment was, crystals will always show some deviations from ideal arrangement of the crystal lattice. These lattice imperfections or 'defects' that arise from the irregular periodic arrangement are classified by the region of the sample over which they extend. They are hence broadly categorised as:

- *Point defects*

These imperfections do not extend more than few lattice points and are generally termed as zero-dimensional defects. It can be due to an impurity that occupies the place of an atom in the crystal (*substitutional impurity*) or an impurity that squeezes into the interstitial of the lattice (*interstitial impurity*). Such defects can also result, especially in ionic crystals when a lattice site is

vacant (*vacancy defect/Schottkey defect*) or when the atom/ion appears in the interstitial sites of the lattice (*interstitial defect/Frenkel defect*).

- *Line defects, dislocations*

Line defects are generally deviations from crystal structure along one direction- in a straight or curved line as a result of mechanical strain or as a result of crystal growth and are generally termed as dislocation. *Edge dislocation* is a defect where an extra portion of a plane is introduced through the crystal causing structural rearrangement in the lattice. Here, this rearrangement is perpendicular to the line of dislocation and limited to the vicinity of the line. On the other hand, a screw *dislocation* is a consequence of two portions in the crystal that slip in opposite directions relative to each other, parallel to the line of dislocation. Dislocations in crystals are usually a combination of both these defects and are termed as *mixed dislocation*.

- *Planar defects*

Planar defects are generally termed for the discontinuities that occur between the homogenous regions of a crystal. They can be either in the form of grain boundaries, stacking faults or twin boundaries in the crystal. During the formation of polycrystalline materials, the crystal growth starts independently in each nucleus with random axis of orientation relative to the surrounding nuclei. As a result, with the growth of the crystal, long range order is restricted to certain macroscopic regions within the crystals called grains or crystallites. The irregularities that occur along the interface of such two crystallites are called *grain boundaries. Stacking faults* are basically local deviations in the stacking or

arrangement of subsequent atomic layers in a crystal lattice which gives rise to a crystal defect over the extended 2D surface. The widely known stacking fault occurs in face-centered cubic (fcc) metals where the stacking sequence of (111) layers i.e, ABCABCABCABC gets stacked ABCAB||ABCABC with a lattice plane C missing in the order (intrinsic stacking fault). Sometimes it can also happen such that a new lattice layer might get inserted resulting in the change in their arrangement. For example, with the addition of a C-type layer, ABABABABAB stacking would be ABAB**C**ABABAB thereby causing faults in the arrangement of atomic layers (extrinsic stacking fault). *Twin boundary* refers to the defects at a surface that separates two different crystallites which are mirror images of one another. For instance, if in the fcc crystal structure ABCABCABC, an extrinsic defect occurs to the right of |C|, the defect energy is minimised with the addition of B to the right of C followed by A-plane to accommodate fcc packing in crystal. This results in the stacking sequence ABCAB|C|BACBAC. Here plane C is the twin boundary while the fcc lattices ABCAB and BACBA are mirror images of one another.

- *Volume defects*

Volume defects in crystals are macroscopic regions in a polycrystalline material with crystallographic arrangement different from the remaining regions of the material. These could be 3D aggregates of vacancies as in *voids or pores*, or intentionally introduced *inclusions*, or *precipitates* or *dispersants*.

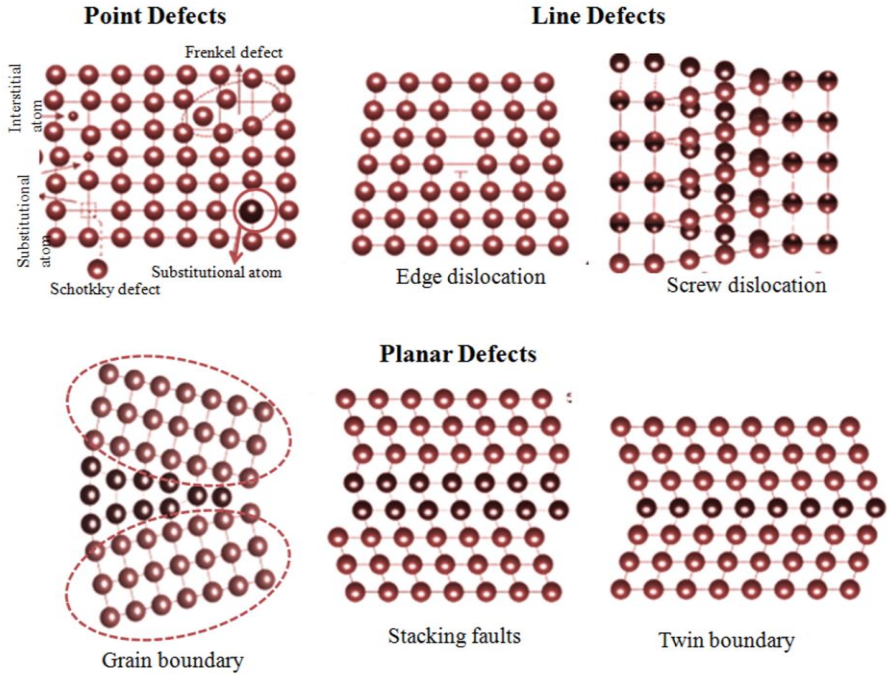

Figure 3.2. Point, line and planar defects in crystal.

3.1.4. Curcumin

Turmeric (*Curcumin longa*) is a popular spice and a folklore medicine that has been used since early times in major parts of Indian subcontinent and other parts of southern and south-western tropical Asia[17]. Chemically named as 1,7-bis-(4-hydroxy-3-methoxyphenyl)-hepta-1,6-diene-3,5- dione or dipheruloylmethane (chemical formulae- $C_{21}H_{20}O_6$), curcumin (CR) is the principal curcuminoid found in turmeric[18]. This component is primarily responsible for the bright orange-yellow color of turmeric. It is widely used as a nutraceutical in food and both as a colorant and condiment. Other curcuminoids

from the herb extract includes demethoxycurcumin and bis-demethoxycurcumin[19].

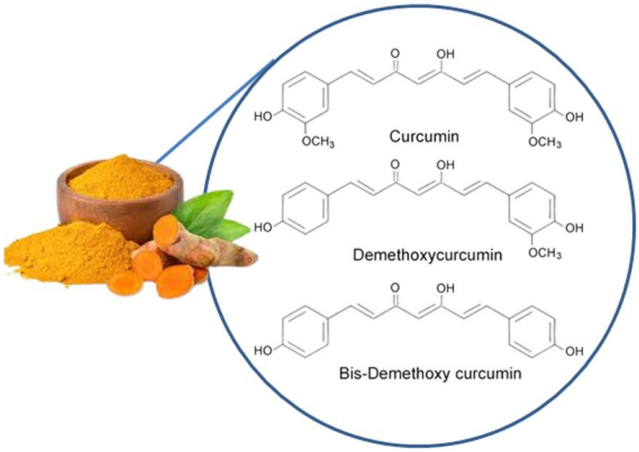

Figure 3.3. Turmeric and its constituent curcuminoids.

Of all these lipophilic, polyphenolic components of turmeric, studies shows that curcumin possess exceptional biological and pharmacological properties[20]. Though utilised for its anti-bacterial[21], anti-inflammatory[22], anti-oxidant[23] and hepatoprotective properties[24], curcumin shows good inhibitory effects towards certain carcinogens[25,26]. It is used in clinical medicine for the treatment of various diseases like arthritis, cystic fibrosis[27], cardiovascular diseases[28], Alzhimer's[29] and even HIV[30]. However studies suggest that excessive dose of curcumin can impose higher oxidative stress resulting in chromosomal aberrations to mitochondria and nuclear genomes in human hepatoma G2 cells[31]. Moreover, it decreases intracellular ATP levels triggering necrosis process[32]. Owing to its wide importance and medicinal value, it is highly desirable to monitor the level of curcumin in foods

and medications through a reliable, fast and sensitive route. Till date, various analytical assays have been reported for the detection of curcumin including high performance liquid chromatography[33], voltammetry [34], electrochemical methods[35], capillary electrophoresis[36], spectrophotometry[37], resonance light scattering[38] and spectrofluorimetry[39,40]. Although many of these are very sensitive and quantitative techniques, high capital and maintenance expense attracted researchers towards sensitive, quick responsive and cost-effective fluorescence sensing. Recently, various flurophores such as P, N, B-co-doped carbon quantum dots[41], Mn doped ZnS QDs[42], graphitic carbon nitrides[43], etc have been exploited as fluorescent nanosensors for quantitative determination of curcumin. But QDs tend to lose their fluorescence properties in aqueous and solid-state due to irreversible photobleaching or aggregation-induced luminescence quenching[44,45]. This limits their practical applicability in designing sensors and imaging devices where materials with solid state fluorescence are inevitable.

Herein, a facile solvothermal route is explained for in-situ synthesis of Se quantum dots in SiO_2 matrix. In solid mesoporous silica, collision and aggregation of Se QDs can rarely happen preventing them from degradation and surface oxidation. This gives longer shelf life making them ideal candidates for solid state fluorescence and optoelectronic applications. This stable solid-state fluorescence obtained from Se QDs are explored for quantitative determination of curcumin.

3.2. EXPERIMENTAL SECTION

3.2.1. Materials

Tetraethyl Orthosilicate (TEOS) (Si $(OC_2H_5)_4$, 98%), selenous acid (H_2SeO_3, 98%), and curcumin ($[HOC_6H_3(OCH_3)CH=CHCO]_2CH_2$, from *Curcuma longa* (Turmeric) powder) were procured from Sigma-Aldrich. Distilled water was used throughout the experiment.

3.2.2. Apparatus and Characterization

The crystallinity of the sample was observed using a benchtop Powder X-ray Diffractometer (Aeris Research, PANalytical, Netherlands) with a scanning range of 2θ =10° to 90° with Cu K_α radiation (λ=1.540598 Å). Morphological parameters were evaluated from Field Emission Scanning Electron Microscopy (FESEM) images from TESCAN MIRA3 LMH and High-Resolution Transmission Electron Microscopy (HRTEM) data from a TALOS F200S G2 Transmission Electron Microscope (200KV, FEG, CMOS Camera 4k x 4k). Raman spectra obtained from Horiba Jobin Yvon T64000 Raman spectrometer was used for phase identification. The absorption spectra in the entire visible range were recorded on a UV Vis spectrophotometer (Jasco, Japan). All fluorescent measurements were recorded in a NIR Spectro Fluorimeter- Fluorolog (Horiba Jobin Yuvan USA). Decay lifetimes were evaluated using a Time Resolved Fluorimax Fluorimeter (Horiba Jobin Yuvan USA)

3.2.3. Synthesis of Se- silica composite

10 wt%, 20 wt%, 30 wt% and 40 wt% Se in 2 g silica was prepared by simple solvothermal route through rapid hydrolysis, condensation and polymerization of tetraethyl orthosilicate (TEOS) in the presence of ethanol and distilled water. Aqueous solution of selenous acid was added to TEOS and ethanol at room temperature. The precursor molar ratio of selenium to silica was fixed at 1:2, 1:3, 1:5 and 1:11 for the synthesis of 40 wt%, 30 wt%, 20 wt% and 10 wt% of se-silica nanocomposite respectively. 2 drops of 1 M HNO_3 was added as a catalyst. The resulting mixture was stirred continuously for 1 hour to obtain a clear solution. The molar ratio of TEOS: Water: Ethanol was taken as 1:2:2. The solution was then poured into 50 mL Teflon-lined autoclave and heated at 150 °C for 24 hours. The grey coloured composite obtained was powdered and used for further characterizations.

3.2.4. Determination of curcumin

For quantitative determination of curcumin in different systems, 0.2 g of 40 wt% Se-SiO_2 was added to varying wt% of chloroform solutions of curcumin (10 mL). The solution was then centrifuged and washed with excess of solvent to remove the loosely bound residues. The mixture was then dried and optical properties of slightly yellowish powder obtained were investigated by fluorescence spectroscopy.

3.3. RESULTS AND DISCUSSION

3.3.1. Powder X-Ray Diffraction (p-XRD)

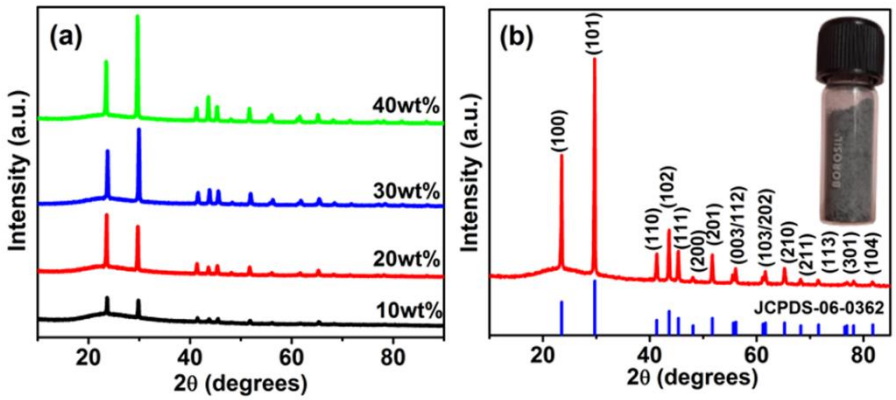

Figure 3.4.(a) XRD pattern of Se-SiO_2 composites with different Se contents. (b) XRD pattern of 40 wt% of Se-SiO_2 composite. The inset shows its digital photograph under visible light.

Powder X-ray diffraction (p-XRD) pattern of Se-SiO_2 composites with different Se contents are shown in **Figure 3.4(a)**. It can be inferred that all Se-SiO_2 composites have same crystal structure as peak positions in p-XRD pattern remain same and their intensities increases with Se contents. As shown in the **Figure 3.4(b)**, occurrence of diffraction peaks at different positions can be indexed to hexagonal Se (JCPDS code: 06-0362) and no impurities peaks are detected. Broad spectrum peaked at 2θ value of 23° in the p-XRD pattern can be ascribed to the presence of amorphous SiO_2. The **inset of Figure 3.4(b)** shows the photograph of 40 wt% Se-SiO_2 nanocomposite.

3.3.2. Scanning Electron Micrograph (SEM) & Transmission Electron Micrograph (TEM)

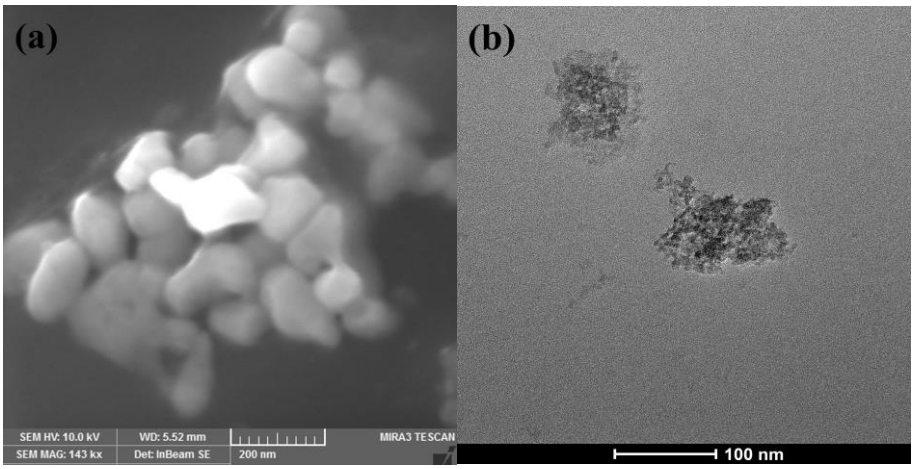

Figure 3.5. (a) FESEM and (b) TEM image of se-silica nanocomposite

The FESEM image (**Figure 3.5(a)**) of se-silica nanocomposite shows fused distorted ellipsoid like structures with average length in the range of 80 to 190 nm and diameter ranging from 60 to 120 nm. Large field TEM image given in **Figure 3.5(b)** clearly illustrates the same morphology of se-silica nanocomposites. The average length and breadth of microstructures is calculated as 130 nm and 110 nm respectively. Moreover, on close examination it can be inferred that each ellipsoid- like structure consists of many homogenously distributed quasi-spherical Se quantum dots with a very narrow size distribution.

3.3.3. High Resolution Transmission Electron Micrograph (HR-TEM)

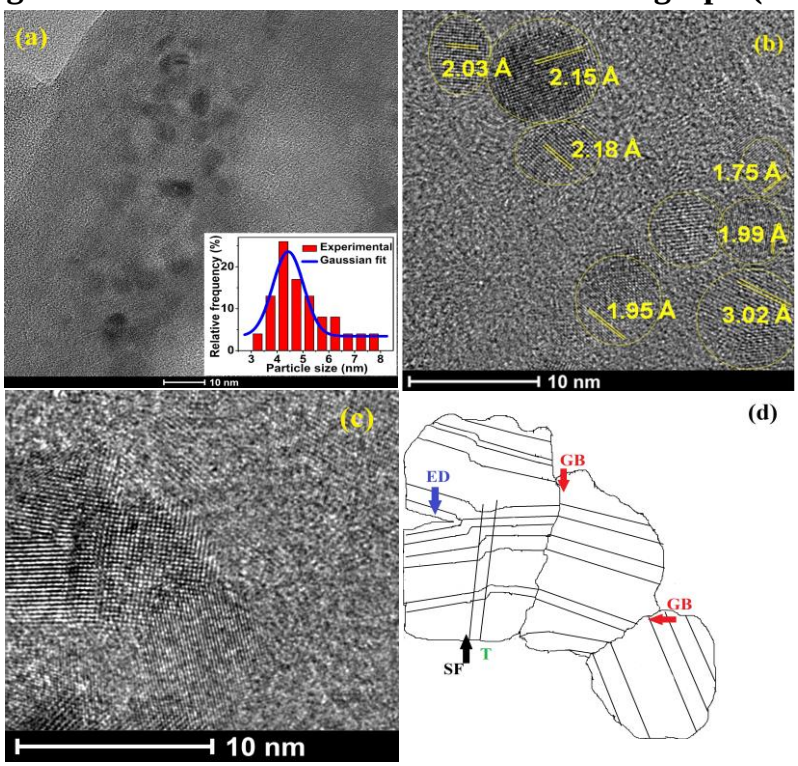

Figure 3.6. (a) Large area HRTEM image of Se-SiO_2 composite (inset shows particle size distribution of Se QDs); (b,c) HRTEM image of t-Se QDs showing d spacings; (d) Diagram illustrating edge dislocation (ED), stacking faults (SF), twins (T) and grain boundaries (GB) in the crystallites as observed from HRTEM.

The HRTEM image shows approximately spherical t-Se QDs distributed evenly without obvious aggregation (**Figure 3.6(a)**). The size of nanocrystallites is in the range of 3-8 nm as obtained from size distributions histogram (**inset of Figure 3.6(a)**). On closer examination, it can be observed that synthesized t-Se QDs (**Figure 3.6(b)**) exhibits randomly oriented crystallites with abrupt disordered edges having considerable grain boundary defects. Clear lattice

fringes revealed the excellent crystalline nature of t-Se QDs. The interplanar distance of 3.02 Å, 2.15 Å, 2.03 Å, 1.95 Å, 1.75 Å can be assigned to (101), (110), (102), (111) and (201) plane of trigonal Se. Upon deeper investigation it can be inferred that like among many nanocrystallites in the system, t-Se QDs possess considerable number of planar defects. **Figure 3.6(c)** shows presence of stacking faults (SF), edge dislocations (ED) and twins (T) which is depicted in **Figure 3.6(d)**. This can be attributed to aggregation-based crystal growth mechanism involved in the synthesis. During hydrothermal coarsening, adjacent primary particles in the solution collide and coalesce resulting in secondary particles. This spontaneous self-organisation following a common crystallographic orientation and imperfect particle attachment often leads to line and planar defects [46].

3.3.4. UV Visible absorption spectra & Tauc plot

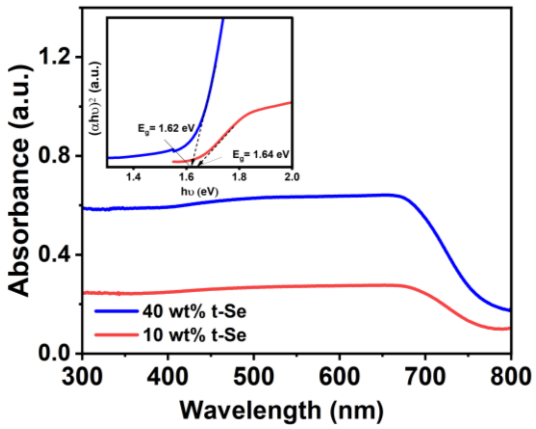

Figure 3.7. UV-visible absorption spectrum of t-$SeSiO_2$ composite; Tauc plot (inset) gives the optical bandgap as 1.6 eV.

The UV-visible absorption spectrum of t-Se quantum dots at 10 and 40 wt% concentration is given in **Figure 3.7**. The spectrum shows a broad absorption in lower wavelength region and an absorption edge is observed around 750 nm for 10 wt% t-Se-silica. A slight blue shift in the absorption edge to is noted for higher concentration of 40 wt%. Some previous studies are available in literature suggest that trigonal Se nanowires have weak absorption maxima at 346, 450 and 570 nm[47]. The semi-metallic nature of the material and the structural similarities with the bulk causes broadening of these individual peaks.[48] The optical band gap of t-Se QDs is calculated from Tauc plot (**inset of Figure 3.7**) as 1.64 eV and 1.62 eV for 10 and 40 wt% respectively. The slight decrease in the bandgap with increase in concentration can be attributed to the defect density in the material. According to values reported in literature trigonal selenium exhibits band gap energy value of 2 eV[13,49,50]. Though higher energy gap is expected in quantum dots due to confinement effects, slight decrease in band gap is observed in t-Se QDs. This can be attributed to the presence of surface states and traps[51,52]. Microstructural studies also indicate the presence of surface states and defects. Due to the smaller size of nanocrystallites, a higher proportion of the total number of atoms will be located on the surface. Moreover, the nanocrystallites have abrupt edges and imperfect surfaces. Therefore, there will be a large density of surface states, which act as active electron and/or hole traps upon optical excitation. The excited carriers undergo nonradiative recombination and

no band edge emission was observed for t-Se QDs, consistent with the results obtained for Jiang et.al[13].

3.3.5. Photoluminescence spectra

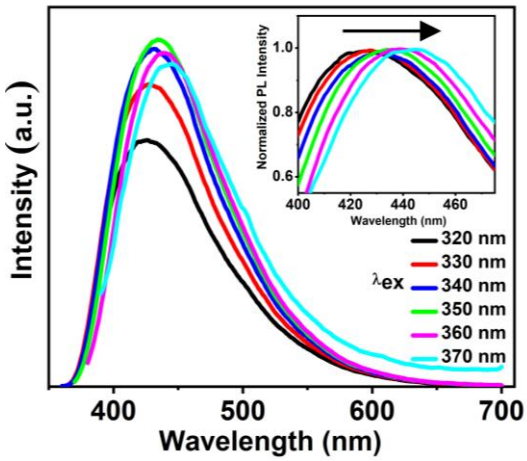

Figure 3.8. Photoluminescence spectra measured in t-Se-SiO_2 composite with varying λ_{ex} from 320 to 370 nm; Normalized PL spectra (inset) show excitation dependent emission.

Under UV excitation wavelength of 350 nm, t-Se-SiO_2 composite exhibit a blue emission peaked at 434 nm wavelength (**Figure 3.8**). This can be assigned to direct inter-band radiative recombination in t-Se QDs[13]. Due to spin orbit coupling, valance band and conduction band might undergo energy splitting and radiative recombination of carriers can happen in same k-space between energy bands. From normalised PL spectra it is clear that emission wavelength shifts from 418 nm to 449 nm when the excitation wavelength varies from 320-370 nm (**inset of Figure 3.8**). Observed red-shift in the emission peak suggests that prepared QDs possess an excitation wavelength-

dependent emission which is consistent with reported data[12]. The quantum yield (QY) estimation for t-Se QDs is obtained as ~0.13%. This low value of room temperature photoluminescence QY is due to high defect density in the material which is consistent with HRTEM and UV visible absorption data. The defect mediated non radiative recombination from surface states and trap sites outnumbers the number of photons emitted which results in reduced QY[53]. Similar quantum yield values have been reported for certain metal nanoclusters (NCs)[54] and some two-dimensional (2D) transition metal dichalcogenides like MoS_2[55] due to the presence of surface states and defects.

3.3.6. Fluorescence detection of food dyes

3.3.6.1. Sensing of curcumin

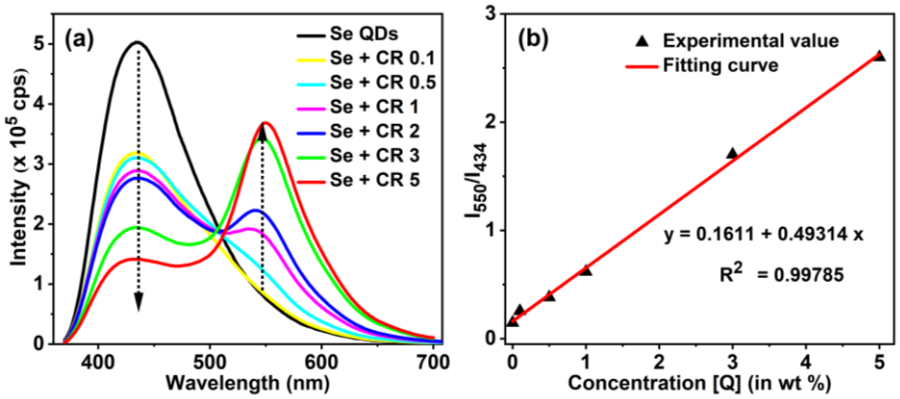

Figure 3.9. (a) Fluorescence responses of t-Se QDs in the presence of varying wt% of curcumin (from top: 0, 0.1, 0.5, 1, 2, 3 and 5 wt%) (b) Stern Volmer plot showing fluorescence intensity ratio (I_{550}/I_{434}) as a function of curcumin concentrations.

To examine the sensing ability of t-Se-SiO_2 composite for curcumin, steady state fluorescence emission spectra of t-Se QDs were closely monitored (**Figure 3.9(a)**) with different concentration of curcumin (0 to 5 wt% of 0.2 g Se-SiO_2 composite). It can be observed that the fluorescence intensity of t-Se QDs is decreased distinctly upon addition of curcumin. Moreover, increase in curcumin content results in occurrence of a new emission band peaked at 550 nm wavelength. The enhanced characteristic yellow emission of curcumin illustrates transfer of photon energy between curcumin and t-Se QDs. The ratio of fluorescence intensities peaked at 550 nm and 434 nm wavelength (I_{550}/I_{434}) shows a satisfactory linear relationship (**Figure 3.9(b)**) as concentration of the analyte varies from 0 to 5 wt% (~ 0 – 10.52 mg). The calibration equation is as follows:

$$I(550)/I(434) = 0.1611 + 0.49314[Q] \quad (3.6)$$

where I(434) and I(550) are the fluorescence intensities of emission bands at λ_{ex} of 350 nm and [Q] represents the concentration of curcumin. The limit of detection (LOD) was calculated to be 0.09 wt% (~180 μg) with LOD = 3σ/S, where σ is represents standard deviation of the pure Se QDs for N=3 and S is the slope of the calibration curve. The obtained value of R^2 = 0.99785 indicates very good linearity.

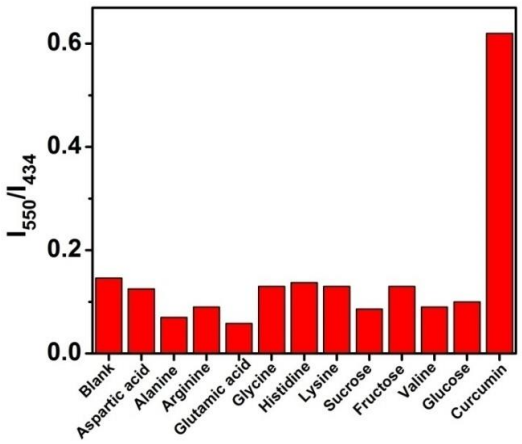

Figure 3.10. Selective fluorescence response (I_{550}/I_{434}) of the probe towards 1 wt% of various interferents like aspartic acid, alanine, arginine, glutamic acid, glycine, histidine, lysine, sucrose, fructose, valine, glucose and curcumin.

To assess the selectivity of the system towards curcumin, relative fluorescence responses (I_{550}/I_{434}) of t-Se-SiO_2 composite towards interfering analytes like aspartic acid, alanine, arginine, glutamic acid, glycine, histidine, lysine, sucrose, fructose, valine, glucose and curcumin were analysed. It is clear that only addition of curcumin makes a remarkable change in I_{550}/I_{434} value (**Figure 3.10**).

3.3.6.2. Mechanism of quenching

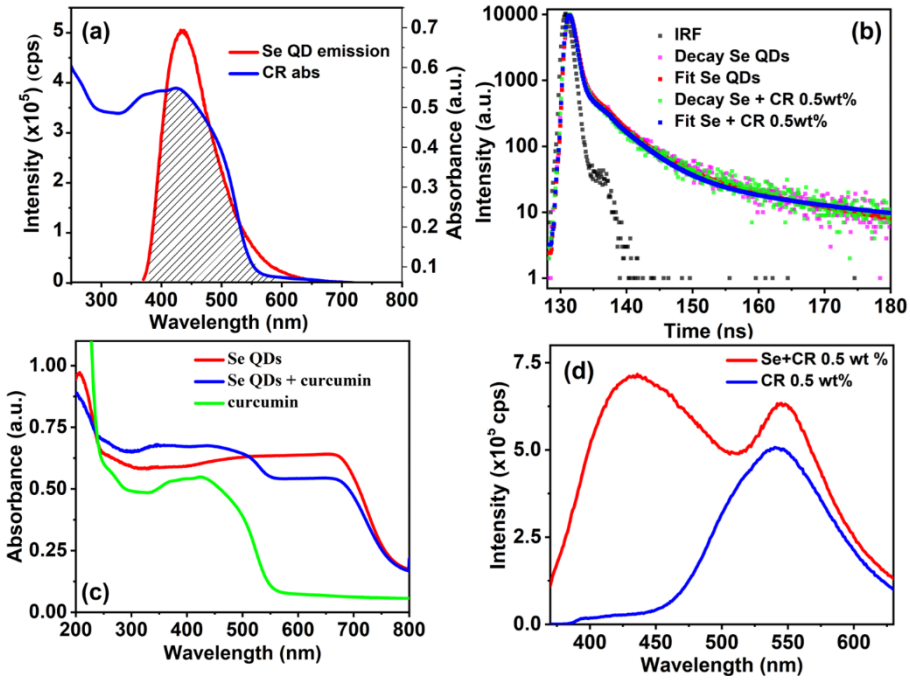

Figure 3.11 (a) UV-vis absorption spectrum of curcumin and emission spectrum of t-Se QDs showing spectral overlap (b) Fluorescent decay curves of t-Se QDs and t-Se QDs - curcumin (c) UV-vis spectra of t-Se QDs, curcumin and t-Se QD+curcumin (d) Photoluminescence spectra of 0.5 wt% curcumin and 0.5 wt% curcumin incorporated trigonal Se – silica nanocomposite showing transfer of photon energy

From **Figure 3.11(a)** it can be observed that the broad absorption of curcumin in short wavelength region has considerable overlap with the emission spectrum of t-Se QDs. This clearly indicates that the decrease in fluorescence of t-Se QDs upon addition of curcumin is due to electron transfer, energy transfer or Inner Filter Effect (IFE)[41,56–60]. As curcumin is negatively charged there won't be any electrostatic interaction between selenium QDs and

curcumin[41,61]. Thus, the fluorescence quenching observed in the mixture is not due to electron transfer mechanism. To understand the aforementioned quenching mechanism, time resolved fluorescent life time decay measurements were carried out at an excitation wavelength of 340 nm (**Figure 3.11(b)**). The fluorescence data was reliably fitted using a tri exponential decay function

$$I(t) = I(0) + \sum Ai * e^{\left(-\frac{t}{\tau i}\right)} \quad (3.7)$$

where τ_i represents the lifetime, A_i denotes the relative amplitude of the decay process while *I(0)* and *I(t)* refers to fluorescence intensities at 0 and t respectively[62]. The fitting parameters obtained are shown in **Table 3.1**. The average life time of t-Se QDs remains unchanged upon addition of 0.5 wt% curcumin. This implies that the excited fluorophore decays in its native natural lifetime and is not in any way bounded to the analyte. UV-Visible absorption spectra of t-Se QDs, Se-curcumin and curcumin are shown in **Figure 3.11(c)** and no additional peak can be observed in Se-curcumin spectrum. This eliminates any possible complex formation between Se and curcumin and possible quenching mechanism observed in Se-curcumin is IFE. The enhanced emission peaked at 550 nm wavelength for Se-curcumin composite compared to curcumin SiO_2 mixture at an excitation wavelength of 350 nm illustrates transfer of photon energy between curcumin and t-Se QDs (**Figure 3.11(d)**). This confirms fluorescence quenching mechanism of t-Se QDs as IFE without any chemical link between donor-acceptor systems. The results suggests that solid-state fluorescence from t-Se QDs can be well applied to less costly IFE based practical fluorescence sensors.

Table 3.1. Fluorescence lifetime parameters of t-Se in the absence and presence of curcumin

Curcumin (wt%)	τ_1 (ns)	a_1	τ_2 (ns)	a_2	τ_3 (ns)	a_3	τ_{avg} (ns)	χ^2
0	4.10	17.75	19.26	5.41	0.25	76.83	1.96	1.31
0.5	4.41	16.46	27.07	4.20	0.23	79.34	2.04	1.32

3.4. CONCLUSION

In summary, t-Se QDs in silica synthesized using solvothermal assisted sol-gel route was studied in detail. Structural evaluation of as synthesized Se-silica nanocomposites confirms the formation of trigonal Se QDs-SiO_2 composites. From HRTEM images, nanocrystallites with considerable planar defects were observed and the oriented attachment (OA) based crystal growth mechanism was discussed in detail. The lower band gap value of 1.6 eV calculated from UV-visible absorption measurements can be attributed to presence of surface states and traps. The blue emission observed for t-Se QDs under UV excitations were successfully utilized for the sensitive detection of curcumin. To the best of our knowledge, reports on solid-state fluorescence in trigonal Se QDs are not readily available in literature. The decrease in fluorescence intensity of t-Se QDs in the presence of curcumin was due to IFE based quenching mechanism which has significant applications toward designing instrument-free practical fluorescence sensors.

3.5. REFERENCES

[1] Yan X, Song Y, Zhu C, Song J, Du D, Su X, et al. Graphene Quantum Dot–MnO2 Nanosheet Based Optical Sensing Platform: A Sensitive Fluorescence "Turn Off–On" Nanosensor for Glutathione Detection and Intracellular Imaging. ACS Appl Mater Interfaces 2016;8:21990–6. https://doi.org/10.1021/acsami.6b05465.

[2] Li Y, Liu Z, Hou Y, Yang G, Fei X, Zhao H, et al. Multifunctional Nanoplatform Based on Black Phosphorus Quantum Dots for Bioimaging and Photodynamic/Photothermal Synergistic Cancer Therapy. ACS Appl Mater Interfaces 2017;9:25098–106. https://doi.org/10.1021/acsami.7b05824.

[3] Huo B, Liu B, Chen T, Cui L, Xu G, Liu M, et al. One-Step Synthesis of Fluorescent Boron Nitride Quantum Dots via a Hydrothermal Strategy Using Melamine as Nitrogen Source for the Detection of Ferric Ions. Langmuir 2017;33:10673–8. https://doi.org/10.1021/acs.langmuir.7b01699.

[4] Zhu M-L, Gao Z-T, Lu J-X, Wang Y, Wang G, Qiu Y, et al. Amorphous Nano-Selenium Quantum Dots Prevent Pulmonary Arterial Hypertension Through Recoupling Endothelial Nitric Oxide Synthase. Rochester, NY: Social Science Research Network; 2020.

[5] Mary KAA, Unnikrishnan NV, Philip R. Cubic to amorphous transformation of Se in silica with improved ultrafast optical nonlinearity. RSC Adv 2015;5:14034–41. https://doi.org/10.1039/C4RA14025G.

[6] Mondal K, Roy P, Srivastava SK. Facile Biomolecule-Assisted Hydrothermal Synthesis of Trigonal Selenium Microrods. Cryst Growth Des 2008;8:1580–4. https://doi.org/10.1021/cg7008557.

[7] Zhang J, Fu Q, Xue Y, Cui Z. Controlled synthesis of t-Se nanomaterials with various morphologies via a precursor conversion method. CrystEngComm 2018;20:1220–31. https://doi.org/10.1039/C7CE01998J.

[8] Gates B, Mayers B, Cattle B, Xia Y. Synthesis and Characterization of Uniform Nanowires of Trigonal Selenium. Adv Funct Mater 2002;12:219–27. https://doi.org/10.1002/1616-3028(200203)12:3<219::AID-ADFM219>3.0.CO;2-U.

[9] Liu L, Peng Q, Li Y. Preparation of monodisperse Se colloid spheres and Se nanowires using Na2SeSO3 as precursor. Nano Res 2008;1:403–11. https://doi.org/10.1007/s12274-008-8040-5.

[10] Kokila K, Elavarasan N, Sujatha V. Diospyros montana leaf extract-mediated synthesis of selenium nanoparticles and their biological applications. New J Chem 2017;41:7481–90. https://doi.org/10.1039/C7NJ01124E.

[11] Prasad KS, Selvaraj K. Biogenic Synthesis of Selenium Nanoparticles and Their Effect on As(III)-Induced Toxicity on Human Lymphocytes. Biol Trace Elem Res 2014;157:275–83. https://doi.org/10.1007/s12011-014-9891-0.

[12] Qian F, Li X, Tang L, Lai SK, Lu C, Lau SP. Selenium quantum dots: Preparation, structure, and properties. Appl Phys Lett 2017;110:053104. https://doi.org/10.1063/1.4975358.

[13] Jiang X, Huang W, Wang R, Li H, Xia X, Zhao X, et al. Photocarrier relaxation pathways in selenium quantum dots and their application in UV-Vis photodetection. Nanoscale 2020;12:11232–41. https://doi.org/10.1039/C9NR10235C.

[14] Zhang Q, Zhang C, Li Z, Ge J, Li C, Dong C, et al. Nitrogen-doped carbon dots as fluorescent probe for detection of curcumin based on the inner filter effect. RSC Adv 2015;5:95054–60. https://doi.org/10.1039/C5RA18176C.

[15] Shang L, Qin C, Jin L, Wang L, Dong S. Turn-on fluorescent detection of cyanide based on the inner filter effect of silver nanoparticles. The Analyst 2009;134:1477–82. https://doi.org/10.1039/b823471j.

[16] Nan H-R, Liu Y-H, Gong W-J, Peng H-B, Wang Y-Q, Zhang Z-B, et al. An inner-filter-effect based ratiometric fluorescent sensor for the detection of uranyl ions in real samples. Anal Methods 2022;14:532–40. https://doi.org/10.1039/D1AY02017J.

[17] Kocaadam B, Şanlier N. Curcumin, an active component of turmeric (Curcuma longa), and its effects on health. Crit Rev Food Sci Nutr 2017;57:2889–95. https://doi.org/10.1080/10408398.2015.1077195.

[18] Lestari MLAD, Indrayanto G. Chapter Three - Curcumin. In: Brittain HG, editor. Profiles Drug Subst. Excip. Relat. Methodol., vol. 39, Academic Press; 2014, p. 113–204. https://doi.org/10.1016/B978-0-12-800173-8.00003-9.

[19] Akram M, Afzal A, Khan U, Abdul H, Mohiuddin E, Asif M. Curcuma longa and Curcumin: A review article. Rom J Biol-Plant Biol 2010;55:65–70.

[20] Tønnesen HH, Karlsen J, Adhikary SR, Pandey R. Studies on curcumin and curcuminoids XVII. Variation in the content of curcuminoids inCurcuma longa L. from Nenal during one season. Z Für Lebensm-Unters Forsch 1989;189:116–8. https://doi.org/10.1007/BF01332943.

[21] Wang Y, Lu Z, Wu H, Lv F. Study on the antibiotic activity of microcapsule curcumin against foodborne pathogens. Int J Food Microbiol 2009;136:71–4. https://doi.org/10.1016/j.ijfoodmicro.2009.09.001.

[22] Bereswill S, Muñoz M, Fischer A, Plickert R, Haag L-M, Otto B, et al. Anti-Inflammatory Effects of Resveratrol, Curcumin and Simvastatin in Acute Small Intestinal Inflammation. PLOS ONE 2010;5:e15099. https://doi.org/10.1371/journal.pone.0015099.

[23] Menon VP, Sudheer AR. ANTIOXIDANT AND ANTI-INFLAMMATORY PROPERTIES OF CURCUMIN. In: Aggarwal BB, Surh Y-J, Shishodia S, editors. Mol. Targets Ther. Uses Curcumin Health Dis., Boston, MA: Springer US; 2007, p. 105–25. https://doi.org/10.1007/978-0-387-46401-5_3.

[24] Girish C, Koner BC, Jayanthi S, Rao KR, Rajesh B, Pradhan SC. Hepatoprotective activity of picroliv, curcumin and ellagic acid compared to silymarin on paracetamol induced liver toxicity in mice. Fundam Clin Pharmacol 2009;23:735–45. https://doi.org/10.1111/j.1472-8206.2009.00722.x.

[25] Goel A, Kunnumakkara AB, Aggarwal BB. Curcumin as "Curecumin": From kitchen to clinic. Biochem Pharmacol 2008;75:787–809. https://doi.org/10.1016/j.bcp.2007.08.016.

[26] Lin L, Shi Q, Nyarko AK, Bastow KF, Wu C-C, Su C-Y, et al. Antitumor Agents. 250. Design and Synthesis of New Curcumin Analogues as Potential Anti-Prostate Cancer Agents. J Med Chem 2006;49:3963–72. https://doi.org/10.1021/jm051043z.

[27] Mouslmani M, M. Rosenholm J, Prabhakar N, Peurla M, Baydoun E, Patra D. Curcumin associated poly(allylamine hydrochloride)-phosphate self-assembled hierarchically ordered nanocapsules: size dependent investigation on release and DPPH scavenging activity of curcumin. RSC Adv 2015;5:18740–50. https://doi.org/10.1039/C4RA12831A.

[28] Aggarwal BB, Harikumar KB. Potential therapeutic effects of curcumin, the anti-inflammatory agent, against neurodegenerative, cardiovascular, pulmonary, metabolic, autoimmune and neoplastic diseases. Int J Biochem Cell Biol 2009;41:40–59. https://doi.org/10.1016/j.biocel.2008.06.010.

[29] Hamaguchi T, Ono K, Yamada M. REVIEW: Curcumin and Alzheimer's Disease. CNS Neurosci Ther 2010;16:285–97. https://doi.org/10.1111/j.1755-5949.2010.00147.x.

[30] Prasad S, Tyagi AK. Curcumin and its analogues: a potential natural compound against HIV infection and AIDS. Food Funct 2015;6:3412–9. https://doi.org/10.1039/C5FO00485C.

[31] Cao J, Jia L, Zhou H-M, Liu Y, Zhong L-F. Mitochondrial and Nuclear DNA Damage Induced by Curcumin in Human Hepatoma G2 Cells. Toxicol Sci 2006;91:476–83. https://doi.org/10.1093/toxsci/kfj153.

[32] Chan W-H, Wu H-Y, Chang WH. Dosage effects of curcumin on cell death types in a human osteoblast cell line. Food Chem Toxicol 2006;44:1362–71. https://doi.org/10.1016/j.fct.2006.03.001.

[33] Jayaprakasha GK, Jagan Mohan Rao L, Sakariah KK. Improved HPLC Method for the Determination of Curcumin, Demethoxycurcumin, and Bisdemethoxycurcumin. J Agric Food Chem 2002;50:3668–72. https://doi.org/10.1021/jf025506a.

[34] Chaisiwamongkhol K, Ngamchuea K, Batchelor-McAuley C, Compton RG. Multiwalled Carbon Nanotube Modified Electrodes for the Adsorptive Stripping Voltammetric Determination and Quantification of Curcumin in Turmeric. Electroanalysis 2017;29:1049–55. https://doi.org/10.1002/elan.201600670.

[35] Kotan G, Kardaş F, Yokuş ÖA, Akyıldırım O, Saral H, Eren T, et al. A novel determination of curcumin via Ru@Au nanoparticle decorated nitrogen and sulfur-functionalized reduced graphene oxide nanomaterials. Anal Methods 2015;8:401–8. https://doi.org/10.1039/C5AY02950C.

[36] Sun X, Gao C, Cao W, Yang X, Wang E. Capillary electrophoresis with amperometric detection of curcumin in Chinese herbal medicine pretreated by solid-phase extraction. J Chromatogr A 2002;962:117–25. https://doi.org/10.1016/S0021-9673(02)00509-5.

[37] Tang B, Ma L, Wang H, Zhang G. Study on the Supramolecular Interaction of Curcumin and β-cyclodextrin by Spectrophotometry and Its Analytical Application. J Agric Food Chem 2002;50:1355–61. https://doi.org/10.1021/jf0111965.

[38] Chen X, Liang S, Zhu L, Liu J, Zhang G, Chen Z. High-sensitivity Determination of Curcumin in Human Urine Using Gemini Zwitterionic Surfactant as a Probe by Resonance Light Scattering Technique. Phytochem Anal 2012;23:456–61. https://doi.org/10.1002/pca.1380.

[39] Wang F, Huang W, Wang Y. Fluorescence enhancement effect for the determination of curcumin with yttrium(III)—curcumin—sodium dodecyl benzene sulfonate system. J Lumin 2008;128:110–6. https://doi.org/10.1016/j.jlumin.2007.05.012.

[40] Sudarsanakumar C, Thomas S, Mathew S, Arundhathi S, Raj DR, Prasanth S, et al. Selective sensing of curcumin using L-cysteine derived blue luminescent graphene quantum dots. Mater Res Bull 2019;110:32–8. https://doi.org/10.1016/j.materresbull.2018.10.014.

[41] Wu B, Liu X, Shi X, Han W, Wang C, Jiang L. Highly photoluminescent and temperature-sensitive P, N, B-co-doped carbon quantum dots and their highly sensitive recognition for curcumin. RSC Adv 2019;9:8340–9. https://doi.org/10.1039/C9RA00183B.

[42] Zhao X, Li F, Zhang Q, Li Z, Zhou Y, Yang J, et al. Mn-doped ZnS quantum dots with a 3-mercaptopropionic acid assembly as a ratiometric fluorescence probe for the determination of curcumin. RSC Adv 2015;5:21504–10. https://doi.org/10.1039/C5RA01412C.

[43] Yang H, Li X, Wang X, Chen W, Bian W, Choi MMF. Silver-doped graphite carbon nitride nanosheets as fluorescent probe for the detection of curcumin. Luminescence 2018;33:1062–9. https://doi.org/10.1002/bio.3509.

[44] Zhou D, Li D, Jing P, Zhai Y, Shen D, Qu S, et al. Conquering Aggregation-Induced Solid-State Luminescence Quenching of Carbon Dots through a Carbon Dots-Triggered Silica Gelation Process. Chem Mater 2017;29:1779–87. https://doi.org/10.1021/acs.chemmater.6b05375.

[45] Wang W, Damm C, Walter J, Nacken TJ, Peukert W. Photobleaching and stabilization of carbon nanodots produced by solvothermal synthesis. Phys Chem Chem Phys 2016;18:466–75. https://doi.org/10.1039/C5CP04942C.

[46] Nanocrystals D, Penn RL, Banþeld JF. Imperfect Oriented Attachment: Dislocation Generation in. n.d.

[47] Ma Y, Qi L, Shen W, Ma J. Selective Synthesis of Single-Crystalline Selenium Nanobelts and Nanowires in Micellar Solutions of Nonionic Surfactants. Langmuir 2005;21:6161–4. https://doi.org/10.1021/la050801l.

[48] Ann Mary KA, Unnikrishnan NV, Philip R. Ultrafast optical nonlinearity in nanostructured selenium allotropes. Chem Phys Lett 2013;588:136–40. https://doi.org/10.1016/j.cplett.2013.09.069.

[49] Todorov TK, Singh S, Bishop DM, Gunawan O, Lee YS, Gershon TS, et al. Ultrathin high band gap solar cells with improved efficiencies from the world's oldest photovoltaic material. Nat Commun 2017;8:682. https://doi.org/10.1038/s41467-017-00582-9.

[50] Andharia E, Kaloni TP, Salamo GJ, Yu S-Q, Churchill HOH, Barraza-Lopez S. Exfoliation energy, quasiparticle band structure, and excitonic properties of selenium and tellurium atomic chains. Phys Rev B 2018;98:035420. https://doi.org/10.1103/PhysRevB.98.035420.

[51] Mary KAA, Unnikrishnan NV, Philip R. Role of surface states and defects in the ultrafast nonlinear optical properties of CuS quantum dots. APL Mater 2014;2:076104. https://doi.org/10.1063/1.4886276.

[52] Khan MM, Ansari SA, Pradhan D, Han DH, Lee J, Cho MH. Defect-Induced Band Gap Narrowed CeO $_2$ Nanostructures for Visible Light Activities. Ind Eng Chem Res 2014;53:9754–63. https://doi.org/10.1021/ie500986n.

[53] Amani M, Lien D-H, Kiriya D, Xiao J, Azcatl A, Noh J, et al. Near-unity photoluminescence quantum yield in MoS2. Science 2015;350:1065–8. https://doi.org/10.1126/science.aad2114.

[54] Wang S, Meng X, Das A, Li T, Song Y, Cao T, et al. A 200-fold Quantum Yield Boost in the Photoluminescence of Silver-Doped AgxAu25−x Nanoclusters: The 13 th Silver Atom Matters. Angew Chem 2014;126:2408–12. https://doi.org/10.1002/ange.201307480.

[55] Wang H, Zhang C, Rana F. Ultrafast Dynamics of Defect-Assisted Electron–Hole Recombination in Monolayer MoS2. Nano Lett 2015;15:339–45. https://doi.org/10.1021/nl503636c.

[56] Zheng M, Xie Z, Qu D, Li D, Du P, Jing X, et al. On–Off–On Fluorescent Carbon Dot Nanosensor for Recognition of Chromium(VI) and Ascorbic Acid Based on the Inner Filter Effect. ACS Appl Mater Interfaces 2013;5:13242–7. https://doi.org/10.1021/am4042355.

[57] Yu C, Zhuang Q, Cui H, Li L, Ding Y, Lin J, et al. A Fluorescent "Turn-off" Probe for the Determination of Curcumin Using Upconvert Luminescent Carbon Dots. J Fluoresc 2020;30:1469–76. https://doi.org/10.1007/s10895-020-02590-3.

[58] Duan Z, Yin M, Zhang C, Song G, Zhao S, Yang F, et al. Polyhydric polymer-loaded pyrene composites as powerful adsorbents and fluorescent probes: highly efficient adsorption and test strips-based fluorimetric analysis of curcumin in urine and plant extracts. Analyst 2018;143:392–5. https://doi.org/10.1039/C7AN01403A.

[59] Guo Z, Zhu Z, Sun Z, Zhang X, Chen Y. Synthesis of dual-emitting (Gd,Eu)2O3-PEI@CD composite and its potential as ratiometric fluorescent sensor for curcumin. Mater Res Bull 2018;108:83–8. https://doi.org/10.1016/j.materresbull.2018.08.038.

[60] Han Z, Zhang H, He L, Pan S, Liu H, Hu X. One-pot hydrothermal synthesis of nitrogen and sulfur co-doped carbon dots and their application for sensitive detection of curcumin and temperature. Microchem J 2019;146:300–8. https://doi.org/10.1016/j.microc.2019.01.024.

[61] Zheng B, Zhang X, Peng S, McClements DJ. Impact of curcumin delivery system format on bioaccessibility: nanocrystals, nanoemulsion droplets, and natural oil bodies. Food Funct 2019;10:4339–49. https://doi.org/10.1039/C8FO02510J.

[62] Sahoo NK, Jana GC, Aktara MN, Das S, Nayim S, Patra A, et al. Carbon dots derived from lychee waste: Application for Fe3+ ions sensing in real water and multicolor cell imaging of skin melanoma cells. Mater Sci Eng C 2020;108:110429. https://doi.org/10.1016/j.msec.2019.110429.

Chapter-4

Synthesis of selenium /cellulose/polyaniline composites

Nanocomposites of conducting polymers and polymer hybrids has intrigued some major research in the recent years due to their enhanced mechanical and electrochemical properties. Among them, cellulose/polyaniline hybrids stand out due to their environmental stability, ease of synthesis, biodegradability etc. Herein, we studied one pot, in-situ polymerization of Se/cellulose/polyaniline hybrid nanocomposite. The structural and morphological understanding of the composites were achieved from XRD, FTIR, SEM, TEM, XPS and RAMAN spectroscopy. HRTEM images revealed that selenium exists in trigonal QD structure in the matrix. The three-dimensional (3D) fibrous network morphology of Se/cellulose/polyaniline is advantageous for surface-oriented applications like energy storage or catalysis.

4.1. INTRODUCTION

Conducting polymers have always been a topic of research interest due to their potential applications in energy storage devices, electromagnetic interference shielding, photovoltaic devices and sensors. They are often easy to scale into large area devices with tunable energy gaps and ionization potentials. Among widely known conducting polymers, polyaniline (PANI) is intensively studied owing to its low cost, low density, environmental and thermal stability, hassle-free synthesis, wider range of working potential window and tunable conductivity. Being a conjugated conducting polymer, the conductivity of polyaniline is a result of redox (oxidation-reduction) reactions. Furthermore, its ability to switch between different oxidation states (emeraldine, leucoemeraldine, and pernigraniline) under varying electrochemical conditions makes PANI a prime candidate for applications in energy storage and electrochemical sensors. However, these materials often suffer from capacitance fading due to swelling/shrinkage of the polymer backbone with repetitive doping/de-doping cycles[1]. Synthesis of various PANI composite, binary and even ternary composite electrodes were found to circumvent such stability and energy density issues[2,3]. Prior reports for synthesis of PANI composite materials for improved storage capabilities include doping with ions such as Zn^{2+}, Cu^{2+} and Fe^{3+}, binary transition metal oxides like Ni-Co oxides and similar metal-oxide-frameworks (MOFs)[4–8]. Carbonaceous materials like graphene[9–12], carbon nanotubes (CNTs)[3,13], porus carbon[14], graphene oxide (GO)[15] etc possessing high surface area are also integrated with PANI and comprehensively studied as an

electrode material for electrochemical studies. The cellulose/PANI hybrid composite has high porosity, flexibility and stability, which can be easily incorporated or bound with conducting polymers to enhance storage capabilities[16,17]. Liu et.al recently reported polyaniline/cellulose nanofibril, where Fe^{3+} ions effectively crosslinked the chains for improved supercapacitor performance[18]. However, low areal capacitance associated with these carbonaceous cellulose materials mandates a larger area to store the intended energy capacity even upon composite formation[19]. This can be disadvantageous for micro-device applications and hinder the size reduction of devices. The fine balance between good capacitance and low loading has to be achieved to ensure the flexibility and less weight of the material [20]. Transformative advances in the field can be attained through a synergistic combination of transition metals, transition metal chalcogenides or chalcogenides. Barik et.al recently elaborated the effect of Se when inserted into WO_3 matrix in the electrochemical performance of the composite[21]. Se insertions into various other metal oxides have also reportedly amplified the conductivity of the material for application in fuel cells[22], solar cells[23], photocatalysis[24]. We studied Se/cellulose/polyaniline composites prepared through a room temperature mediated polymerization route followed by freeze drying.

4.1.1. Nanocomposite of polyaniline with selenium

Out of all the known elemental counterparts, chalcogen elements like selenium plays an inevitable role in nanomaterial-based devices due to its unique and superior electrical, optical and thermal properties. Though some research has

been conducted on Se-polyaniline composite material to discover applications in energy storage, medical, thermoelectric, electrical and opto-electronic devices, reports on the detailed effects of integration of Se into polyaniline are scarce. A recent review by A K Yadav et.al., gives a comprehensive understanding of synthesis, structure, properties and effects of chalcogen/chalcogenide doped PANI composites[25]. Nanocomposites of Se with conducting polymer like PANI are generally synthesized via in-situ polymerization of aniline in the presence of Se NPs or simple mixing of Se NPs with PANI structures. The choice of synthesis route also dictates the structural, electrical and optical properties of the final material. Shumaila et al. synthesized Se/PANI nanocomposites by mixing Se nanowires synthesized from SeO_2, in the presence of β-cyclodextrin and vitamin C which was then mixed with PANI EB[26]. The ex-situ synthesized composite exhibited nearly five-fold increase in its electrical conductivity upon doping with Se. Another work by E. Ozkazanc et.al., describes the formation of Se/PANI composites through in-situ chemical oxidation of aniline with Se added to the mixture during polymerization[27]. The FTIR spectra in the work suggested plausible electrostatic interaction between Se and nitrogen atoms of PANI leading to the formation of the composites. Se/PANI composites are also synthesized to act as precursor for Se for the fabrication of metal selenide/PANI composite. P K Khanna et.al., had demonstrated the use of pre-synthesized Se/PPy composite as precursor for CdSe/PPy composite using chemical and microwave methods and used it for the detection of mercury ions (Hg^{2+}) using UV-Visible absorption spectroscopy[28]. The morphology of Se within the composite was also found to

play a vital role in the material property. One dimensional Se structures were found to facilitate effective conductive pathways due to the movement of delocalized electrons within the polymer chain. This enhanced property of 1D Se structure is notable in the work of Zhang et.al, where graphene sheet encapsulated one dimensional Se-PANI core-shell nanowires was reported for battery application[29]. The material showed enhanced cycling performance and high-rate capability with a reversible discharge capacity of 567.1 mA h/g at 0.2 C after 200^{th} cycle and 510.9 mA h/g at 2 C. A similar composite was also used by Lei et.al, for high capacitance aluminium-selenium batteries[30].

4.1.2. Nanocomposite of polyaniline with cellulose

Cellulose $(C_6H_{10}O_5)_n$ is one of the most abundant polymers that is primarily known for its biocompatibility, hydrophilic nature, easy functionalization, low weight, thermal and mechanical properties. It is often available in various forms like cellulose nanocrystals (CNCs), cellulose nanofibers (CNFs), cellulose nanowhiskers (CNWs), bacterial cellulose (BC) and microcrystalline cellulose (MCC). These various forms are extracted from lignocellulosic biomass via different physico-chemical, microbial and enzymatic routes. The bulk hydroxyl groups in cellulose backbone allows easy functionalization of the polymer and integration with other polymers. Cellulose-polymer blends have received considerable attention with many works focused on integrating cellulose with polymers like polypyrrole, polyaniline, epoxy etc. Cellulose-PANI blends have been the most alluring among them as the composite retains the electrical conductivity of PANI while having exceptional thermal and

mechanical properties. The secondary forces between the hydroxyl bonds of cellulose and amine groups of aniline ensures homogenous formation of the composite. Their improved adsorbing and conductive properties are widely exploited in energy storage application, biosensors, electromagnetic shielding applications, water treatment etc.

Cellulose-PANI composites have been widely exploited for dye adsorption against both acidic and basic dyes. While maximum adsorption was observed at lower pH for anionic dyes, basic/neutral gave maximum adsorption for cationic dyes[31,32]. The adsorbant composite has also been effective in heavy metal removal including Cr(IV)[33], Cu(II)[34], Hg(II)[35], Pb(II)[36] etc. For example, in a recent report by Dewa et.al., MCC functionalized with PANI was found to be an effective adsorbent in Cr(IV) ion removal at neutral pH[37]. Doping of metal/metal oxide/metal nitrate NPs into nanocellulose-PANI composite have also been instrumental in monitoring bio-signals and even as antibacterial materials. Cheng et.al, recently reported regenerated CNFs with PANI@Ag NPs as catalyst/bactericide for water decontamination[38]. The sensing capabilities of PANI is often elevated with the introduction of cellulose and these materials are widely used in humidity sensors[39], gas sensors like CO_2 sensors[40], ammonia sensors[41], LPG sensors[42] and other vapor sensors. Another area of interests for cellulose-PANI composites is electromagnetic shielding where the shielding efficiencies of polyaniline is supported by the lightweight cellulose matrix. Gopakumar et.al, describes the use of CNF-PANI papers to attenuate microwave radiations in the X-band with an average shielding

effectiveness of ca. −23 dB (>99% attenuation) at 8.2 GHz with 1 mm paper thickness via absorption mechanism[43]. A recent review by Rana et.al, also summarizes the application of cellulose-PANI composite as electrode material for energy storage applications[32]. While polyaniline imparts electrical conductivity to the composite, cellulose matrix offers good mechanical stability to the electrode material favoring longer cyclic stability with each round of charge-discharge.

4.1.3. Chemical oxidative polymerisation

Chemical oxidative polymerization of aniline, a key method for polyaniline synthesis, is particularly notable for its simplicity and scalability. This process involves the chemical oxidation of aniline monomer in an acidic medium, typically using oxidants like ammonium persulfate (APS) or hydrogen peroxide, leading to the formation of polyaniline through a series of complex reaction pathways. The reaction commences with the protonation of aniline in an acidic medium, forming an anilinium ion. The oxidant, commonly APS, oxidizes the aniline monomers to generate aniline radicals. These radicals couple to form dimeric intermediates, which further react to form oligomers and eventually high molecular weight polyaniline. The entire process is highly dependent on several factors, including the concentration of aniline and the oxidant, the type of acid used, the temperature, and the reaction time[44]. Recent studies have demonstrated that by fine-tuning these parameters, one can effectively control the molecular weight, conductivity and morphology of the resultant polyaniline. For instance, varying the concentration ratios of aniline to APS was found to alter the

extend of oxidation, impacting the polymer's conductivity and structural integrity[45]. Similarly, adjusting the acidity of the reaction medium has been shown to influence the doping level of PANI, thereby modifying its electrochemical properties

The chemical oxidative polymerization route allows for the synthesis of polyaniline in various morphological forms, including nanofibers, nanotubes, and nanoparticles, each with distinct properties and applications. Recent advancements in this field have provided deeper insights into the mechanistic and structural nuances of polyaniline synthesis, leading to enhanced control over the polymer's properties and potential applications.

4.1.4. Lyophilization

Freeze drying or lyophilization is often used as a drying technique mostly to remove organics from the sample. In this method, the sol-gel mixture is first frozen after which the solvent is sublimated under low pressure, thereby bypassing the liquid phase. The capillary forces that act on the solvent is hence absent causing minimal shrinkage and cracking in the final material. It is generally used for sensitive gels that collapse easily upon supercritical drying. The method is also employed to generate an ideal 3D template with enhanced porosity while maintaining the chemical and mechanical properties of the matrix. This elevated porosity aids in better adhesion and increased active sites for the nanomaterial in the host. Such mesoporous structure with least obstructed channels facilitates the easy transport of charge through the electrolyte resulting in better supercapacitor applications. Moreover, the temperature regime of PANI preparation was found

to have a direct correlation with the temperature dependent electrical conductivity of PANI with PANI exhibiting high orders of conductivity, at low temperatures[46]. Wu et.al reported a nickel-cobalt layered double hydroxide loaded on a freeze-dried polyaniline/bacterial cellulose electrode with excellent electrochemical and mechanical properties[47]. Electrode materials with enhanced surface area based on iron doped polyaniline (Fe-PANI) prepared by freeze drying was also reported recently[48]. The synthetic procedure was used by Zhe-Fei Li et al to reduce the re-stacking of graphene in G-PANI nanocomposites while enhancing the electrochemical active surface area[11].

4.2. EXPERIMENTAL SECTION

4.2.1. Materials

Ammonium persulfate [$(NH_4)_2S_2O_8$, (APS)] and aniline hydrochloride ($C_6H_5NH_2 \cdot HCl$) and analytical reagent grade hydrochloric (HCl) acid was purchased from commercial sources. Selenous acid (H_2SeO_3, 98%), cellulose (microcrystalline, powder) and *N*-Methyl-2-pyrrolidone [anhydrous, 99.5% (NMP)] were procured from Sigma-Aldrich. All the reagents were analytical-grade and used as supplied without further purification. Distilled water (DW) obtained from Merck Chemicals was used throughout the experiment.

4.2.2. Apparatus and characterization

Powder X-ray Diffractometer (Aeris Research, PANalytical, Netherlands) with a scanning range of 2θ =10° to 90° with Cu K_α radiation (λ=1.540598 Å) was used to obtain the X-ray diffractogram from the samples.

The room temperature Fourier Transform Infared (FTIR) spectrum in the region 400-4000 cm^{-1} was obtained from FTIR spectrometer (Perkin Elmer). The morphology and microstructure of the samples were evaluated by images from a TESCAN and Bruker make MIRA3 LM Field Emission Scanning Electron Microscope (FESEM) with EDS mapping of the elements and JEOL 2100 Plus Transmission Electron Microscope (TEM). The X-ray Photoelectric Spectroscopy (XPS) were performed on a Thermo Scientific K-Alpha X-ray Photoelectron Spectrometer system. The Diffuse Reflectance Spectra (DRS) of the samples were recorded on a Shimadzu UV-Vis-NIR spectrophotometer-UV 2600. The characteristic scattering of the samples was recorded on a Horiba Scientific Confocal Raman Microscope at a laser excitation wavelength of 532 nm. Thermogravimetric analyses (TGA) were performed on a NETZSCH thermogravimetric analyser from RT-800 °C at a rate of 10 K/min. The specific Brunauer-Emmett-Teller (BET) surface area was estimated from N_2 adsorption-desorption test using a BELSORP MAX analyser. The surface area and pore size distribution were calculated using Brunauer−Emmett−Teller (BET) and the Barrett−Joyner−Halenda (BJH) methods respectively.

4.2.3. Synthesis of PANI, Se-PANI, Cel-PANI, Se-Cel-PANI composites

Polyaniline was prepared via one-pot polymerization of aniline hydrochloride following an earlier chemical method with slight variations in the reaction conditions[49]. In a typical synthesis, 4.15 g ammonium persulphate (APS) is added to 50 ml of 1 M HCl solution and mixed well. This solution was then slowly added in drop-wise manner into a beaker containing aniline

hydrochloride (2.05 g) dissolved in 50 ml of 1M HCl solution under continuous stirring. The oxidant to monomer ratio was kept at 1.15:1. This pitch-dark green reaction mixture was kept undisturbed in the dark at room temperature for 36 hrs. The obtained green precipitate was filtered, washed several times with DW and ethanol to remove the by-products, excess acids and unpolymerised species. The slurry like mixture was kept in a cold press at -120 °C for 1 hour and then freeze dried at -70 °C for 1 day to obtain bright dark green powders. To prepare Se-PANI, Cel-PANI and Se-Cel-PANI composite, in addition to APS solution, 1 ml aqueous solution of selenous acid or/and 0.5 g microcrystalline cellulose (MCC) powders was added to aniline hydrochloride, during the polymerization process. The molar ratio of monomer to Se precurssor was kept at 2:1.

4.3. RESULTS AND DISCUSSION

4.3.1. Powder X-Ray Diffraction (p-XRD)

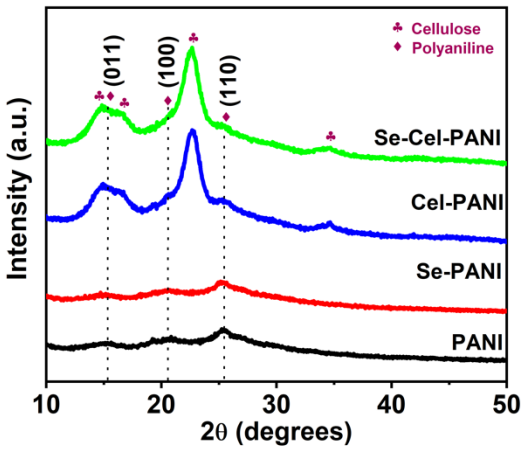

Figure 4.1. Powder-XRD pattern of PANI, Se-PANI, Cel-PANI and Se-Cel-PANI composites

Figure 4.1 displays the p-XRD pattern of PANI, Se-PANI, Cel-PANI and Se-Cel-PANI composites. The XRD pattern of pristine PANI shows peaks at $2\theta \approx 15.3°$, 20.84° and 25.23° corresponds to (011), (100), and (110) reflections from the emeraldine salt form of polyaniline[50]. The characteristic peaks at 15.3°, 20.8° and 25.2° can be attributed to the repeated units of the polymer chain and periodic channels perpendicular to the principal polymer backbone and the periodic arrays parallel to the polyaniline chain respectively[51]. The X-ray diffractograms of Cel-PANI composite shows peaks at 14.9°, 16.7°, 22.6° and 34.5° corresponding to reflections from $(1\bar{1}0)$, (110), (200) and (004) crystallographic planes respectively of semicrystalline cellulose structure in addition to diffraction peaks of PANI[52]. This is consistent with the XRD pattern of microcrystalline cellulose reported. No diffraction peaks from crystalline selenium are observed in the XRD pattern of the Se-PANI or Se-Cel-PANI composite. Absence of any shift in diffraction peaks of PANI and MCC suggests formation of hybrid composites of polyaniline and MCC through hydrogen bonding.

4.3.2. Fourier Transform Infrared (FTIR) spectra

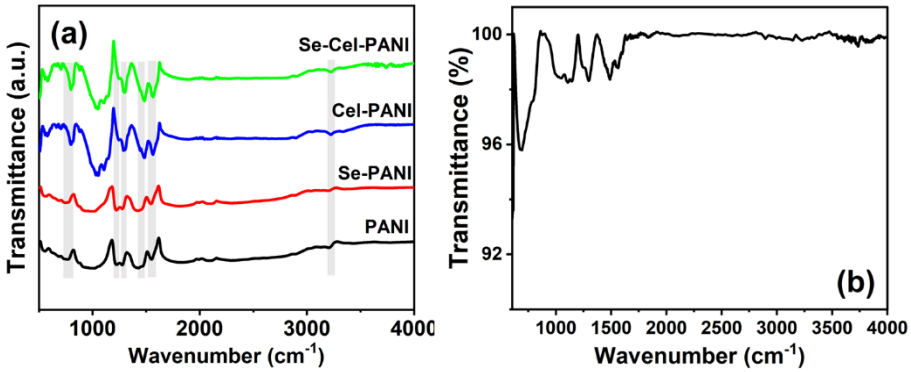

Figure 4.2. (a)FTIR spectra of PANI, Se-PANI, Cel-PANI and Se-Cel-PANI composites (b) FTIR spectra of Se-Cel-PANI composite after one year of storage

The chemical structures of the composites were evaluated from the FTIR spectra (**Figure 4.2(a)**). The FTIR spectra of all the composites PANI, Se-PANI, Cel-PANI and Se-Cel-PANI exhibits the characteristics peaks of virgin PANI. The main absorption bands at 770, 1014, 1220, 1278, 1428 and 1550 cm^{-1} corresponds to the emeraldine salt form of PANI[53]. The band peaked at 1278 cm^{-1} can be attributed to the stretching of C–N bonds of the second aromatic amines while the band corresponding to stretching of the $C–N^{+}$ polaron structure is observed at 1220 cm^{-1}. The absorption centered at 1014 cm^{-1} is dedicated to the presence of protonated imine group on the polyaniline backbone chain[54]. The band peaked at 770 cm^{-1} corresponds to C-H out of plane bending and aromatic ring deformations[55]. The weak band observed in the spectrum centered at 3202 cm^{-1} is due to the -NH stretching vibrations[56]. The characteristic stretching bands at 1550 $cm^{-1}$and 1428 cm^{-1} represents the C=C vibrations of the quinoid

and benzenoid rings of polyaniline respectively[43]. Compared to PANI, the intensity of band at 1428 cm^{-1} is higher in Se-PANI suggesting a greater number of benzenoid units. For Cel-PANI and Se-Cel PANI composites intensity of band due to benzenoid rings is reduced. This is due to the conversion of benzenoid units to quinoid units upon addition of cellulose. The absence of any prominent broad peaks at around 3400 cm^{-1} corresponding to the hydroxyl bonds of cellulose in Cel-PANI suggests that the –OH bonds of cellulose are consumed by the amine groups of PANI during the formation of the composite[57]. The FTIR spectrum of Se-PANI and Se-Cel PANI composite resembles the spectrum obtained for pristine PANI with minor shifts of the bands peaked at 770 cm^{-1} and 1014 cm^{-1} of PANI. This can be attributed to the interaction of Se with the aromatic ring and imine groups of the polymer.

Generally, MCC is hygroscopic owing to its large surface-to-volume ratio and presence of abundant -OH groups in the material. For device applications, MCC composites often face challenges due to moisture absorption with time. The FTIR spectra of Se-Cel-PANI composite after 1 year of storage is given in **Figure 4.2 (b)**. The band showing the presence of hydroxyl bond (at ~3400 cm^{-1}) in the composite is absent indicating negligible water content in the material even after one year of storage.

4.3.3. Scanning Electron Micrograph (SEM) images & EDS mapping

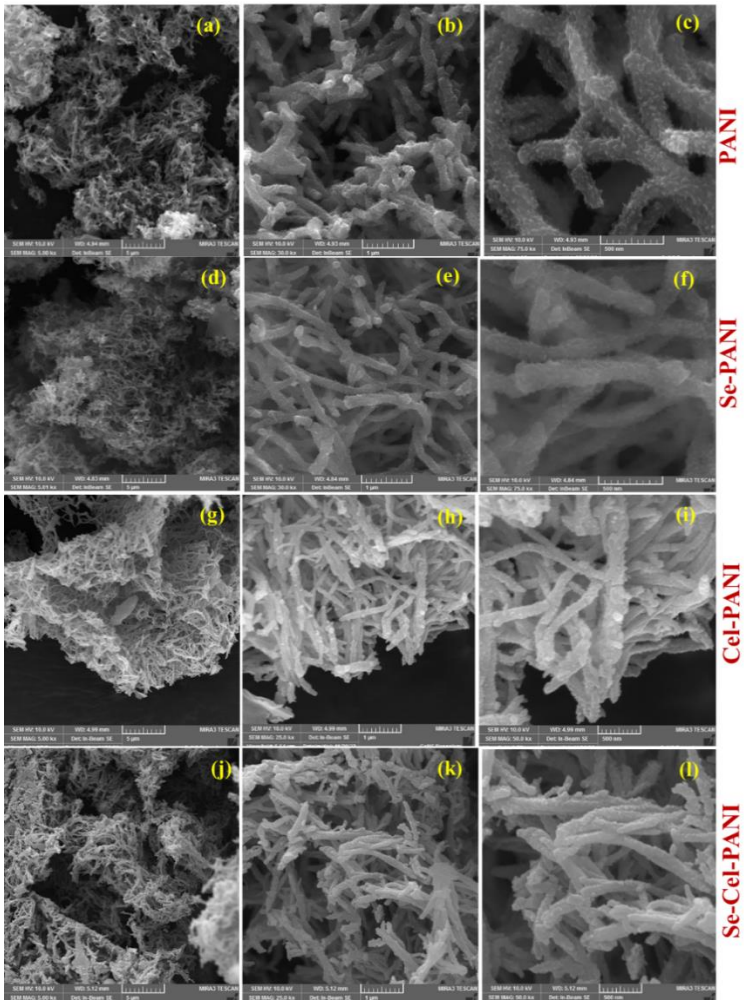

Figure 4.3. SEM image of (a-c) PANI (d-f) Se-PANI (g-i) Cel-PANI (j-l) Se-Cel-PANI composites

The scanning electron microscopy (SEM) images of the PANI, Se-PANI, Cel-PANI and Se-Cel-PANI composite is given in **Figure 4.3(a-c), 4.3(d-**

f) 4.3(g-i) and **4.3(j-l)** respectively. The surface morphology and microstructure of all composites shows a similar intertwined network in porous framework. PANI composite exhibited short, thick fibrillar morphology with a heavily scaled external surface with an approximate average diameter of about 175 nm (**Figure 4.3(c)**). For Se-PANI shown in **Figure 4.3(f)**, the fibres exhibited similar external surface with an average diameter of about 160 nm. After the introduction of cellulose in the polyaniline matrix, there occurs bumps and nodules on the surface of the Cel-PANI (**Figure 4.3(i)**). The fibres appear slightly longer with average diameter being 140 nm. The Fe-SEM images of the Se-Cel-PANI composite given in (**Figure 4.3(l)**) also reveals fibrillar morphology having average diameter of 120 nm and bumps on its surface. PANI produced by oxidative aniline polymerization usually form a nanofibrous structure followed by an irregular secondary growth and aggregation. The fibers in the composites are fused at more than one point forming a sponge-like surface. The presence of microcrystalline cellulose and Se gives active sites for chemical polymerization of PANI nanofibers and prevents tendency to aggregate[58]. Thus, hydrophilic PANI composite fibers formed spreads into aqueous phase and grow slender and faster. Consequently, nanofibers have the maximum diameter for PANI and Se-Cel-PANI have uniform longer nanofibers with smallest diameter. Moreover, Se is evenly anchored on the PANI surface, enables fast ion diffusion and strong interfacial charge transfer for superior electrochemical properties.

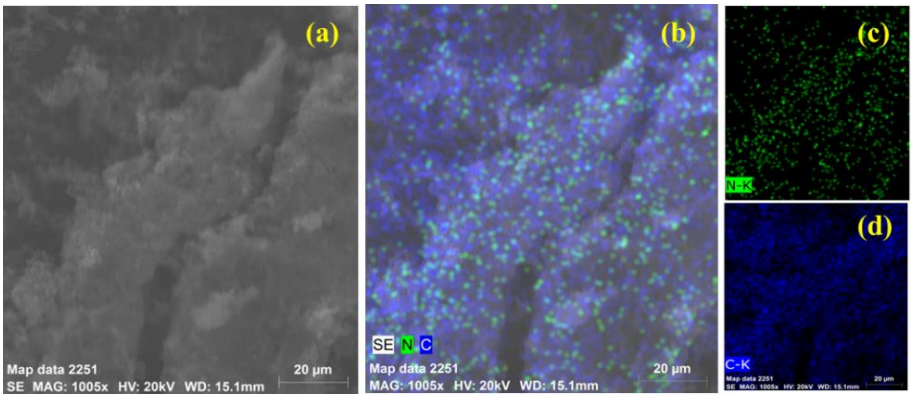

Figure 4.4. (a) SEM image and (b) EDX mapping of PANI composite, (c-d) differential elemental distribution for an area shown in image (a)

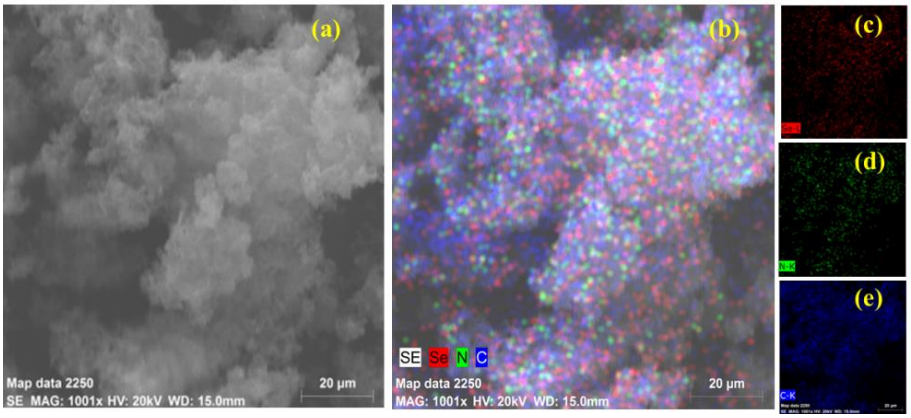

Figure 4.5. (a) SEM image and (b) EDX mapping of Se-PANI composite, (c-e) differential elemental distribution for an area shown in image (a)

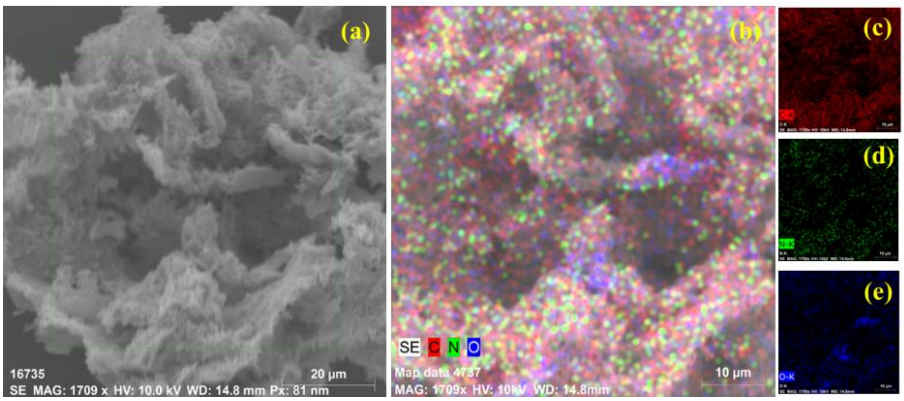

Figure 4.6. (a) SEM image and (b) EDX mapping of Cel-PANI composite, (c-e) differential elemental distribution for an area shown in image (a)

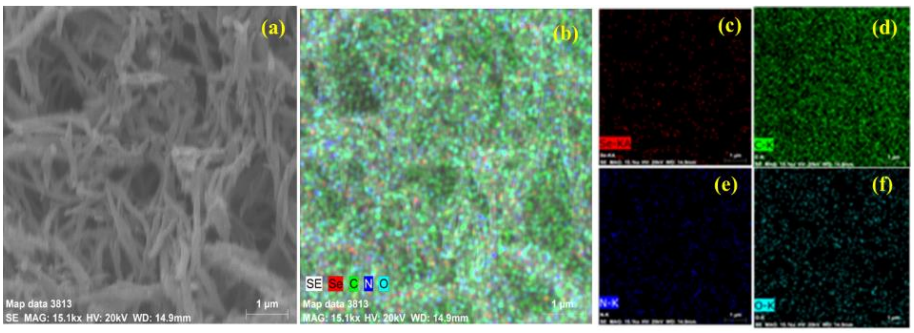

Figure 4.7. (a) SEM image and (b) EDX mapping of Se-Cel-PANI composite, (c-f) differential elemental distribution for an area shown in image (a)

The EDX mapping of the composites PANI, Se-PANI, Cel-PANI and Se-Cel-PANI is shown in **Figure 4.4, 4.5, 4.6, 4.7** respectively. The differentiated distribution of elements present in the composite is also given in the images accompanying the corresponding figures. The differential EDX mapping in **Figure 4.4(c,d)** corresponds to C and N of PANI chains. **Figure 4.5(c)** clearly indicates that Se has been well incorporated into the composite in addition to C

and N of PANI chains. The introduction of cellulose into the matrix have evidently contributed O into the elemental distribution of Cel-PANI and Se-Cel-PANI (**Figure 4.6 and 4.7**). All the elements present in the composite is found to have been uniformly distributed throughout the morphology. For Se containing composites, the differential distribution of the elements clearly indicates that Se has also been decorated uniformly throughout the composite. Additionally, the elemental mapping of pure PANI, Se-PANI and Se-Cel-PANI depicts that the composites do not contain impurity elements. The spatial and surface distribution of the constituent elements in the matrix gives a better perspective regarding the interaction of elements within the composite.

4.3.4. Transmission Electron Micrograph (TEM), High Resolution Transmission Electron Micrograph (HR-TEM) images

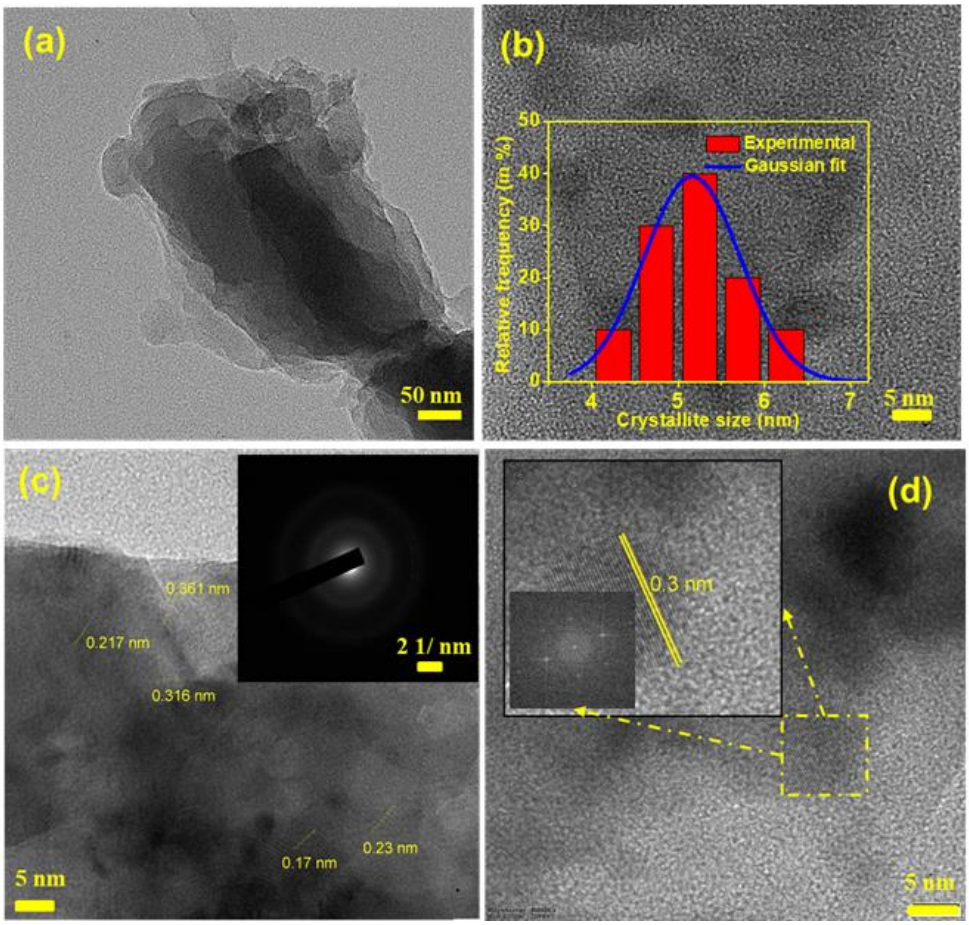

Figure 4.8. (a)TEM image (b) HRTEM image of Se-Cel-PANI composite; inset of figure shows the particle size distribution (c) HRTEM image showing the lattice fringes corresponding to lattice planes of trigonal Se; inset shows the SAED pattern observed for the composite (d) HRTEM image showing the lattice spacing of 0.3 nm corresponding to (101 plane) of trigonal Se (shown in inset); FFT image of the corresponding lattice fringes which confirms to hexagonal structure of Se (given in inset of inset).

The microstructure of Se-Cel-PANI composite was better understood by TEM, HRTEM images. **Figure 4.8(a)** shows that the Se-Cel-PANI composite fibers measured an average diameter of 115 nm, consistent with the SEM data. On close examination, quasi-spherical dark regions amidst agglomeration were observed in the HRTEM image shown in **Figure 4.8(b)**. These can be attributed to the presence of selenium in the composite. The **inset of Figure 4.8(b)** shows the particle size distribution as obtained from the HRTEM image. The particle sizes ranges from 4 to 6.5 nm. The HRTEM image of Se-Cel-PANI given in **Figure 4.8(c)** shows randomly oriented crystallites with interplanar spacing of 0.36, 0.31, 0.23, 0.21 and 0.17 nm. These d-spacing values can be indexed to (010), (101), (110), (102) and (201) planes of trigonal Se[59]. The **inset of Figure 4.8(c)** gives the selected area diffraction pattern of the composite. The concentric rings observed in the image implies the polycrystalline nature of the sample. The HRTEM image showing a set of lattice fringes corresponding to the d-spacing 0.3 nm is given in **Figure 4.8(d)**. This corresponds to the (101) plane of trigonal selenium species. The bottom left **inset of Figure 4.8(d)** shows the fast Fourier transform image obtained for the lattice fringes observed. The bright spots obtained in the FFT image directly correlates with the hexagonal structure of Se in the composite.

4.3.5. X-ray Photoelectron Spectra (XPS)

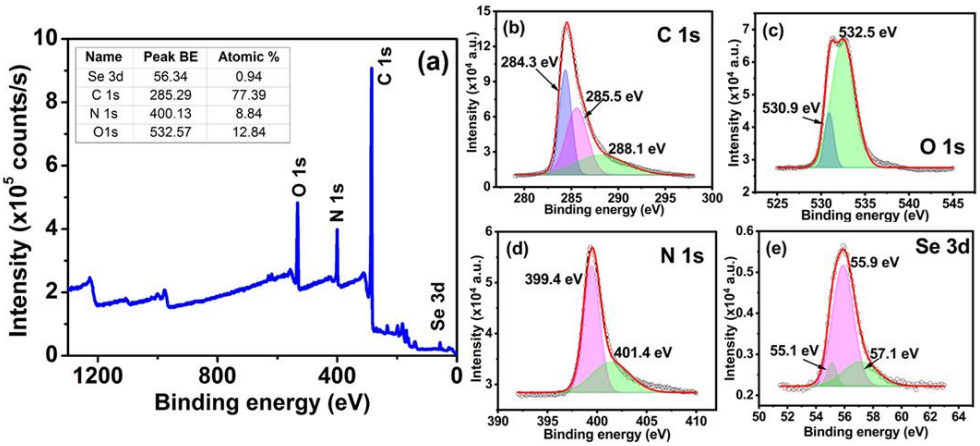

Figure 4.9. (a) Survey spectrum scan of elements; inset shows table containing the peak binding energy (in eV) and the % atomic composition of elements (b) C 1s (c) O 1s (d) N 1s and (e) Se 3d elemental X-ray photoelectron spectroscopy spectra of Se-Cel-PANI composites

The XPS analysis of Se-Cel-PANI composite was done to confirm the chemical bonding and elemental valence. **Figure 4.9(a)** shows the survey scan spectrum of Se-Cel-PANI composite with typical peaks corresponding to C 1s, N 1s, O 1s and Se 3d. The signal intensity for Se indicates the presence of elemental selenium in the composite. The **inset of Figure 4.9(a)** shows the peak binding energy (in eV) and the % atomic composition of the element detected in Se-Cel-PANI composite. **Figure 4.9(b-e)** represents the elemental point scan of C 1s, O 1s, N 1s and Se 3d species respectively. These core spectra were deconvoluted using Gaussian fitting method. The C 1s spectra shown in **Figure 4.9(b)** was deconvoluted to three distinct peaks corresponding to three types of carbon functional groups. The intense peak at 284.3 eV can be due to the presence of

non-oxygenated carbon, generally C-C bonds, while the peaks at 285.5 and 288.1 eV can be attributed to C-O/C-Se bonds and C=O bond respectively[60]. The comparative oxygen O 1s spectrum (**Figure 4.9(c)**) illustrates the presence of peaks due to C-O and C=O bonds centered at 532.5 eV and 530.9 eV respectively[60]. The core N 1s spectrum (**Figure 4.9(d)**) of Se-Cel-PANI composite consists of two subpeaks at 399.4 eV and 401.4 eV corresponding to the benzenoid amine and the diminished nitrogen cationic radical ($N^{+\bullet}$). The absence of peak corresponding to imine groups (at ~398 eV) indicates that these groups have been completely doped[61]. It ensures high conductivity of Se-Cel-PANI composite. The presence of these nitrogen species also reveals that PANI present in the ternary composite is in the protonated state[62]. The Se 3d spectra (**Figure 4.9(e)**) consists of two sub peaks at 55.1 eV and 55.9 eV which corresponds to Se $3d_{5/2}$ and Se $3d_{3/2}$ orbitals respectively for Se [Se(0)] which are separated by 0.8 eV. A sub peak at binding energy of 57.1 eV can be indicative of interaction of Se with C/O [Se(IV)] ie, Se-C/Se-O[63]. This confirms that Se has definitely interacted with carbon in the matrix which is also consistent with the FTIR results.

4.3.6. UV-Visible Absorption Spectra

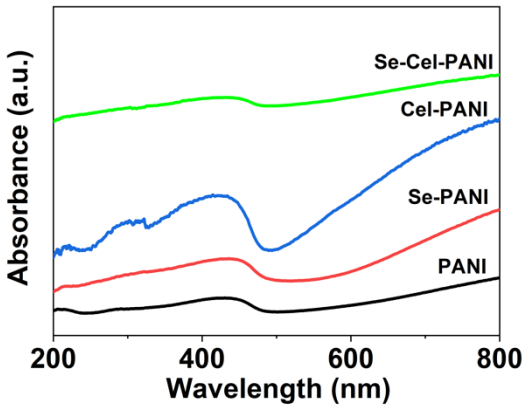

Figure 4.10. UV-Visible absorption spectra of PANI, Se-PANI, Cel-PANI and Se-Cel-PANI composites

Solid state absorption spectra of PANI, Se-PANI, Cel-PANI and Se-Cel-PANI composites are shown in **Figure 4.10**. The peak around 435 nm can be assigned to the polaron−π* transitions while the broad shoulder below 400 nm is due to π−π* transition of benzenoid rings in PANI chains[64]. Another free tail extending to the IR region is due to the π−polaron transition of the chains[65]. Presence of such localized polaronic states confirms the formation of doped emeraldine salt form of polyaniline. The UV-visible absorption spectra of PANI composites also show similar spectral peaks. This confirms in-situ development of PANI - cellulose hybrid.

4.3.7. RAMAN Spectra

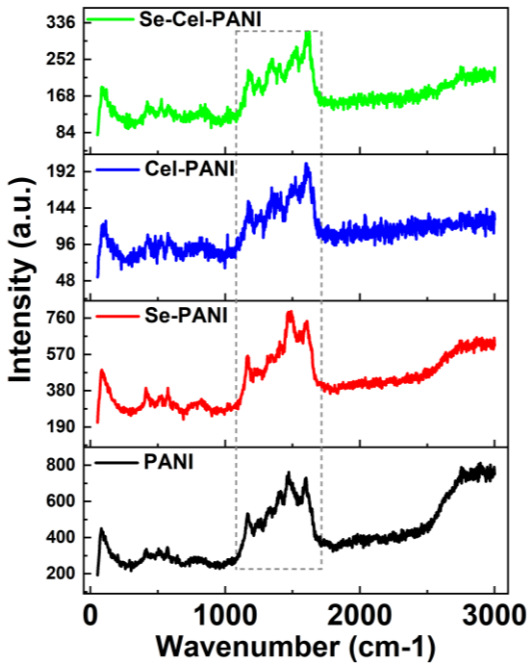

Figure 4.11. RAMAN spectra of PANI, Se-PANI, Cel-PANI and Se-Cel-PANI composites

The interracial interaction between the constituents of the composite can be effectively studied using Raman spectroscopy (**Figure 4.11**). For virgin PANI sample, the spectral peak observed at 1600 cm^{-1}, 1409 cm^{-1} and 1471 cm^{-1} can be attribute to the C-C stretching vibrations of benzenoid, C-C stretching vibrations of quinoid and C=N vibrations of the quinoid rings respectively[66,67]. The C-H bending vibrations of benzene/quinoid rings and in plane ring deformations are observed at 1263 and 1164 cm^{-1} respectively. The $C–N^{+}$ stretching vibration of PANI is recorded at 1334 cm^{-1} [67]. The Raman spectrum of Cel-PANI

composites displayed characteristic peaks similar to pristine PANI. Moreover, decrease in intensity of quinoid vibration band at 1471 cm^{-1} compared to stretching vibrations of benzenoid suggests conversion quinoid to benzenoid in cellulose composites.

4.3.8. Thermo-gravimetric analysis (TGA)

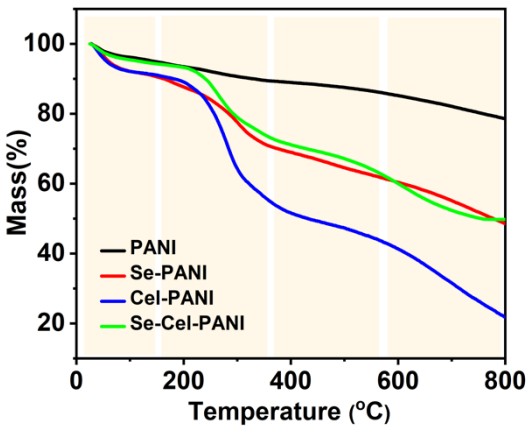

Figure 4.12. Thermogravimetric analysis (TGA) spectra of PANI, Se-PANI, Cel-PANI and Se-Cel-PANI composites.

Figure 4.12 gives the TGA curves of PANI, Se-PANI, Cel-PANI and Se-Cel-PANI composites divided into four regions. From room temperature to about 150 °C, the loss in moisture accounted for a small fraction of weight loss in all samples[58]. The second stage of weight loss occurs from a temperature 200 C to 350 °C due to the decomposition of cellulose in the matrix and removal of acid components in the composite[68]. PANI remains almost stable and loss of weight is due to the removal of acid components. The composite Se-PANI also

exhibits considerable weight loss due to the decomposition of selenium from the composite. The maximum weight loss for cellulose composites happens in this stage of thermal degradation. Noticeably, the presence of Se enhances the thermal stability of Se-Cel-PANI at this stage of degradation. The final stage of thermal degradation in the samples is from about 350 °C to 680 °C is ascribed to the breaking down of the polymer backbone[58,69]. Finally, 80%, 50%, 50%, 20% of residue remained after heating to 800 ^{o}C for PANI, Se-PANI, Se-Cel-PANI and Cel-PANI respectively. The results suggest that compared to the Cel-PANI, the thermal stability of the Se-Cel-PANI has been enhanced due to the interaction between Se with Cel-PANI.

4.3.9. Brunauer-Emmett-Teller (BET) analysis

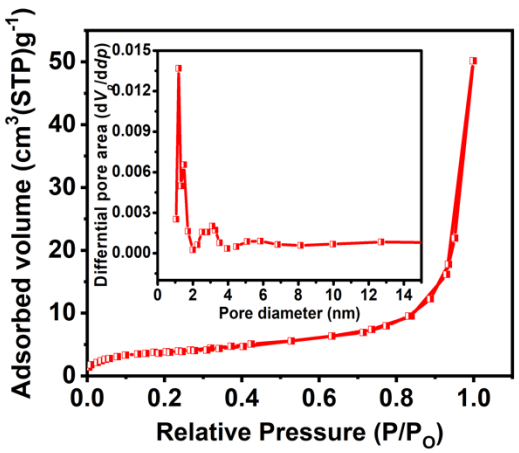

Figure 4.13 Brunauer-Emmett-Teller (BET) surface area of Se-Cel-PANI. The inset of figure shows the pore size distribution in the composite.

N_2 adsorption-desorption test was used to study the specific surface area of Se-Cel-PANI composite. The isotherm showed in **Figure 4.13** is a type IV

isotherm which is characteristic of mesoporous materials (materials with pore size from 2 to 50 nm). The specific surface area of Se-Cel-PANI was found to be approximately 14.5 m^2/g and the composite possess a pore size of 19.56 nm. This value of specific surface area is sufficiently conducive for better percolation of ions to/from the electrolyte used during electrochemical energy storage thereby leading to enhanced capacitance values.

4.3.10. Mechanism of formation of ternary Se-Cellulose-Polyaniline composite

A plausible scheme of formation of the ternary Se-Cellulose-Polyaniline composite from its constituent entities is given below in **Scheme 4.1**. Aniline hydrochloride gets homogenously dispersed over the microcrystalline cellulose during the initial stages of synthesis. Aniline monomers are adhered on crystallite sites of MCC through the hydrogen bonding between the amine groups of aniline and the hydroxyl entities of cellulose. Upon the addition of APS, the polymerization is initiated, thereby resulting longer fibres due to larger number of specific sites with aniline monomers. Selenium could anchor on the Cel-PANI composite to crystallize in trigonal form and gets decorated homogeneously throughout the composite. The end product is a pitch-dark green powder composite of Se-Cellulose-Polyaniline with excellent conductivity and electrochemical performance. In the absence of cellulose, the repeated units of PANI formed by secondary polymerization gets accumulated on the surface of the already formed fibres resulting in a bulky morphology. However, cellulose

provides an increased surface for PANI to polymerise and prevent the over-stacking of the fibres.

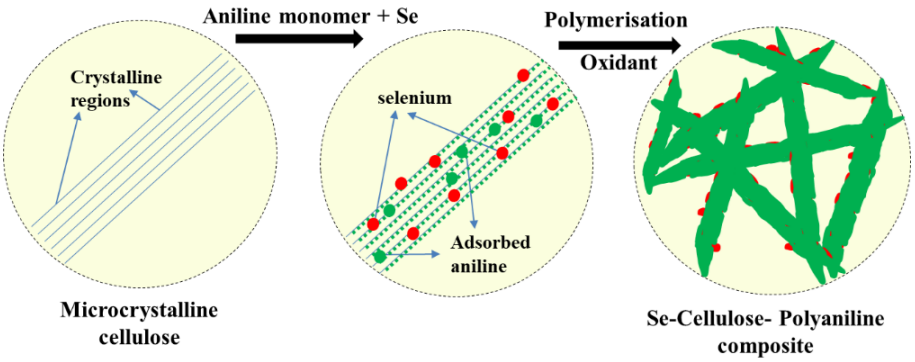

Scheme 4.1. A scheme showing the formation of a stable PANI onto cellulose decorated with selenium

4.4. CONCLUSION

Selenium /Cellulose/Polyaniline nanocomposites were synthesized using freeze drying assisted one pot polymerization of aniline. The work emphasis chemical oxidative polymerization followed by lyophilization as an easy and scalable route for the synthesis of nanocomposites. Polymerization of aniline monomers anchored on specific sites of MCC with homogeneous decoration of Se QDs results in the formation of Cellulose-PANI composites. The nanocomposite was studied for its structural, morphological and optical characteristics using XRD, FTIR, SEM and UV-Visible spectroscopy. The HRTEM images shows that Se crystallites have trigonal structure in hybrid polymer matrix.

4.5. REFERENCES

[1] Gao Z, Yang W, Wang J, Wang B, Li Z, Liu Q, et al. A New Partially Reduced Graphene Oxide Nanosheet/Polyaniline Nanowafer Hybrid as Supercapacitor Electrode Material. Energy Fuels 2013;27:568–75. https://doi.org/10.1021/ef301795g.

[2] Gupta A, Sardana S, Dalal J, Lather S, Maan AS, Tripathi R, et al. Nanostructured Polyaniline/Graphene/Fe2O3 Composites Hydrogel as a High-Performance Flexible Supercapacitor Electrode Material. ACS Appl Energy Mater 2020;3:6434–46. https://doi.org/10.1021/acsaem.0c00684.

[3] Wang S, Shang J, Wang Q, Zhang W, Wu X, Chen J, et al. Enhanced Electrochemical Performance by Strongly Anchoring Highly Crystalline Polyaniline on Multiwalled Carbon Nanotubes. ACS Appl Mater Interfaces 2017;9:43939–49. https://doi.org/10.1021/acsami.7b11567.

[4] Wang Y, Wei H, Wang J, Liu J, Guo J, Zhang X, et al. Electropolymerized polyaniline/manganese iron oxide hybrids with an enhanced color switching response and electrochemical energy storage. J Mater Chem A 2015;3:20778–90. https://doi.org/10.1039/C5TA04439A.

[5] Xu H, Tang J, Chen Y, Liu J, Pu J, Li Q. Zn2+-Doped Polyaniline/Graphene Oxide as Electrode Material for Electrochemical Supercapacitors. J Electron Mater 2017;46:6150–7. https://doi.org/10.1007/s11664-017-5638-y.

[6] Pandey K, Yadav P, Mukhopadhyay I. Elucidating the effect of copper as a redox additive and dopant on the performance of a PANI based supercapacitor. Phys Chem Chem Phys 2014;17:878–87. https://doi.org/10.1039/C4CP04321A.

[7] Asen P, Shahrokhian S, Zad AI. Transition metal ions-doped polyaniline/graphene oxide nanostructure as high performance electrode for supercapacitor applications. J Solid State Electrochem 2018;22:983–96. https://doi.org/10.1007/s10008-017-3831-9.

[8] Adriyani TR, Ensafi AA, Rezaei B. Flexible and sewable electrode based on Ni-Co@PANI-salphen composite-coated on textiles for wearable supercapacitor. Sci Rep 2023;13:19772. https://doi.org/10.1038/s41598-023-47067-y.

[9] Fan W, Zhang C, Tjiu WW, Pramoda KP, He C, Liu T. Graphene-Wrapped Polyaniline Hollow Spheres As Novel Hybrid Electrode Materials for Supercapacitor Applications. ACS Appl Mater Interfaces 2013;5:3382–91. https://doi.org/10.1021/am4003827.

[10] Zhang K, Zhang LL, Zhao XS, Wu J. Graphene/Polyaniline Nanofiber Composites as Supercapacitor Electrodes. Chem Mater 2010;22:1392–401. https://doi.org/10.1021/cm902876u.

[11] Li Z-F, Zhang H, Liu Q, Sun L, Stanciu L, Xie J. Fabrication of High-Surface-Area Graphene/Polyaniline Nanocomposites and Their Application in Supercapacitors. ACS Appl Mater Interfaces 2013;5:2685–91. https://doi.org/10.1021/am4001634.

[12] Zou Y, Zhang Z, Zhong W, Yang W. Hydrothermal direct synthesis of polyaniline, graphene/polyaniline and N-doped graphene/polyaniline hydrogels for high performance flexible supercapacitors. J Mater Chem A 2018;6:9245–56.

[13] Wu W, Wang X, Deng Y, Zhou C, Wang Z, Zhang M, et al. In situ synthesis of polyaniline/carbon nanotube composites in a carbonized wood scaffold for high performance supercapacitors. Nanoscale 2020;12:17738–45. https://doi.org/10.1039/D0NR04617E.

[14] Yu S, Liu D, Zhao S, Bao B, Jin C, Huang W, et al. Synthesis of wood derived nitrogen-doped porous carbon–polyaniline composites for supercapacitor electrode materials. RSC Adv 2015;5:30943–9. https://doi.org/10.1039/C5RA01949D.

[15] Li D, Li Y, Feng Y, Hu W, Feng W. Hierarchical graphene oxide/polyaniline nanocomposites prepared by interfacial electrochemical polymerization for flexible solid-state supercapacitors. J Mater Chem A 2015;3:2135–43. https://doi.org/10.1039/C4TA05643D.

[16] Liu R, Ma L, Huang S, Mei J, Xu J, Yuan G. Large areal mass, flexible and freestanding polyaniline/bacterial cellulose/graphene film for high-performance supercapacitors. RSC Adv 2016;6:107426–32. https://doi.org/10.1039/C6RA21920A.

[17] Pérez-Madrigal MM, Edo MG, Alemán C. Powering the future: application of cellulose-based materials for supercapacitors. Green Chem 2016;18:5930–56. https://doi.org/10.1039/C6GC02086K.

[18] Liu Z, Chen J, Zhan Y, Liu B, Xiong C, Yang Q, et al. Fe3+ Cross-Linked Polyaniline/Cellulose Nanofibril Hydrogels for High-Performance Flexible Solid-State Supercapacitors. ACS Sustain Chem Eng 2019;7:17653–60. https://doi.org/10.1021/acssuschemeng.9b03674.

[19] Wang X, Myers BD, Yan J, Shekhawat G, Dravid V, Lee PS. Manganese oxide micro-supercapacitors with ultra-high areal capacitance. Nanoscale 2013;5:4119–22. https://doi.org/10.1039/C3NR00210A.

[20] Tan H, Xiao D, Navik R, Zhao Y. Facile Fabrication of Polyaniline/Pristine Graphene–Bacterial Cellulose Composites as High-Performance Electrodes for Constructing Flexible All-Solid-State Supercapacitors. ACS Omega 2021;6:11427–35. https://doi.org/10.1021/acsomega.1c00442.

[21] Barik R, Yadav AK, Jha SN, Bhattacharyya D, Ingole PP. Two-Dimensional Tungsten Oxide/Selenium Nanocomposite Fabricated for Flexible Supercapacitors with Higher Operational Voltage and Their Charge Storage Mechanism. ACS Appl Mater Interfaces 2021;13:8102–19. https://doi.org/10.1021/acsami.0c15818.

[22] Jin Z, Nie H, Yang Z, Zhang J, Liu Z, Xu X, et al. Metal-free selenium doped carbon nanotube/graphene networks as a synergistically improved cathode catalyst for oxygen reduction reaction. Nanoscale 2012;4:6455–60. https://doi.org/10.1039/C2NR31858J.

[23] Meng X, Yu C, Song X, Iocozzia J, Hong J, Rager M, et al. Scrutinizing Defects and Defect Density of Selenium-Doped Graphene for High-Efficiency Triiodide Reduction in Dye-Sensitized Solar Cells. Angew Chem 2018;130:4772–6. https://doi.org/10.1002/ange.201801337.

[24] Gurkan YY, Kasapbasi E, Cinar Z. Enhanced solar photocatalytic activity of TiO2 by selenium(IV) ion-doping: Characterization and DFT modeling of the surface. Chem Eng J 2013;214:34–44. https://doi.org/10.1016/j.cej.2012.10.025.

[25] Kumar Yadav A, Mohammad N, Chamanehpour E, Kumar Mishra Y, K. Khanna P. Polyaniline (PANI) nanocomposites with Se, Te and their metal chalcogenides: a review. RSC Appl Polym 2024. https://doi.org/10.1039/D4LP00093E.

[26] Shumaila, Alam M, Siddiqui AM, Husain M. Synthesis, characterization and properties of Se nanowires intercalated polyaniline/Se nanocomposites. | Express Polymer Letters | EBSCOhost 2013;7:723. https://doi.org/10.3144/expresspolymlett.2013.70.

[27] Ozkazanc E, Zor S, Ozkazanc H. Synthesis, Characterization, and AC Conductivity of Polyaniline/Selenium Composites. J Macromol Sci Part B 2012;51:2122–32. https://doi.org/10.1080/00222348.2012.664451.

[28] K. Khanna P, Bhanoth S, Dhanwe V, Kshirsagar A, More P. In situ SeO 2 promoted synthesis of CdSe/PPy and Se/PPy nanocomposites and their utility in optical sensing for detection of Hg 2+ ions. RSC Adv 2015;5:92818–28. https://doi.org/10.1039/C5RA14425F.

[29] Zhang J, Xu Y, Fan L, Zhu Y, Liang J, Qian Y. Graphene–encapsulated selenium/polyaniline core–shell nanowires with enhanced electrochemical performance for Li–Se batteries. Nano Energy 2015;13:592–600. https://doi.org/10.1016/j.nanoen.2015.03.028.

[30] Lei H, Tu J, Li S, Huang Z, Luo Y, Yu Z, et al. Graphene-encapsulated selenium@polyaniline nanowires with three-dimensional hierarchical architecture for high-capacity aluminum–selenium batteries. J Mater Chem A 2022;10:15146–54. https://doi.org/10.1039/D2TA04210J.

[31] Abbasian M, Niroomand P, Jaymand M. Cellulose/polyaniline derivatives nanocomposites: Synthesis and their performance in removal of anionic dyes from simulated industrial effluents. J Appl Polym Sci 2017;134:45352. https://doi.org/10.1002/app.45352.

[32] Rana AK, Scarpa F, Thakur VK. Cellulose/polyaniline hybrid nanocomposites: Design, fabrication, and emerging multidimensional applications. Ind Crops Prod 2022;187:115356. https://doi.org/10.1016/j.indcrop.2022.115356.

[33] Qiu B, Xu C, Sun D, Yi H, Guo J, Zhang X, et al. Polyaniline Coated Ethyl Cellulose with Improved Hexavalent Chromium Removal. ACS Sustain Chem Eng 2014;2:2070–80. https://doi.org/10.1021/sc5003209.

[34] Taleb MdA, Kumar R, Barakat MA. Multifunctional carboxymethyl cellulose/graphene oxide/polyaniline hybrid thin film for adsorptive removal of Cu(II) and oxytetracycline antibiotic from wastewater. Int J Biol Macromol 2023;253:126699. https://doi.org/10.1016/j.ijbiomac.2023.126699.

[35] Li R, Liu L, Yang F. Removal of aqueous Hg(II) and Cr(VI) using phytic acid doped polyaniline/cellulose acetate composite membrane. J Hazard Mater 2014;280:20–30. https://doi.org/10.1016/j.jhazmat.2014.07.052.

[36] Gapusan RB, Balela MDL. Adsorption of anionic methyl orange dye and lead(II) heavy metal ion by polyaniline-kapok fiber nanocomposite. Mater Chem Phys 2020;243:122682. https://doi.org/10.1016/j.matchemphys.2020.122682.

[37] Dewa L, Masimba Tichapondwa S, Mhike W. Adsorption of hexavalent chromium from wastewater using polyaniline-coated microcrystalline cellulose nanocomposites. RSC Adv 2024;14:6603–16. https://doi.org/10.1039/D3RA08027G.
[38] Cheng Q, Li Q, Yuan Z, Li S, Xin JH, Ye D. Bifunctional Regenerated Cellulose/Polyaniline/Nanosilver Fibers as a Catalyst/Bactericide for Water Decontamination. ACS Appl Mater Interfaces 2021;13:4410–8. https://doi.org/10.1021/acsami.0c20188.
[39] Ragazzini I, Castagnoli R, Gualandi I, Cristina Cassani M, Nanni D, Gambassi F, et al. A resistive sensor for humidity detection based on cellulose/polyaniline. RSC Adv 2022;12:28217–26. https://doi.org/10.1039/D2RA03982F.
[40] Abdali H, Heli B, Ajji A. Cellulose Nanopaper Cross-Linked Amino Graphene/Polyaniline Sensors to Detect CO2 Gas at Room Temperature. Sensors 2019;19:5215. https://doi.org/10.3390/s19235215.
[41] Yang L, Xu X, Liu M, Chen C, Cui J, Chen X, et al. Wearable and flexible bacterial cellulose/polyaniline ammonia sensor based on a synergistic doping strategy. Sens Actuators B Chem 2021;334:129647. https://doi.org/10.1016/j.snb.2021.129647.
[42] Ravikiran YT, Kotresh S, Vijayakumari SC, Thomas S. Liquid petroleum gas sensing performance of polyaniline-carboxymethyl cellulose composite at room temperature. Curr Appl Phys 2014;14:960–4. https://doi.org/10.1016/j.cap.2014.04.015.
[43] Gopakumar DA, Pai AR, Pottathara YB, Pasquini D, Carlos de Morais L, Luke M, et al. Cellulose Nanofiber-Based Polyaniline Flexible Papers as Sustainable Microwave Absorbers in the X-Band. ACS Appl Mater Interfaces 2018;10:20032–43. https://doi.org/10.1021/acsami.8b04549.
[44] Cao Y, Andreatta A, Heeger AJ, Smith P. Influence of chemical polymerization conditions on the properties of polyaniline. Polymer 1989;30:2305–11. https://doi.org/10.1016/0032-3861(89)90266-8.
[45] Cortés MT, Sierra EV. Effect of synthesis parameters in polyaniline: influence on yield and thermal behavior. Polym Bull 2006;56:37–45. https://doi.org/10.1007/s00289-005-0467-1.
[46] Bláha M, Varga M, Prokeš J, Zhigunov A, Vohlídal J. Effects of the polymerization temperature on the structure, morphology and conductivity of polyaniline prepared with ammonium peroxodisulfate. Eur Polym J 2013;49:3904–11. https://doi.org/10.1016/j.eurpolymj.2013.08.018.
[47] Wu H, Zhang Y, Yuan W, Zhao Y, Luo S, Yuan X, et al. Highly flexible, foldable and stretchable Ni–Co layered double hydroxide/polyaniline/bacterial cellulose electrodes for high-performance all-solid-state supercapacitors. J Mater Chem A 2018;6:16617–26. https://doi.org/10.1039/C8TA05673K.
[48] El-Khodary SA, El-Enany GM, El-Okr M, Ibrahim M. Modified iron doped polyaniline/sulfonated carbon nanotubes for all symmetric solid-state supercapacitor. Synth Met 2017;233:41–51. https://doi.org/10.1016/j.synthmet.2017.09.002.
[49] Joseph N, Varghese J, Sebastian MT. A facile formulation and excellent electromagnetic absorption of room temperature curable polyaniline nanofiber based inks. J Mater Chem C 2016;4:999–1008. https://doi.org/10.1039/C5TC03080C.

[50] Mondal S, Rana U, Das P, Malik S. Network of Polyaniline Nanotubes for Wastewater Treatment and Oil/Water Separation. ACS Appl Polym Mater 2019;1:1624–33. https://doi.org/10.1021/acsapm.9b00199.
[51] Yao Q, Chen L, Zhang W, Liufu S, Chen X. Enhanced Thermoelectric Performance of Single-Walled Carbon Nanotubes/Polyaniline Hybrid Nanocomposites. ACS Nano 2010;4:2445–51. https://doi.org/10.1021/nn1002562.
[52] Janaki V, Vijayaraghavan K, Oh B-T, Ramasamy AK, Kamala-Kannan S. Synthesis, characterization and application of cellulose/polyaniline nanocomposite for the treatment of simulated textile effluent. Cellulose 2013;20:1153–66. https://doi.org/10.1007/s10570-013-9910-x.
[53] Kweon H, Lin C-W, Faruque Hasan MM, Kaner R, Sant GN. Highly Permeable Polyaniline–Graphene Oxide Nanocomposite Membranes for CO2 Separations. ACS Appl Polym Mater 2019;1:3233–41. https://doi.org/10.1021/acsapm.9b00426.
[54] Wang W, Gumfekar SP, Jiao Q, Zhao B. Ferrite-grafted polyaniline nanofibers as electromagnetic shielding materials. J Mater Chem C 2013;1:2851–9. https://doi.org/10.1039/C3TC00757J.
[55] Zhang S, Sun G, He Y, Fu R, Gu Y, Chen S. Preparation, Characterization, and Electrochromic Properties of Nanocellulose-Based Polyaniline Nanocomposite Films. ACS Appl Mater Interfaces 2017;9:16426–34. https://doi.org/10.1021/acsami.7b02794.
[56] Zheng W, Angelopoulos M, Epstein AJ, MacDiarmid AG. Experimental Evidence for Hydrogen Bonding in Polyaniline: Mechanism of Aggregate Formation and Dependency on Oxidation State. Macromolecules 1997;30:2953–5. https://doi.org/10.1021/ma9700136.
[57] Liu Q, Chen Z, Jing S, Zhuo H, Hu Y, Liu J, et al. A foldable composite electrode with excellent electrochemical performance using microfibrillated cellulose fibers as a framework. J Mater Chem A 2018;6:20338–46. https://doi.org/10.1039/C8TA06635C.
[58] Casado UM, Aranguren MI, Marcovich NE. Preparation and characterization of conductive nanostructured particles based on polyaniline and cellulose nanofibers. Ultrason Sonochem 2014;21:1641–8. https://doi.org/10.1016/j.ultsonch.2014.03.012.
[59] Anupama K, Paul T, Ann Mary KA. Solid-State Fluorescent Selenium Quantum Dots by a Solvothermal-Assisted Sol–Gel Route for Curcumin Sensing. ACS Omega 2021;6:21525–33. https://doi.org/10.1021/acsomega.1c02441.
[60] Yun YS, Yoon G, Park M, Cho SY, Lim H-D, Kim H, et al. Restoration of thermally reduced graphene oxide by atomic-level selenium doping. NPG Asia Mater 2016;8:e338–e338. https://doi.org/10.1038/am.2016.191.
[61] Luong ND, Korhonen JT, Soininen AJ, Ruokolainen J, Johansson L-S, Seppälä J. Processable polyaniline suspensions through in situ polymerization onto nanocellulose. Eur Polym J 2013;49:335–44. https://doi.org/10.1016/j.eurpolymj.2012.10.026.
[62] Ahuja P, Ujjain SK, Arora I, Samim M. Hierarchically Grown NiO-Decorated Polyaniline-Reduced Graphene Oxide Composite for Ultrafast Sunlight-Driven Photocatalysis. ACS Omega 2018;3:7846–55. https://doi.org/10.1021/acsomega.8b00765.

[63] Zhao D, Wang L, Qiu M, Zhang N. Amorphous Se Restrained by Biomass-Derived Defective Carbon for Stable Na–Se Batteries. ACS Appl Energy Mater 2021;4:7219–25. https://doi.org/10.1021/acsaem.1c01317.

[64] Poyraz S, Cerkez I, Huang TS, Liu Z, Kang L, Luo J, et al. One-Step Synthesis and Characterization of Polyaniline Nanofiber/Silver Nanoparticle Composite Networks as Antibacterial Agents. ACS Appl Mater Interfaces 2014;6:20025–34. https://doi.org/10.1021/am505571m.

[65] Lv H, Wei Z, Han C, Yang X, Tang Z, Zhang Y, et al. Cross-linked polyaniline for production of long lifespan aqueous iron||organic batteries with electrochromic properties. Nat Commun 2023;14:3117. https://doi.org/10.1038/s41467-023-38890-y.

[66] Zhang L, Wan M. Polyaniline/TiO2 Composite Nanotubes. J Phys Chem B 2003;107:6748–53. https://doi.org/10.1021/jp034130g.

[67] Luo Y, Kong D, Jia Y, Luo J, Lu Y, Zhang D, et al. Self-assembled graphene@PANI nanoworm composites with enhanced supercapacitor performance. RSC Adv 2013;3:5851–9. https://doi.org/10.1039/C3RA00151B.

[68] Zhou Z, Zhang X, Lu C, Lan L, Yuan G. Polyaniline-decorated cellulose aerogel nanocomposite with strong interfacial adhesion and enhanced photocatalytic activity. RSC Adv 2014;4:8966–72. https://doi.org/10.1039/C3RA46441E.

[69] Wang X, Deng J, Duan X, Liu D, Guo J, Liu P. Crosslinked polyaniline nanorods with improved electrochemical performance as electrode material for supercapacitors. J Mater Chem A 2014;2:12323–9. https://doi.org/10.1039/C4TA02231A.

Chapter-5

Selenium/cellulose/polyaniline nanocomposites for energy storage applications

Miniaturized electronic application calls for materials with enhanced energy storage capabilities. For past several years, much research focused on synthesis techniques that can boost the areal or volume capacitance instead of gravimetric capacitance of the material for portable and lightweight energy storage materials. Selenium/cellulose/polyaniline composites with distinct fibrillar morphology can provide improved mechanical stability to the material due to many ion-accessible active area, short diffusion path, high cyclic capacity etc. The selenium-cellulose-polyaniline composite exhibits excellent areal capacitance of 4.55 F/cm^2 at a sweep rate of 2 mV/s with retention of ~100% even after 5000 cycles of charge-discharge. The result demonstrates the indefectible potential of the composite for use in energy storage applications.

5.1. INTRODUCTION

The 21st century has seen burgeoning demand for electric vehicles and portable electronic devices in all realms of life[1,2]. Depleting fossil fuel reserves and growing energy demands has triggered minds for a cheap, efficient and capable energy storage system in the form of supercapacitors or ion batteries. Of these, supercapacitors (SC) have been stirring interests due to their ability to generate transient yet high power in addition to high energy storage capacity[3]. SC can be generally categorized into electrical double layer capacitors (EDLCs) and pseudocapacitors owing to their energy storage mechanism. While the accumulation of ionic charges at the electrode/electrolyte interface is responsible for capacitance of EDLCs, the pseudocapacitance is due to the fast and reversible faradic redox reactions at the interface[4–6]. EDLCs therefore exploit mostly carbon based porous electrode materials like carbon nanotubes[7], graphene[8], activated carbon[9], hetero-doped carbon[10] etc while latter makes use of electroactive transition metal oxides[11] like RuO_2[12], MnO_2[13], certain selenides[14,15], sulfides[16] or conducting polymers such as polypyrrole[17,18] and polyaniline[19].

Here in we report Se decorated on cellulose-polyaniline composite with enhanced electrochemical energy storage capabilities. Though selenium is a widely exploited chalcogen in various components of electronic circuitry, its composite with a conducting polymer has rarely been investigated for pseudocapacitor applications. Chalcogens (Se, S, Te) being in the same group as oxygen has also initiated efforts for energy storage studies as they are reputed

with high conductivity rich redox chemistry, multiple valence states and synergy with their counterparts[20,21]. Recent studies have affirmed that Transition Metal Chalcogenides (TMCs) especially selenides have better conductivity than TMOs[22]. Barik et.al recently elaborated the effect of Se when inserted into WO_3 matrix in the electrochemical performance of the composite[14]. Se insertions into various other metal oxides have also reportedly amplified the conductivity of the material for application in fuel cells[23], solar cells[24], photocatalysis[25].

5.1.1. Polyaniline-based nanocomposite for supercapacitor applications- review

Polyaniline (PANI) has piqued the research interests among academic community as a vibrant candidate for energy storage applications. Nanostructures of PANI are highly preferred in this regard as they display increased electroactive area with shorter ion conducting pathways[26]. The theoretical specific capacitance of pure nano-polyaniline electrodes is about 1200 Fg^{-1} which is competitive with much more expensive electrode available[27]. However, the poor mechanical stability that accompanies with the large volumetric swelling/shrinking of the polymer backbone with every charge-discharge cycle due to repeated insertion/expulsion of electrolyte ions impedes device application despite its ease of synthesis and easy functionalization abilities[28]. To resolve the issue, efforts are made towards polyaniline composite materials that integrates the features of the polymer and also possess improved material feature of the additive. Carbonaceous precursors like

graphene, graphene oxide, graphite, activated carbon or carbon nanotubes (CNTs) are regarded as efficient additives that combat the cycle instability in polyaniline. Zhang et.al., discussed a graphene/PANI supercapacitor electrode with specific capacitance of 480 F/g at a current density of 0.1 A/g with good cyclic stability[29]. The graphene oxide/PANI electrode was subjected to hydrazine reduction and the re-protonation of polyaniline to form graphene/PANI. Single or multiwalled CNTs integrated with PANI are also widely studied for energy storage applications. The report by Wu et.al, showed vertically aligned CNT/PANI composite electrode with specific capacitance of 403.3 Fg^{-1}, excellent cycling stability (90.2% retention after 3000 cycles at 4 A g^{-1}) and high energy density (98.1 Wh kg^{-1})[30]. Similarly aligned muti-walled CNT (mwCNT)/PANI composites developed by Lin et.al., showed maximum specific capacitance of 233 Fg^{-1} at a current density of 1 Ag^{-1} and high cyclic stability which was reportedly 36 times of bare mwCNT sheet, 23 times of pure polyaniline and 3 times of randomly dispersed mwCNT/polyaniline film under the same conditions[31]. Other examples of composites of PANI with carbon-based material include electrodes like reduced Graphene oxide (r-GO)/PAni as studied by Wang et.al.[32], which had no loss of capacitance even after 200 cycles at 2 A g^{-1}. Devdas et.al, studied the effect of carbon dots on the specific capacitance and energy storage abilities of PANI and PPy[33]. The composites exhibited capacitances of 676 and 529 Fg^{-1} for PPy@Cdots and PANI@Cdots, respectively for same current density. Even upon the addition of less conductive carbon dots, the composite showed better capacitive performance in comparison with pristine polymer units.

Metal nanoparticles and metal oxide have also been incorporated with PANI to enhance capacitance for energy storage. Polyaniline has been doped with transition metal like Ni^{2+} ions[34] and Co^{2+} ions[35], to study the improved energy storage capabilities. Xia et al. grew a thin layer of RuO_2 on polyaniline nanofibers to enhance the stability and energy density of the final material with capacitance retention upto 88% after 10,000 cycles[28]. Han et.al, patterned ultra-thin MnO_2 nanorods on PANI to create electrodes with specific capacitance fourfold greater than virgin PANI[36]. Literature has also seen a spurge of studies on metal-oxide -frameworks (MOF) doped polyaniline. MOFs are renowned with very high surface area, excellent chemical stability, and large pore volume and are believed to be ideal for energy storage applications. For example, Iqbal et.al., fabricated Co-intercalated MOF/PANI electrodes for supercapattery applications[37].

The filler or additive to the polymer chain could also be a conjugate polymer itself. Chen et.al, demonstrated highly uniform PPy/PANI nanospheres with maximum specific capacitance of 510 Fg^{-1} at 10 mVs^{-1} with long cyclic stability[38]. The structure was fabricated such that PPy nanospheres was the core and sea urchin-like PANI acts like the shell thereby maximizing the electroactive surface area. Ternary and quaternary nanocomposites are also investigated nowadays with a view to improve energy storage capabilities towards high performance electrochemical electrodes due to synergistic effects among individual components. Ternary graphene/Au/PANI electrode synthesized by Wang et.al., demonstrated a specific capacitance of 572 Fg^{-1},

with over 88.5% of capacitance retention after 10,000 cycles which is significantly higher than that of binary graphene-PANI composite[39]. Similarly, Martins et.al, developed r-GO/PANI/Fe_3O_4 as free-standing and flexible thin films using facile doctor blade technique for supercapacitor applications[40]. An example for quaternary composite can be Chakraborty et.al's CuO@NiO/PANI/MWCNT nanocomposites that encompass the merits of its individual components to obtain specific capacitance of 1372 Fg^{-1} and a good cyclic stability of 83% after 1500 cycles[41].

Recently fiber-based supercapacitors have picked up pace among research fraternity moving towards a broad and innovative field of wearable electronics and energy storage textiles. Some of these supercapacitors are even electrochromic, self-healing, stimuli sensitive, stretchable and perform other multifunctional applications. A recent review article from Zhao et.al, summarizes the efforts towards these flexible and 'smart' supercapacitors[42].

Out of all the known elemental counterparts, chalcogen elements like selenium plays an inevitable role in the context due to its unique and superior electrical, optical and thermal properties. Though some research has been conducted on Se-polyaniline composite material to discover applications in energy storage[43,44], medical, thermoelectric, electrical[45] and opto-electronic devices[46], reports on the detailed effects of integration of Se into polyaniline are scarce[47]. Studies considering altercations in synthesis procedure are also exploited for enhanced physical properties of these materials. This includes the use of electrochemical deposition, in-situ polymerization, electrospinning, use of various surfactants and catalysts.

5.1.2. Characteristics of supercapacitors

The choice among various types of supercapacitors (EDLCs, pseudocapacitors or hybrid) primarily depends on the application requirements of energy/power densities, cost efficiency and stability of the electrode. Understanding the performance indicators of supercapacitors is instrumental for efficient device application. It also provides considerable knowledge regarding the material and its abilities towards energy storage.

- **Specific capacitance**

The capacitance of a supercapacitor is the prime factor that decides its performance. It is a measure of the energy storage capability of the electrode and is defined as the amount of charge stored per unit mass or unit area of the material. Consequently, they are expressed in terms of Farads per gram, F/g (gravimetric capacitance) or Farads per sq. centimeter, F/cm^2 (areal capacitance). Higher the specific capacitance, greater is the ability of the electrode to store charge. Specific capacitance is generally dependent upon the nature of the electrode material, its intrinsic features like porosity, surface chemistry, the design/ architecture of the electrode, nature of the electrolyte used and measurement parameters like current density and scan rates.

- **Electrochemical impedance**

Efficient charge storage and minimal resistive losses are prerequisites for any good supercapacitors. Generally, the EIS data is interpreted by using two plots- Nyquist and Bode plots which are characterised by the following features.

Nyquist Plot- At low frequencies, the impedance is dominated by the capacitance of the electrochemical double layer (or pseudocapacitance), and there is minimal resistive loss at these frequencies and hence a near vertical graph is obtained at lower frequencies. At intermediate frequencies, a semicircle may be observed whose diameter corresponds to the charge transfer resistance (Rct) and/or contact resistance. At very high frequencies, the plot intersects the real axis (Z') and this value indicates the equivalent series resistance (ESR) of the system, which includes the internal resistance of the electrode, electrolyte resistance, and other contact resistances. Minimal intercept on the real axis (showing low ESR) and smaller semi-circular diameter (indicating quick charge transfer) at intermediate frequencies and a vertical line at lower frequencies indicating ideal capacitive behaviour is characteristic of any ideal supercapacitor.

Bode Plot- In an ideal supercapacitor Bode plot (phase vs. frequency), the phase angle approaches −90° at lower frequencies indicating good capacitive response of the material.

- **Cyclic stability**

The reliability of a supercapacitor for use in practical application greatly depends on its longevity. Energy storage devices need to maintain its capacitance capabilities over numerous cycles of working in devices. Cyclic stability of a supercapacitor describes its ability to retain the capacitance even after repeated cycles of charge-discharge. The stability is assessed by recording the capacitance of the supercapacitor for thousands or even ten-thousands cycle

of charge-discharge. It largely depends on the electrochemical nature of the electrode and the nature of the electrolyte.

- **Energy and power densities**

Energy and power densities are critical performance metrics for any energy storage device. While energy density (expressed in terms of Wh/kg or Wh/cm^2) describes the quantity of energy stored within the bulk of a supercapacitor electrode, power density (expressed in W/kg or W/cm^2) describes how rapidly this energy could be discharged from the device. Higher energy and power densities are requisites for any supercapacitors. Both these parameters are best evaluated from GCD curves in a two-electrode configuration which mimics a practical supercapacitor set up.

- **Eco-friendliness**

A supercapacitor electrode should always be eco-compatible as these materials are widely used in wearable electronics, various biomedical applications and even environmental monitoring. The choice of precursor for electrode material like biodegradable materials, cost effective agriculturally abundant sources are widely researched upon in this aspect.

5.2. EXPERIMENTAL SECTION

5.2.1. Apparatus and characterization

The materials used in the study were synthesis by fabrication routes as mentioned in chapter 4. The electrochemical measurements were made on a three-electrode system using 1M H_2SO_4 as the electrolyte at room temperature

in air. Cyclic voltammetry (CV), galvanostatic charge/discharge (GCD), electrochemical impedance spectroscopy (EIS) was recorded on BioLogic VSP electrochemical workstation.

The composites were first dispersed in ethanol and drop casted on to the glassy carbon electrode which was the working electrode. The areal capacitance values can be calculated by integrating the CV curve and also from the GCD curves using the equations (5.1) and (5.2) given below (C_a, $mFcm^{-2}$).

$$C = \frac{\int_{v1}^{v2} I(V)dV}{2(\Delta V)SA} \tag{5.1}$$

$$C = \frac{I\Delta t}{A\Delta V} \tag{5.2}$$

where *I* represents the current (A), *v1* and *v2* are starting and ending voltages (V), ΔV represents the potential window (V), *S* is the scan rate (mV/s), *A* is the area of active material of the electrode (cm^2), Δt is the discharge time (s). The energy densities (E_a, $mWhcm^{-2}$) and power density (P_a, Wcm^{-2}) were determined using the following equations (5.3) and (5.4).

$$Ea = \frac{0.5}{3.6} C(\Delta V)^2 \tag{5.3}$$

$$Pa = \frac{3600E}{\Delta t} \tag{5.4}$$

The cycling test was performed at 100 mA applied discharge current in the potential window of -0.2 to 0.8 V for 5000 cycles of charge-discharge.

The electrochemical performance of the material was also tested in a two-electrode symmetric device configuration. The material was formulated into electrodes after mixing with the binder acetylene black, polyvinylidene fluoride (PVDF) in the ratio 80:10:10. The mixture was made into a slurry paste by dispersing in NMP and then doctor-bladed on to a substrate. A filter paper wetted with aqueous solution of 1M H_2SO_4 was kept between these electrodes as separator. The sandwiched configuration serves as a symmetric supercapacitor device.

The specific areal capacitance, C (Fcm^{-2}) values from the CV and GCD graphs respectively were calculated using equation

$$C = \frac{\int_{v1}^{v2} I(V)dV}{(\Delta V)SA} \tag{5.5}$$

$$C = 2\frac{I\Delta t}{A\Delta V} \tag{5.6}$$

where *I* represents the current (A), *v1* and *v2* are starting and ending voltages (V), ΔV is the operated potential window (V), *S* is the applied scan rate (mV/s), *A* is the area of active material on one of the electrodes (cm^2) and Δt is the discharge time (s). Here, in both the equations, a factor of 2 is multiplied in comparison with equations (5.1) and (5.2) due to the formation of series capacitance in a symmetrical supercapacitor device. The energy and power

densities of the device can be evaluated from the equations (5.3) and (5.4) respectively.

5.3. RESULTS AND DISCUSSION

5.3.1. Cyclic voltammetry studies

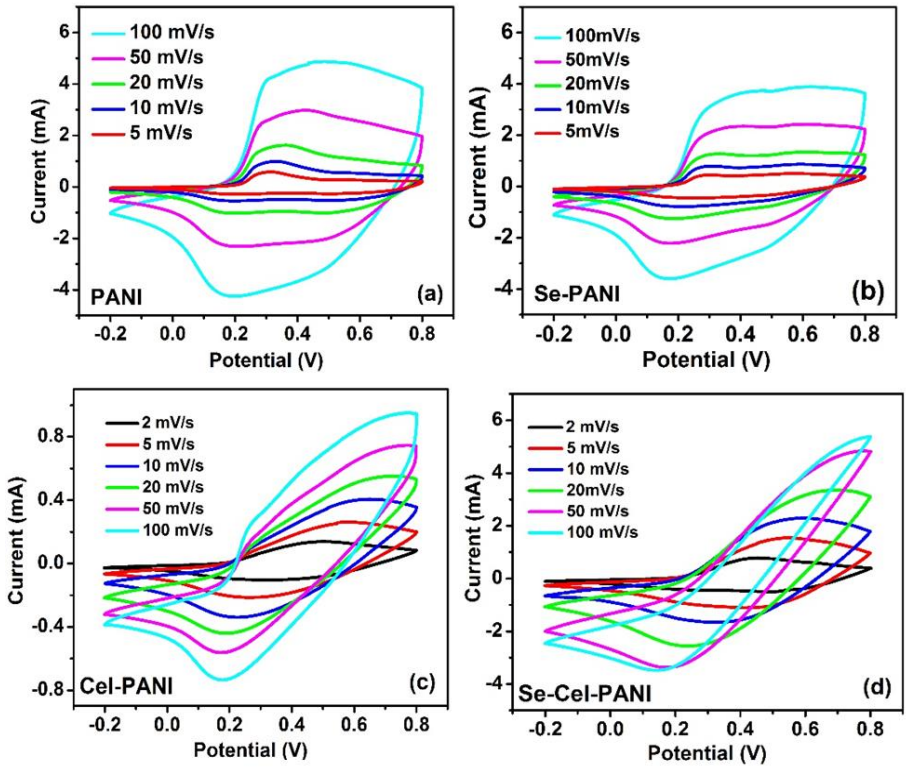

Figure 5.1. (a-d) CV curves at different scan rates of PANI, Se-PANI, Cel-PANI and Se-Cel-PANI composite

The CV response at various scan rates at varying discharge current of composites are shown in **Figure 5.1(a-d)** respectively. In the CV profiles, with

increasing scan rates, the response current also increased for each composite indicating a good rate capability of the electrode. Also, a positive shift in the oxidation peak and a negative shift in the reduction peak are noted for all composites with increasing scan rate, which may be due to internal resistance. The redox peaks at 0.6 V/0.5 V becomes less apparent at higher scan rates for each composite as the electrolyte fail to diffuse into and out of the interior of the electrode within such short time. However, the redox peak current retains its shape for each composite with this increasing sweep rate indicating fast current responses by the composite.

5.3.2. Galvanostatic charge-discharge studies

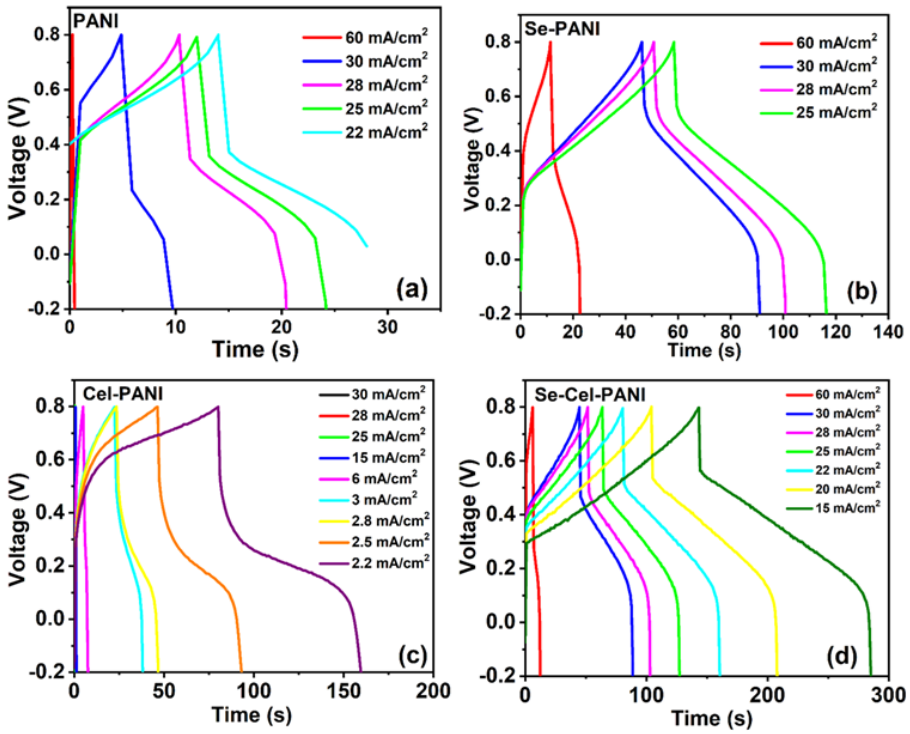

Figure 5.2.(a-d) GCD curves at varying discharge current of PANI, Se-PANI, Cel-PANI and Se-Cel-PANI composites

The GCD curves (**Figure 5.2(a-d)**) of the composites reveal a short discharge from the potential 0.8V followed by a linear region in the curve to 0V. Also, the discharge time was found to be inversely proportional to the current as larger current can build up the same charge or same voltage in a system in shorter time. The asymmetrical shape of the GCD curves indicates the pseudocapacitive nature of the as-synthesized materials.

5.3.3. Comparison of electrochemical performance of the composites

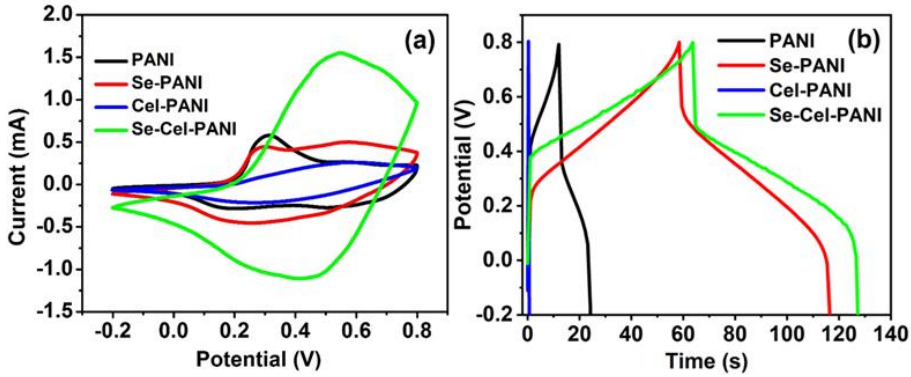

Figure 5.3. (a) CV curves at 5 mV/s scan rate (b) GCD curves at 25 mA/cm^2 discharge current of PANI, Se-PANI, Cel-PANI and Se-Cel-PANI composite.

The electrochemical performance of the composites was investigated using three electrode cells and evaluated using Cyclic Voltammetry (CV) and Galvanostatic Charge-Discharge (GCD) and electrochemical impedance spectroscopy (EIS) studies. **Figure 5.3(a)** shows the cyclic voltammetric performance of the composites at 5 mV/s scan rate in the potential window from -0.2 to 0.8 V. For PANI, the first pair of redox waves (P_1/P_2 at ~0.3/0.2 V) can be attributed to leucoemeraldine to polaronic emeraldine transition of PANI, while the second set of peaks (P_3/P_4 at ~0.6/0.5 V) are related to the emeraldine/pernigraniline transformations of PANI correspondingly[48]. The CV characteristics remains almost invariant for Se-PANI composites, which indicated that PANI suffered similar charge/discharge reactions in Se-PANI. Additionally, area enclosed by the CV curve is increased hence Se-PANI have higher areal capacitance. These redox peaks are however less apparent in Cel-

PANI and Se-Cel-PANI nanocomposites. The synergistic effects of the components of the composites have a direct effect on the shape and size of the CV spectra[49]. Presence of cellulose in the matrix hinders the easy interconversion and redox cycle of the polymer chains and hence the aforesaid peaks become less intense in their CV spectra. Evidently, Se-Cel-PANI has higher current response compared to its counterparts indicating that the material possesses greater electrochemical active area that aids in better conductivity and capacitance capabilities. The fibrillar morphology of the composite allows the efficient diffusion of the electrolyte ions into the interior of the network thereby allowing better access to the active sites. The increased current response can also be attributed to the synergistic effect of Se and PANI nanofibres and increased charge accumulation in electrode – electrolyte interface. The **Figure 5.3(b)** shows the galvanostatic charge-discharge curves of PANI, Se-PANI, Cel-PANI and Se-Cel-PANI composites in the potential range -0.2 V to 0.8 V at an applied current density of 25 mA/cm^2. The asymmetrical nature of the triangles exhibited by the GCD profiles indicates the pseudocapacitive behavior of the material as a result of electrochemical interaction occurring at the electrode-electrolyte interface[50]. A voltage drop is noted in the discharge curve which can be attributed to the internal resistance[51]. This drop is however less for Se containing composites in comparison with PANI and Cel-PANI which could be due to reduced internal resistance caused by the shortened transfer path of ions in the matrix owing to the conductivity of Se. The discharging time was found to be longer for Se-Cel-PANI ternary composite indicating excellent electrochemical behavior.

5.3.4. Areal capacitance

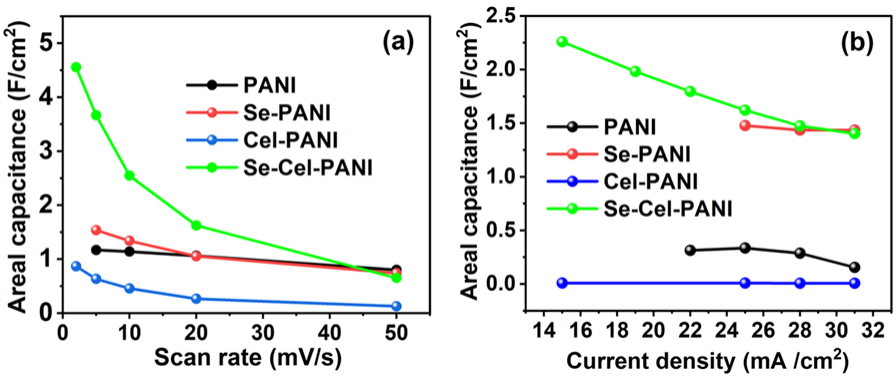

Figure 5.4. Variation of specific areal capacitance (a) against scan rate obtained from CV and (b) against current density obtained from GCD

The areal capacitance as a function of current scan rate is given in **Figure 5.4(a)** The capacitance decreased with ascending scan rates. At higher rates of scan, inner active sites of the electrode would be unable to keep up with the redox transition and as a result, all active species do not participate in the charging process. In this sense, only the areal capacitance at slower scan rate can suggest almost complete utilization of the electrode material[52]. The Se-Cel-PANI composite showed exceptionally high capacitance of 4.55 F/cm^2 at a scan rate of 2 mV/s which is greater than many other reported capacitance values for a conducting polymer-based composite. This can be ascribed to the enhanced electrochemically active surface spots in the composite which further allows the percolation of ions from the electrolyte with better adsorption and desorption upon charge-discharge. The porous 3D network of cellulose offers a conductive frame for polyaniline along with the adsorbed Se entities that shortens the charge transfer distance from PANI to the current collector. In

addition to this, Se in the composite may have increased the conductivity of the material by offering richer active sites and channels for ion transport[14]. Thus, even though Se-Cel-PANI composite has less surface area and pore size, it exhibits shown outstanding areal capacitance than many reported candidates. The areal capacitance value is in the order of Cel-PANI< PANI< Se-PANI<Se-Cel-PANI demonstrating that Se-Cel-PANI exhibit better electrochemical performance in comparison to its counterparts. The specific areal capacitance of Se-Cel-PANI composite evaluated from the GCD plot (**Figure 5.4(b)**) was 2.250 F/cm^2 at a current density of 15 mA/cm^2. The areal capacitance values obtained from the GCD values were also observed to be consistent with those obtained from CV spectra.

5.3.5. Nyquist Plot

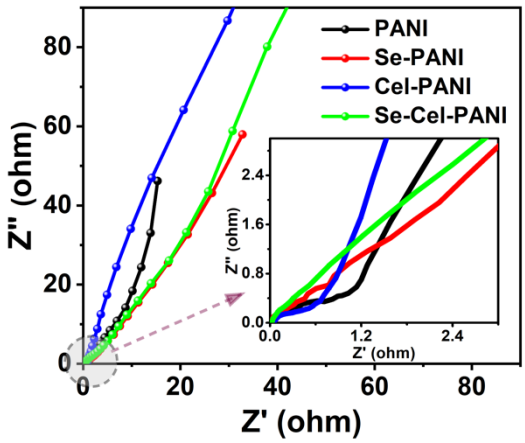

Figure 5.5. Nyquist plot of PANI, Se-PANI, Cel-PANI and Se-Cel-PANI composites; inset shows the expanded EIS spectra

The Nyquist plot (**Figure 5.5**) was recorded from the electrochemical impedance spectroscopy to study the internal resistance, charge transfer kinetics and ion-diffusion process in the composite. A semicircle arc towards higher frequencies followed by a vertical plot with larger slope in the low frequency region is characteristic of any EIS spectra. While the former can be attributed to the contact impedance generated by the electrode and electrolyte resistance, the latter corresponds to capacitive behaviour. The diameter/ first intercept of this semi-circle with the x-axis gives the charge transfer resistance for the material[53]. Se-Cel-PANI electrode evidently exhibit an inconspicuous semicircle/intercept with Z' axis among all other electrodes (inset of **Figure 5.5**). Such low values for charge transfer resistances (R_{ct}) indicate that the composite showed good conductivity and least resistance to ion exchange between electrode-electrolyte pair and ideal capacitive behavior.

5.3.6. Cyclic stability

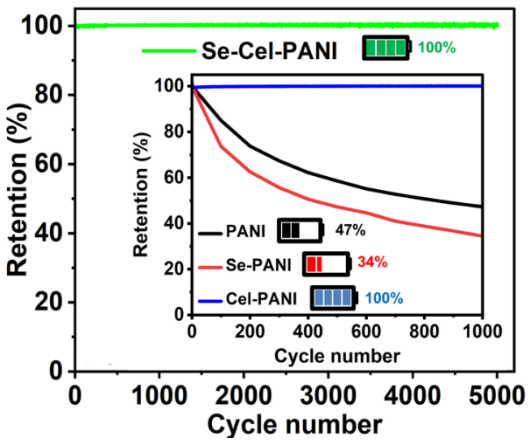

Figure 5.6. (a) Capacitance retention (in%) from GCD at a constant discharge current of 100 mA for varying number of charge-discharge cycles; inset shows the cyclic

retention (in %) of PANI, Se-PANI, Cel-PANI and Se-Cel-PANI composites for 1000 cycles

The cyclic stability of Se-Cel-PANI nanocomposites for 5000 GCD cycles at 100 mA discharge current is given in **Figure 5.6**. The material exhibited excellent capacitance retention of ~100% even after 5000 cycles of charge-discharge. The **inset of Figure 5.6(a)** illustrates the cyclic retention of PANI, Se-PANI, Cel-PANI and Se-Cel-PANI composites for 1000 GCD cycles at an applied discharge current of 100 mA. A dropped capacitance value of approximately 47.2% and 34.4% was observed at the end of 1000 cycles for PANI and Se-PANI respectively. However, cellulose containing composites showed a sustained retention of ~100% at the end of 1000 cycles of charge-discharge. Se-Cel-PANI showed nearly no drop in capacitance even after 5000 cycles. Conducting polymer-based composites usually have poor capacitance retention values due to the shrinking and swelling of PANI chains with the continuous doping/de-doping processes. However, the stability studies suggest that its composition with cellulose meliorated the situation effectively by enhancing the strength of the polymer backbone. Though Cel-PANI and Se-Cel-PANI exhibits remarkable cyclic stability, the specific capacitance considerations would entitle Se-Cel-PANI ternary composite as an ideal candidate for energy storage applications.

5.3.7. Energy and power densities (Ragone plot)

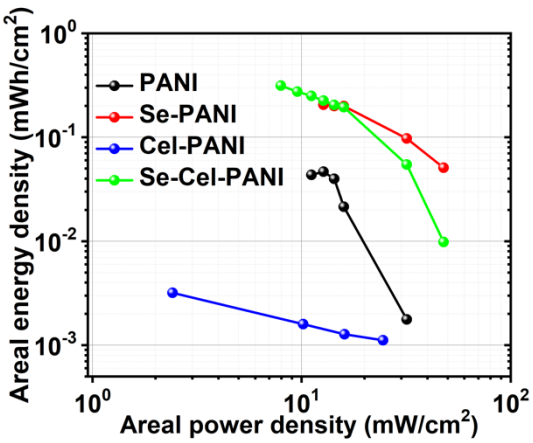

Figure 5.7. Areal normalized Ragone plot of Se/Cellulose/PANI composite

Figure 5.7 shows the areal ragone plot for the composites evaluated from GCD data. The graph compares the specific energy and specific power associated in different energy storage devices. The Se-Cel-PANI ternary composite exhibited a remarkable areal energy density of 313.6 µWhcm^{-2} at 15 mAcm^{-2} current density. The corresponding power density was evaluated to be 8 mWcm^{-2}. In addition to this, maximum power density was found to be 47.77 mWcm^{-2} at an energy density of 9.82 µWhcm^{-2}. These areal energy/power density values were found to be superior to that of electrodes reported in literature and opens vast horizons of applications for Se based energy storage devices.

Table 5.1 lists the comparison of some literatures on the electrochemical performance of certain cellulose-polyaniline based composites synthesized via in-situ polymerization.

Table. 5.1. Literature on various cellulose-polyaniline composites synthesised by chemical oxidative polymerisation reported as electrodes for supercapacitor applications using 1M H_2SO_4 as electrolyte

Electrode material	**Specific Capacitance**	**Stability (cycles)**	**Ref**
Cellulose fibre/SWCNT/PANI	330 mF/cm^2, 0.2 mA/cm^2	79% (1000)	[54]
Cellulose paper/graphite/PANI	355.6 mF/cm^2, 0.5 mA/cm^2	83% (10000)	[55]
Cellulose aerogel/Ag/PANI	217 F/g, 0.1 A/g	83% (1000)	[56]
Fe^{3+}/Cellulose/PANI	3060 mF/cm^2, 0.5 mA/cm^2	79% (1000)	[57]
Cellulose/GO/PANI aerogel	1218 mF/cm^2, 1mA/cm^2	83% (1000)	[58]
MXene ($Ti_3C_2T_x$)/CNF/PANI	2935 mF/cm^2, 1 mA/cm^2	94% (2000)	[59]
Nanocellulose/MWCNT/PANI	2176.3 mF/cm^2, 1 mA/cm^2	64% (1050)	[60]
CNF/CCS/$PANI_{2:2:1}$	1838.5 mF/cm^2, 1 mA/cm^2	83.2% (3000)	[61]
Se/Cellulose/PANI	**2250 mF/cm^2, 15 mA/cm^2**	**~100% (5000)**	**This work**

5.3.8. Electrochemical performance of the composite in a two-electrode symmetric capacitor configuration

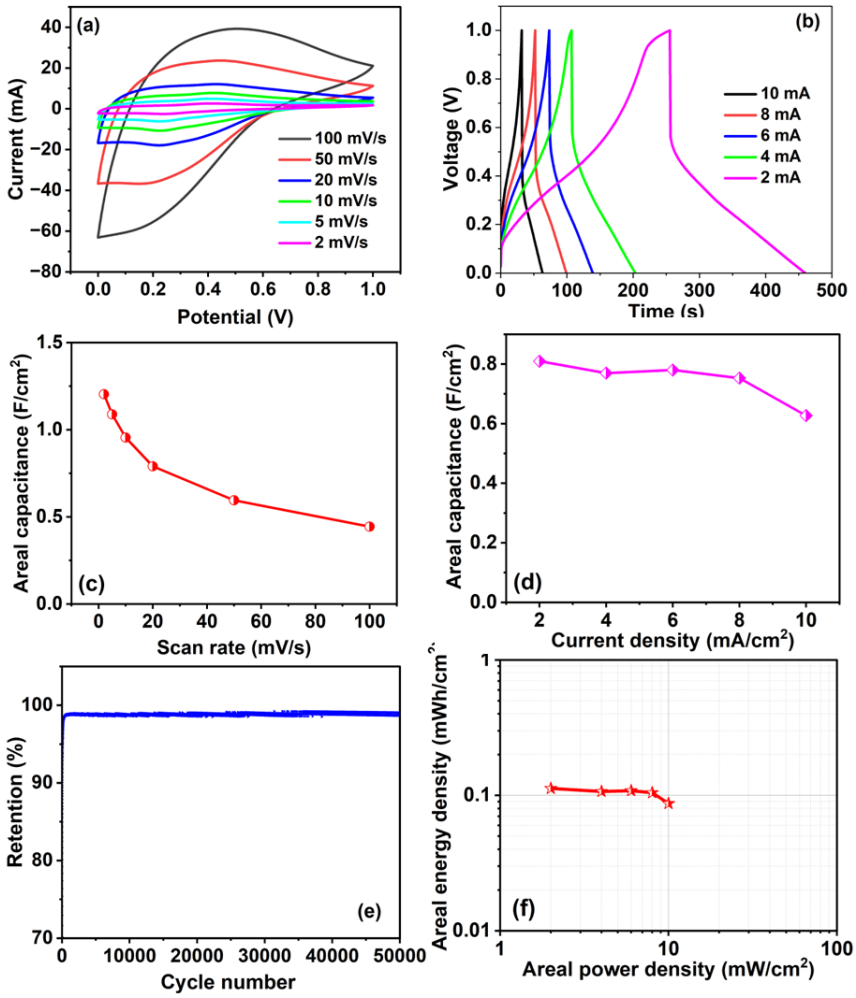

Figure 5.8. (a) CV (b) GCD response of Se-Cel-PANI composites in two electrode configuration (c,d) calculated specific areal capacitance from CV and GCD profiles respectively (c) Capacitance retention (in %) from GCD varying number of charge-discharge cycles; (d) Areal normalized Ragone plot

To test the electrochemical performance of the composite in a real energy storage system, the material was tested on a two-electrode symmetric supercapacitor configuration**. Figure 5.8(a)** and **Figure 5.8(b)** indicates the CV and GCD response of the device respectively. The CV plot recorded for an operational potential window of 0-1 V clearly indicates the pseudocapacitive nature of the material. The GCD plots are not exactly triangular in nature indicating non-linear redox process occurring in the material. The specific areal capacitance estimated from the CV curve is plotted in **Figure 5.8(c)**. The material showed an exceptional areal capacitance of 1.203 F/cm^2 at a scan rate of 2 mV/s. With the increasing rates of scan, the electrolyte ions are unable to move in and out of the ions in the reduced time and hence capacitance values decrease. The specific areal capacitance plotted from the GCD response of the material (given **in Figure 5.8(d)**) shows a capacitance of 0.809 F/cm^2 at a current density of 2 mA/cm^2. The complete synergy between the constituents and their ability to meliorate the capabilities of one another has effectively increased the areal capacitance of the device. The value is significantly better than most of the areal capacitance obtained for some symmetrical supercapacitor devices. The cyclic retention exhibited by the device at a discharge current of 20 mA for 50,000 cycles of charge-discharge is shown in **Figure 5.8(e).** The material showed an exceptional stability of 100% even after 50,000 cycles of charge -discharge. The areal ragone plot obtained from the GCD response of the device is given in **Figure 5.8(f).** The device exhibited a maximum power density 10 mW/cm^2 at energy density 0.087 mWh/cm^2. The fabricated device

has hence shown immense potential in terms of stability and energy storage for use in practical supercapacitor applications.

5.4. CONCLUSION

In the present work, Se/Cellulose/PANI nanocomposites are studied for their electrochemical performance. The Se-cellulose-PANI composite showed an admirable areal capacitance of 4.55 Fcm^{-2} at a scan rate of 2 mV/s with an excellent retention of ~100% for 5000 cycles. The remarkable areal energy density of 313.6 $\mu Whcm^{-2}$ at power density of 8 $mWcm^{-2}$ suggests the outperformance of the material compared to some previously reported polyaniline composites. The enhanced areal performance of the ternary composite can be attributed to the high conductivity of PANI in the matrix and simultaneous contribution of mechanical strength from cellulose onto the polymer adhered over it. Selenium was found to play a vital role in the composite by endowing it with additional conductivity. The design and synthesis method adopted offers a facile, room-temperature cured and scalable approach for the design of electrode materials for enhanced supercapacitor applications.

5.5. REFERENCES

[1] Kyerematenng NA, Brousse T, Pech D. Microsupercapacitors as miniaturized energy-storage components for on-chip electronics. Nat Nanotechnol 2017;12:7–15. https://doi.org/10.1038/nnano.2016.196.

[2] Dubal DP, Chodankar NR, Kim D-H, Gomez-Romero P. Towards flexible solid-state supercapacitors for smart and wearable electronics. Chem Soc Rev 2018;47:2065–129. https://doi.org/10.1039/C7CS00505A.

[3] Li Y, Zhao X, Xu Q, Zhang Q, Chen D. Facile Preparation and Enhanced Capacitance of the Polyaniline/Sodium Alginate Nanofiber Network for Supercapacitors. Langmuir 2011;27:6458–63. https://doi.org/10.1021/la2003063.

[4] Das AK, Paria S, Maitra A, Halder L, Bera A, Bera R, et al. Highly Rate Capable Nanoflower-like NiSe and WO3@PPy Composite Electrode Materials toward High Energy Density Flexible All-Solid-State Asymmetric Supercapacitor. ACS Appl Electron Mater 2019;1:977–90. https://doi.org/10.1021/acsaelm.9b00164.

[5] Konwar G, Sarma SCh, Mahanta D, Peter SC. Polyaniline Hybrid Nanofibers via Green Interfacial Polymerization for All-Solid-State Symmetric Supercapacitors. ACS Omega 2020;5:14494–501. https://doi.org/10.1021/acsomega.0c01158.

[6] Fleischmann S, Mitchell JB, Wang R, Zhan C, Jiang D, Presser V, et al. Pseudocapacitance: From Fundamental Understanding to High Power Energy Storage Materials. Chem Rev 2020;120:6738–82. https://doi.org/10.1021/acs.chemrev.0c00170.

[7] Pan H, Li J, Feng Y. Carbon Nanotubes for Supercapacitor. Nanoscale Res Lett 2010;5:654. https://doi.org/10.1007/s11671-009-9508-2.

[8] Tan YB, Lee J-M. Graphene for supercapacitor applications. J Mater Chem A 2013;1:14814–43. https://doi.org/10.1039/C3TA12193C.

[9] Li B, Dai F, Xiao Q, Yang L, Shen J, Zhang C, et al. Nitrogen-doped activated carbon for a high energy hybrid supercapacitor. Energy Environ Sci 2016;9:102–6. https://doi.org/10.1039/C5EE03149D.

[10] Yan L, Li D, Yan T, Chen G, Shi L, An Z, et al. N,P,S-Codoped Hierarchically Porous Carbon Spheres with Well-Balanced Gravimetric/Volumetric Capacitance for Supercapacitors. ACS Sustain Chem Eng 2018;6:5265–72. https://doi.org/10.1021/acssuschemeng.7b04922.

[11] Jayakumar S, Santhosh PC, Mohideen MM, Radhamani AV. A comprehensive review of metal oxides (RuO2, Co3O4, MnO2 and NiO) for supercapacitor applications and global market trends. J Alloys Compd 2024;976:173170. https://doi.org/10.1016/j.jallcom.2023.173170.

[12] Subramanian V, Hall SC, Smith PH, Rambabu B. Mesoporous anhydrous RuO2 as a supercapacitor electrode material. Solid State Ion 2004;175:511–5. https://doi.org/10.1016/j.ssi.2004.01.070.

[13] Wang X, Myers BD, Yan J, Shekhawat G, Dravid V, Lee PS. Manganese oxide micro-supercapacitors with ultra-high areal capacitance. Nanoscale 2013;5:4119–22. https://doi.org/10.1039/C3NR00210A.

[14] Barik R, Yadav AK, Jha SN, Bhattacharyya D, Ingole PP. Two-Dimensional Tungsten Oxide/Selenium Nanocomposite Fabricated for Flexible Supercapacitors with Higher Operational Voltage and Their Charge Storage Mechanism. ACS Appl Mater Interfaces 2021;13:8102–19. https://doi.org/10.1021/acsami.0c15818.

[15] Tang G, Liang J, Wu W. Transition Metal Selenides for Supercapacitors. Adv Funct Mater n.d.;n/a:2310399. https://doi.org/10.1002/adfm.202310399.

[16] Chen I-WP, Chou Y-C, Wang P-Y. Integration of Ultrathin MoS2/PANI/CNT Composite Paper in Producing All-Solid-State Flexible Supercapacitors with Exceptional Volumetric Energy Density. J Phys Chem C 2019;123:17864–72. https://doi.org/10.1021/acs.jpcc.9b04046.

[17] Wang S, Liang Y, Zhuo W, Lei H, Javed MS, Liu B, et al. Freestanding polypyrrole/carbon nanotube electrodes with high mass loading for robust flexible supercapacitors. Mater Chem Front 2021;5:1324–9. https://doi.org/10.1039/D0QM00649A.

[18] Zhou H, Han G, Xiao Y, Chang Y, Zhai H-J. Facile preparation of polypyrrole/graphene oxide nanocomposites with large areal capacitance using electrochemical codeposition for supercapacitors. J Power Sources 2014;263:259–67. https://doi.org/10.1016/j.jpowsour.2014.04.039.

[19] Wang Z-L, Guo R, Li G-R, Lu H-L, Liu Z-Q, Xiao F-M, et al. Polyaniline nanotube arrays as high-performance flexible electrodes for electrochemical energy storage devices. J Mater Chem 2012;22:2401–4. https://doi.org/10.1039/C2JM15070K.

[20] Lamiel C, Hussain I, Rabiee H, Ogunsakin OR, Zhang K. Metal-organic framework-derived transition metal chalcogenides (S, Se, and Te): Challenges, recent progress, and future directions in electrochemical energy storage and conversion systems. Coord Chem Rev 2023;480:215030. https://doi.org/10.1016/j.ccr.2023.215030.

[21] Dahiya Y, Hariram M, Kumar M, Jain A, Sarkar D. Modified transition metal chalcogenides for high performance supercapacitors: Current trends and emerging opportunities. Coord Chem Rev 2022;451:214265. https://doi.org/10.1016/j.ccr.2021.214265.

[22] Anantharaj S, Ede SR, Sakthikumar K, Karthick K, Mishra S, Kundu S. Recent Trends and Perspectives in Electrochemical Water Splitting with an Emphasis on Sulfide, Selenide, and Phosphide Catalysts of Fe, Co, and Ni: A Review. ACS Catal 2016;6:8069–97. https://doi.org/10.1021/acscatal.6b02479.

[23] Jin Z, Nie H, Yang Z, Zhang J, Liu Z, Xu X, et al. Metal-free selenium doped carbon nanotube/graphene networks as a synergistically improved cathode catalyst for oxygen reduction reaction. Nanoscale 2012;4:6455–60. https://doi.org/10.1039/C2NR31858J.

[24] Meng X, Yu C, Song X, Iocozzia J, Hong J, Rager M, et al. Scrutinizing Defects and Defect Density of Selenium-Doped Graphene for High-Efficiency Triiodide Reduction in Dye-Sensitized Solar Cells. Angew Chem 2018;130:4772–6. https://doi.org/10.1002/ange.201801337.

[25] Gurkan YY, Kasapbasi E, Cinar Z. Enhanced solar photocatalytic activity of TiO2 by selenium(IV) ion-doping: Characterization and DFT modeling of the surface. Chem Eng J 2013;214:34–44. https://doi.org/10.1016/j.cej.2012.10.025.

[26] Xu H, Li X, Wang G. Polyaniline nanofibers with a high specific surface area and an improved pore structure for supercapacitors. J Power Sources 2015;294:16–21. https://doi.org/10.1016/j.jpowsour.2015.06.053.
[27] Peng C, Hu D, Chen GZ. Theoretical specific capacitance based on charge storage mechanisms of conducting polymers: Comment on 'Vertically oriented arrays of polyaniline nanorods and their super electrochemical properties.' Chem Commun 2011;47:4105–7. https://doi.org/10.1039/C1CC10675A.
[28] Xia C, Chen W, Wang X, Hedhili MN, Wei N, Alshareef HN. Highly Stable Supercapacitors with Conducting Polymer Core-Shell Electrodes for Energy Storage Applications. Adv Energy Mater 2015;5:1401805. https://doi.org/10.1002/aenm.201401805.
[29] Zhang K, Zhang LL, Zhao XS, Wu J. Graphene/Polyaniline Nanofiber Composites as Supercapacitor Electrodes. Chem Mater 2010;22:1392–401. https://doi.org/10.1021/cm902876u.
[30] Wu G, Tan P, Wang D, Li Z, Peng L, Hu Y, et al. High-performance Supercapacitors Based on Electrochemical-induced Vertical-aligned Carbon Nanotubes and Polyaniline Nanocomposite Electrodes. Sci Rep 2017;7:43676. https://doi.org/10.1038/srep43676.
[31] Lin H, Li L, Ren J, Cai Z, Qiu L, Yang Z, et al. Conducting polymer composite film incorporated with aligned carbon nanotubes for transparent, flexible and efficient supercapacitor. Sci Rep 2013;3:1353. https://doi.org/10.1038/srep01353.
[32] Wang L, Ye Y, Lu X, Wen Z, Li Z, Hou H, et al. Hierarchical Nanocomposites of Polyaniline Nanowire Arrays on Reduced Graphene Oxide Sheets for Supercapacitors. Sci Rep 2013;3:3568. https://doi.org/10.1038/srep03568.
[33] Devadas B, Imae T. Effect of Carbon Dots on Conducting Polymers for Energy Storage Applications. ACS Sustain Chem Eng 2018;6:127–34. https://doi.org/10.1021/acssuschemeng.7b01858.
[34] Arulmani S, Wu JJ, Anandan S. Ultrasound promoted transition metal doped polyaniline nanofibers: Enhanced electrode material for electrochemical energy storage applications. Ultrason Sonochem 2019;51:469–77. https://doi.org/10.1016/j.ultsonch.2018.07.006.
[35] Mu Y, Ruan C, Li P, Xu J, Xie Y. Enhancement of electrochemical performance of cobalt (II) coordinated polyaniline: A combined experimental and theoretical study. Electrochimica Acta 2020;338:135881. https://doi.org/10.1016/j.electacta.2020.135881.
[36] Han J, Li L, Fang P, Guo R. Ultrathin MnO2 Nanorods on Conducting Polymer Nanofibers as a New Class of Hierarchical Nanostructures for High-Performance Supercapacitors. J Phys Chem C 2012;116:15900–7. https://doi.org/10.1021/jp303324x.
[37] Iqbal MZ, Faisal MM, Ali SR, Farid S, Afzal AM. Co-MOF/polyaniline-based electrode material for high performance supercapattery devices. Electrochimica Acta 2020;346:136039. https://doi.org/10.1016/j.electacta.2020.136039.

[38] Chen S, Cheng H, Tian D, Li Q, Zhong M, Chen J, et al. Controllable Synthesis, Core-Shell Nanostructures, and Supercapacitor Performance of Highly Uniform Polypyrrole/Polyaniline Nanospheres. ACS Appl Energy Mater 2021;4:3701–11. https://doi.org/10.1021/acsaem.1c00131.

[39] Wang L, Wu T, Du S, Pei M, Guo W, Wei S. High Performance Supercapacitors Based On Ternary Graphene/Au/Polyaniline (PANI) Hierarchical Nanocomposites. RSC Adv n.d.

[40] Martins VHN, Siqueira NMS, Fonsaca JES, Domingues SH, Souza VHR. Ternary Nanocomposites of Reduced Graphene Oxide, Polyaniline, and Iron Oxide Applied for Energy Storage. ACS Appl Nano Mater 2021;4:5553–63. https://doi.org/10.1021/acsanm.1c01036.

[41] Chakraborty I, Chakrabarty N, Senapati A, Chakraborty AK. CuO@NiO/Polyaniline/MWCNT Nanocomposite as High-Performance Electrode for Supercapacitor. J Phys Chem C 2018;122:27180–90. https://doi.org/10.1021/acs.jpcc.8b08091.

[42] Zhao Z, Xia K, Hou Y, Zhang Q, Ye Z, Lu J. Designing flexible, smart and self-sustainable supercapacitors for portable/wearable electronics: from conductive polymers. Chem Soc Rev 2021;50:12702–43. https://doi.org/10.1039/D1CS00800E.

[43] Zhang J, Xu Y, Fan L, Zhu Y, Liang J, Qian Y. Graphene–encapsulated selenium/polyaniline core–shell nanowires with enhanced electrochemical performance for Li–Se batteries. Nano Energy 2015;13:592–600. https://doi.org/10.1016/j.nanoen.2015.03.028.

[44] Lei H, Tu J, Li S, Huang Z, Luo Y, Yu Z, et al. Graphene-encapsulated selenium@polyaniline nanowires with three-dimensional hierarchical architecture for high-capacity aluminum–selenium batteries. J Mater Chem A 2022;10:15146–54. https://doi.org/10.1039/D2TA04210J.

[45] Ozkazanc E, Zor S, Ozkazanc H. Synthesis, Characterization, and AC Conductivity of Polyaniline/Selenium Composites. J Macromol Sci Part B 2012;51:2122–32. https://doi.org/10.1080/00222348.2012.664451.

[46] Heiba ZK, Mohamed MB, Imam NG. Structural, Optical and Magnetic Properties of PANI/Se0.95Fe0.05 Nanocomposites. J Supercond Nov Magn 2019;32:2981–6. https://doi.org/10.1007/s10948-019-5074-8.

[47] Kumar Yadav A, Mohammad N, Chamanehpour E, Kumar Mishra Y, K. Khanna P. Polyaniline (PANI) nanocomposites with Se, Te and their metal chalcogenides: a review. RSC Appl Polym 2024. https://doi.org/10.1039/D4LP00093E.

[48] Wang D-W, Li F, Zhao J, Ren W, Chen Z-G, Tan J, et al. Fabrication of Graphene/Polyaniline Composite Paper *via In Situ* Anodic Electropolymerization for High-Performance Flexible Electrode. ACS Nano 2009;3:1745–52. https://doi.org/10.1021/nn900297m.

[49] Kumar NA, Choi H-J, Shin YR, Chang DW, Dai L, Baek J-B. Polyaniline-Grafted Reduced Graphene Oxide for Efficient Electrochemical Supercapacitors. ACS Nano 2012;6:1715–23. https://doi.org/10.1021/nn204688c.

[50] Yan J, Wei T, Shao B, Fan Z, Qian W, Zhang M, et al. Preparation of a graphene nanosheet/polyaniline composite with high specific capacitance. Carbon 2010;48:487–93. https://doi.org/10.1016/j.carbon.2009.09.066.

[51] Wang X, Deng J, Duan X, Liu D, Guo J, Liu P. Crosslinked polyaniline nanorods with improved electrochemical performance as electrode material for supercapacitors. J Mater Chem A 2014;2:12323–9. https://doi.org/10.1039/C4TA02231A.

[52] Waikar MR, Shaikh AA, Sonkawade RG. PANINFs synthesized electrochemically as an electrode material for energy storage application. Polym Bull 2019;76:4703–18. https://doi.org/10.1007/s00289-018-2634-1.

[53] Laschuk NO, Easton EB, Zenkina OV. Reducing the resistance for the use of electrochemical impedance spectroscopy analysis in materials chemistry. RSC Adv n.d.;11:27925–36. https://doi.org/10.1039/d1ra03785d.

[54] Ge D, Yang L, Fan L, Zhang C, Xiao X, Gogotsi Y, et al. Foldable supercapacitors from triple networks of macroporous cellulose fibers, single-walled carbon nanotubes and polyaniline nanoribbons. Nano Energy 2015;11:568–78. https://doi.org/10.1016/j.nanoen.2014.11.023.

[55] Yao B, Yuan L, Xiao X, Zhang J, Qi Y, Zhou J, et al. Paper-based solid-state supercapacitors with pencil-drawing graphite/polyaniline networks hybrid electrodes. Nano Energy 2013;2:1071–8. https://doi.org/10.1016/j.nanoen.2013.09.002.

[56] Tian J, Peng D, Wu X, Li W, Deng H, Liu S. Electrodeposition of Ag nanoparticles on conductive polyaniline/cellulose aerogels with increased synergistic effect for energy storage. Carbohydr Polym 2017;156:19–25. https://doi.org/10.1016/j.carbpol.2016.09.005.

[57] Liu Z, Chen J, Zhan Y, Liu B, Xiong C, Yang Q, et al. Fe3+ Cross-Linked Polyaniline/Cellulose Nanofibril Hydrogels for High-Performance Flexible Solid-State Supercapacitors. ACS Sustain Chem Eng 2019;7:17653–60. https://doi.org/10.1021/acssuschemeng.9b03674.

[58] Li Y, Xia Z, Gong Q, Liu X, Yang Y, Chen C, et al. Green Synthesis of Free Standing Cellulose/Graphene Oxide/Polyaniline Aerogel Electrode for High-Performance Flexible All-Solid-State Supercapacitors. Nanomaterials 2020;10:1546. https://doi.org/10.3390/nano10081546.

[59] Yuan T, Zhang Z, Liu Q, Liu X-T, Miao Y-N, Yao C. MXene (Ti3C2Tx)/cellulose nanofiber/polyaniline film as a highly conductive and flexible electrode material for supercapacitors. Carbohydr Polym 2023;304:120519. https://doi.org/10.1016/j.carbpol.2022.120519.

[60] Liu S, Chen Y, Dorsel P-KP, Wu C. Facile preparation of nanocellulose/multi-walled carbon nanotube/polyaniline composite aerogel electrodes with high area-specific capacitance for supercapacitors. Int J Biol Macromol 2023;238:124158. https://doi.org/10.1016/j.ijbiomac.2023.124158.

[61] Liu Q, Jing S, Wang S, Zhuo H, Zhong L, Peng X, et al. Flexible nanocomposites with ultrahigh specific areal capacitance and tunable properties based on a cellulose derived nanofiber-carbon sheet framework coated with polyaniline. J Mater Chem A 2016;4:13352–62. https://doi.org/10.1039/C6TA05131F.

Chapter-6

Conclusion

The thesis has been summarized in this chapter with some key results and highlights associated with our research. The chapter-wise detail analysis is briefly presented. The need for bridging the existing gaps in research on selenium nanocomposites is conveyed in the chapter.

Though renowned as one of the first photovoltaic material, selenium was replaced within a short time with the emergence of silicon solar cells. But Se has gained renewed interests among the research fraternity and resurged lately, as a wide bandgap photoabsorber in tandem solar cells. Better understanding of the structure, functionalization capabilities and integration potential of the material is vital for better device application. The thesis work had attempted to shed new light on certain selenium-based nanocomposites for optical and electrochemical applications.

Chapter 1 presents a brief introduction into nanostructures, the various optical and electrochemical properties associated with them and their suitable applications. A detailed literature review on various Se nanostructures and a short discussion on conducting polymer -polyaniline based nanocomposites is also presented.

The synthesis and characterization of various selenium allotropes in silica host matrix is discussed in **chapter 2**. While cubic and amorphous forms of Se QDs were synthesized via sol-gel technique followed by thermal annealing, a combination of solvothermal assisted sol gel route was adopted for the fabrication of stable monoclinic and trigonal Se in silica. The average crystallite size is in the range 2-10 nm and cubic and trigonal form exhibited blue emission upon UV excitations. Preliminary in-vitro cytotoxicity studies shows that the QDs exhibit negligible cell toxicity on rat spleen cells as evaluated by trypan blue exclusion method.

The characteristic absorption and photoluminescence observed for trigonal Se QDs was explored in detail in **Chapter 3.** The crystal growth mechanism was understood in detail and the various defects observed from the microstructural studies were identified. The trigonal Se-silica was used as a solid-state fluorescent sensing probe for the inner filter effect (IFE) based detection of curcumin. The probe showed good range of detection (0-10 mg) with LOD of 180 µg. The optical features of trigonal Se-silica nanocomposite were found to be suitable for less costly IFE-based practical fluorescence sensors.

Chapter 4 deals with the synthesis and structural elucidation of Se in a stable hybrid conducting polymer polyaniline and cellulose-polyaniline matrix. The chapter discusses the synthesis of the composites of cellulose and/or PANI were via a one-pot polymerization of monomers followed by freeze drying. The structural elucidation of the nanocomposite was performed in detail. The HRTEM studies reveal that Se crystallizes in trigonal structure within the composite.

In **chapter 5**, electrochemical properties of Se/Cellulose/PANI nanocomposites are discussed in detail for supercapacitor applications. The electrochemical performance of the Se-cellulose-PANI is compared with that of PANI, Se-PANI and Cellulose-PANI composites. The electrochemical parameters evaluated on both three-electrode and two-electrode set up is comparable to existing supercapacitor electrodes. The trigonal Se enhances areal specific capacitance (4.55 F/cm^2 at a sweep rate of 2 mV/s) of the material,

while cellulose strengthens the polymer backbone and prevents degradation due to multiple charge-discharge cycles.

To sum it up, the thesis implies importance of Se nanostructures and explored its potential in optical and electrochemical applications. Amorphous, cubic, monoclinic and trigonal forms of Se was synthesized. The blue emission of trigonal nanocrystallites was exploited to design a fluorescence probe for curcumin detection. Furthermore, the electrical conductivity of trigonal Se nanocrystallites is explored to enhance the pseudocapacitance of cellulose/PANI composites which resulted in a potential material with high areal capacitance and cyclic stability.

Chapter-7

Recommendations

Recommendations or future scope of the current research is presented. We anticipate the wide application of different selenium nanostructures in opto-electronic devices and energy storing units in the coming years.

Study of elemental allotropes has always been one of the promising areas in the field of research. This is mainly due to the fact that though allotropes are different forms of the same element, they could have totally unrelated and wide range of properties. The current study has paved way to immense research potential in the fabrication and characterization of selenium nanostructures. In addition to the four polymorphs discussed in the works, attempts can be made to fabricate rhombohedral or orthorhombic Se. Moreover, the optical non-linear properties, dielectric properties and conductivity studies etc of these nanocomposite glasses are still largely unexplored.

Trigonal Se QDs fabricated by solvothermal assisted sol-gel route exhibits a photoluminescence quantum yield (QY) <1%. Defect engineered t-Se QDs can efficiently solve the issue and help to attain higher QY values. Effort towards reducing the defects and surface traps in the material can be made.

A conducting silica hybrid matrix (SiO_2-PANI blend matrix) can be developed and the formation of Se allotropes in the matrix can be assessed. Change in the matrix would change the pore size and network of the medium which in turn might alter the optical and physical properties of the nano crystallites. The conducting nature of the matrix can be helpful in studying the electronic band structure, density of states, photoconductivity and even low temperature electrical conductivity of allotropes which have not been assessed before.

Composites of other polymorphs of Se in cellulose/PANI can be fabricated for electrochemical energy storage. For example, 2D selenium

structures can be intercalated with PANI to enhance the electroactive surface area in these materials. Attempts can be made to improve the specific energy and power associated with the materials while maintaining capacitance retention and improved specific capacitance values. The electrode can be incorporated into flexible and wearable electronics which are heavily consumed in the market for their efficiency, portability and hassle-free use.

The entire work can also be extrapolated to study the allotropes and the application potential of other elements like Phosphorous, Boron, Bismuth etc.

UNIVERSITY OF CALICUT

CERTIFICATE ON PLAGIARISM CHECK

1.	Name of the Research Scholar	ANUPAMA K	
2.	Title of thesis / dissertation	OPTICAL AND ELECTROCHEMICAL STUDIES OF SELENIUM BASED NANOCOMPOSITES	
3.	Name of the Supervisor	Dr. Ann Mary K A	
4.	Department/Institution	Research Scholar Department of Physics St Thomas College (Autonomous), Thrissur Kerala- 680001 Ph: 9446283674,	
5.	Similar content (%) identified	Non Core **Introduction/ Theoretical overview/Review of literature/ Materials & Methods/ Methodology** **6**	Core **Analysis/Result/Discussion / Summary/Conclusion/ Recommendations** **2**
	Acceptable maximum limit (%)	10	10
6.	Software used	iThenticate	
7.	Date of verification	Fri Nov 08 2024 00:00:00 GMT+0530 (India Standard Time)	

**Report on plagiarism check, specifying included/excluded items with % of similarity to be attached.*

Checked by (with name , designation & signature) Dr. Nasirudheen. T, Assistant Librarian, University of Calicut, Kerala

Name and signature of the Researcher Anupama K.

Name and signature of the Supervisor. Dr. Ann Mary K.A

The Doctoral Committee* has verified the report on plagiarism check with the contents of the thesis, as summarized above and appropriate measures have been taken to ensure originality of the Research accomplished herein.

Name & Signature of the HoD/HoI (Chairperson of the Doctoral Committee)

Dr. Martin K. A.
Principal-in-Charge
St Thomas College (Autonomous)
Thrissur - 680 001